Sensor-enabled Robotics for In-process Ultrasonic NDE of Welds

Momchil Vasilev

Department of Electronic and Electrical Engineering

Centre for Ultrasonic Engineering

University of Strathclyde

A thesis submitted for the degree of

Doctor of Philosophy

June 2021

Copyright

Signed: 

Date: 13 August 2021

Acknowledgements

I would like to thank my supervisor Charles MacLeod for recognizing my talent and always pushing me to stretch above and beyond. His help, mentorship and positive attitude along my journey have been invaluable. I would also like to thank my second supervisor Prof. Gareth Pierce for his guidance, and my colleagues in the Centre for Ultrasonic Engineering (CUE) for their technical support, in particular Walter Galbraith, Yashar Javadi and Alex Ward.

I would also like to express my gratitude to my great-uncle Prof. Koliu Donev, for being an exceptional role model, and whose generous sponsorship throughout my undergraduate studies allowed me to make it this far. For your selfless act of kindness I will be eternally grateful.

I owe a massive thank you to my partner in crime Stela for becoming my personal assistant over the last year, keeping all daily chores away and providing encouragement, allowing me to focus on completing this work. I'm happy to say that your services are no longer required.

Finally, I would like to thank my parents Elena and Ivan for nurturing my curiosity for science from an early age, and my brother Ivo, for motivating me to submit my thesis before he works up the courage to submit his - it's your turn now.

Abstract

Fusion welding is a process commonly employed in High Value Manufacturing (HVM), with the automated welding industry expected to reach $10.8 billion by 2026. The sector is, however, facing a rising gap in the workforce and new, sensor-enabled, intelligent systems are required to address the increased demand. Traditional, manually deployed Non-Destructive Evaluation (NDE) is integral to the welding industry, responsible for ensuring the quality, safety and lifetime of welded joints. The weld NDE sector is also under increasing pressure and has become the bottleneck of the supply chain, due to its poor integration with the manufacturing process and the increased production rates from automation.

Future welding HVM operations must react to these challenges, by adopting a holistic approach where the NDE activities are merged with the welding deposition process. Such an approach would fundamentally increase the production quality and reduce the overall costs and lead-time inconsistencies, by providing an early indication for defect formation and enabling their in-process repair.

This thesis presents novel research and multiple developments that contribute to the field of automated fusion welding and in-process ultrasonic NDE. A flexible robotic welding and NDE system was underpinned by a novel adaptive real-time control approach, based on sensory input. Ultrasonic thickness measurement has been deployed for the first time in-process, during live arc welding, for on-the-fly welding parameter control. Lastly, the

in-process weld penetration screening of thin butt-welded joints in steel plates was achieved through non-contact ultrasonic guided wave testing, performed during the welding deposition.

Contents

List of Figures

List of Tables

Abbreviations

A_0	Zeroth order antisymmetric Lamb wave mode
AMC	Adaptive Motion Controller
AVC	Arc Voltage Control
CAD	Computer Aided Design
CAM	Computer Aided Manufacture
CC	Constant Current
CNC	Computer Numerical Control
CUE	Centre for Ultrasonic Engineering
CV	Constant Voltage
DFT	Discrete Fourier Transform
DLL	Dynamic-Link Library
DoF	Degree of Freedom
EC	Eddy Current

EMAT	Electro Magnetic Acoustic Transducer
EMI	Electromagnetic Interference
FEA	Finite Element Analysis
FMC	Full Matrix Capture
FPGA	Field Programmable Gate Array
FTP	Frequency Thickness Product
GMAW	Gas Metal Arc Welding
GTAW	Gas Tungsten Arc Welding
GUI	Graphical User Interface
HAZ	Heat Affected Zone
HDR	High Dynamic Range
HVM	High Value Manufacturing
IR	Inspection Robot
KRC	KUKA Robot Controller
LAW	Laser Arc Welding

LMC	Linear Motion Controller
LU	Laser Ultrasound
MMAW	Manual Metal Arc Welding
NDE	Non-destructive Evaluation
NDT	Non-destructive Testing
PAUT	Phased Array Ultrasonic Testing
PAW	Plasma Arc Welding
PID	Proportional Integral Derivative
PRF	Pulse Repetition Frequency
PWM	Pulse Width Modulation
RSI	Robot Sensor Interface
RMS	Root Mean Square
RoC	Rate of Change
SHM	Structural Health Monitoring
SMAW	Submerged Arc Welding

SNR	Signal to Noise Ratio
STFT	Short Time Fourier Transform
TFM	Total Focusing Method
UAV	Unmanned Aerial Vehicle
UDP	User Datagram Protocol
UT	Ultrasonic Testing
UTM	Ultrasonic Thickness Measurement
WAAM	Wire + Arc Additive Manufacturing
WPD	Welding Penetration Depth
WPS	Welding Procedure Specification
WR	Welding Robot
XML	Extensible Markup Language

Chapter 1

Introduction

1.1. Context of Research

The UK is among the top 10 largest manufacturers in the world, with China, the US, Japan and Germany retaining the leading positions over the past two decades [1], [2]. While the manufacturing sector and welding productivity in the UK and worldwide has, on the whole, increased significantly year-on-year since the 1970s, manufacturing and welding growth has remained generally stagnant throughout [3]. With older members of the workforce retiring, the rising deficit of qualified young labourers is increasing the skill gap in the manufacturing sector [2]. Furthermore, in 2020, the average productivity per worker in the UK reduced by 9.5 %, compared to 2019, due to the COVID-19 pandemic [4].

Welding is one of the occupations with overall high skill requirement and subsequently the profession faces a predicted 60 % worldwide shortage in trained worker availability between 2015 and 2025 [5]. As a result of this, and the fact that 70 % of the welding manufacture costs are associated with wages [6], labour numbers need to be reduced significantly for the UK economy to remain competitive [3].

Therefore, for future manufacturing and welding to increase productivity, remain globally competitive and to achieve growth to meet demand in major areas including transport [7], [8] and energy [9], new approaches in manufacturing concepts and solutions are crucial. New developments in "Smart Manufacturing" technological areas play a fundamental role in offering solutions to these grand challenges and greatly progressing the High Value Manufacturing (HVM) of advanced welded components. Considering the current industrial revolution (4.0) [10], the future HVM process must embrace digitisation and system interconnectivity, enabling sensor driven automation of traditional manufacturing operations to improve their accuracy, repeatability and speed.

The global automated welding industry has been valued at $5.5 billion in 2018 and is predicted to double by 2026, reaching $10.8 billion [11] with industrial articulated robots expected to replace current column and boom systems and manual operations. This growth has been driven by key HVM sectors including automotive, marine, nuclear, petrochemical and defence. However, automated fusion welding systems are often plagued with issues such as gap width variation inflexibility, component and electrode tip misalignment and wire feed problems [6] and hence require additional sensors to mitigate these adverse factors. Paired with the technological demands of industry 4.0, the need for the development of intelligent and flexible sensor-enabled robotic welding systems has become paramount.

Non-Destructive Evaluation (NDE) plays a key role in ensuring the quality, lifetime and fitness-for-purpose of welded joints and as such is integral to the welding sector [12]. NDE of welds is traditionally carried out manually on the as-welded components, after a delay to allow for the components to cool down and for any delayed cracking to develop, with some standards requiring a period of up to 72 hours between welding and inspection [13]. As such, any defects that are detected in the welds and do not pass an acceptance criteria [14] would either cause the part to be sent back for repairs or, in some cases, would lead to scrapping the component altogether. Apart from adding to the overall production process inefficiency, delayed NDE also results in higher production costs and longer, less consistent lead times.

As a result of the wide adoption of automated manufacturing systems, NDE has become a major bottleneck in the production process. This has subsequently raised the demand for automatically-deployed and adaptive NDE in order to keep up with the faster production lines, when compared to manual manufacturing processes [15]. Advances in automated NDE are driven by industrial demand for fast and reliable quality control in high-value and high-throughput applications. Automatic systems provide greater positional accuracy, repeatability and inspection rates when compared to human operators, therefore, resulting in faster inspection speeds and reduced manufacturing costs. The ever-improving capabilities of such systems lead to an overall increase in asset integrity and lifecycle, contributing to further long-term savings. Safety is another key advantage of automated NDE systems, as they can be deployed in hazardous environments, dangerous conditions and sites where human access is limited or not possible [16], [17], thus improving working

conditions and reducing the risks of workplace injuries and harmful substance exposure [18].

The opportunity exists to perform NDE in parallel with the welding deposition, effectively reducing the delay between weld flaw formation and detection. By integrating the inspection into the manufacturing process, an early indication of potential defects can be obtained, effectively addressing the production and cost inefficiencies by allowing for defects to be qualified and potentially repaired in-process. This would be particularly advantageous for welds of thicker components, large bore pipes and metal 3D printed Wire + Arc Additive Manufacturing (WAAM) parts [19], [20] which require days and, in some cases, weeks to complete, as only a small amount of material would need to be removed in order to excavate and repair any defects. Moreover, inspection at the point of manufacture brings forward many advantages over traditional weld NDE such as lower quantities of scrap, more predictable lead-times and reduced overall production costs.

1.2. Problem Statement

Robotic welding is widely used in industry and the deployment of such systems is growing, however, their flexibility is very limited. The new requirements of "Smart Manufacturing" and Industry 4.0 have brought the need for adaptive sensor-enabled robotic behaviour. Such behaviour can be realised by achieving full real-time control of the robot position from an external system, which is able to communicate to various sensors, allowing them to influence the robotic motion on-the-fly.

The use of ultrasonic sensors during the welding poses a challenge due to the harsh environment, high amounts of electromagnetic noise, extreme temperatures required for fusion welding, and the sensitivity of the welding process to external materials like ultrasonic couplant. Low noise electronics, digital signal processing and various coupling techniques can be utilised to enable the in-process deployment of UT during the welding deposition.

Traditional NDE of welded components is carried out manually, up to 72 hours after the welding has finished. As a result of this delay, the increased production rates of robotic welding, and the low scanning rates of manual inspectors, NDE has become a major bottleneck in the supply chain. The automation and integration of ultrasonic NDE into the welding process will shorten the delay between defect formation and defect detection and could be used for process control and quality screening of the produced welds.

1.3. Research Goals

The research goals of the work in this thesis are:

1. Establish the state-of-the-art in robotic NDE systems and in-process UT research.

2. Develop an adaptive motion robotic control approach based on real-time positional corrections.

3. Develop a multi-robot sensor-enabled robotic system for automated welding and NDE to serve as a testbed for this work and future research into in-process NDE.

4. Investigate the feasibility of ultrasonic transducer deployment during live-arc welding.

5. Develop a real-time welding parameter control method based on in-process ultrasonic sample thickness measurement.

6. Investigate the use of non-contact air-coupled ultrasonic transducers and guided Lamb waves for in-process screening of thin plate butt-welds.

1.4. Contributions to Knowledge

This thesis presents a number of unique and novel, industry focused contributions to the fields of robotic welding and NDE as follow:

- A novel sensor-driven adaptive motion algorithm for use with industrial robots. Full external positional control is achieved in real-time and an on-the-fly motion correction is performed based on multi-sensory input.

- A novel multi-robot welding and NDE system is developed, allowing for the flexible manufacture of welded components and the research into, and deployment of, NDE techniques at the point of manufacture.

- On-line ultrasonic thickness measurement during welding deposition is achieved for the first time. The measured thickness is utilised for real-time process control of a number of welding parameters, allowing for a robust welding process that can

adapt to changes in sample thickness. The performance of the developed approach is verified through welding samples with wall thickness variations.

- The screening of thin plate welds during the welding deposition is realised via non-contact gas-coupled transducers. Ultrasonic Lamb waves are induced through the weld seam during live-arc welding, and the relationship between the Welding Penetration Depth (WPD) and the detected ultrasonic signals is characterised.

- The work in this thesis has directly supported and enabled further research in in-process weld inspection, across sectors, with the aim of producing right-first-time welds and WAAM components - the SIMPLE, RoboWAAM and AWESIM projects.

1.5. Thesis Structure

Chapter 2 introduces the theoretical basis, upon which this work is built, including the fundamentals of fusion welding and its associated common defects. The fundamentals of NDE and its automation are outlined with a particular focus on Ultrasonic Testing (UT). Chapter 3 presents on a novel control algorithm, allowing for real-time positional control of a robotic end-effector through a sensor-based on-the-fly adaptive motion. A novel multi-robot welding cell is developed, enabling the repeatable deposition of welds and flexible sensor deployment, underpinning the following in-process NDE work.

The in-process deployment of an ultrasonic wheel probe for on-line thickness measurement of steel plates with changing wall thickness is described in Chapter 4. A

welding parameter relationship between sample thickness and welding current, welding torch travel speed and filler wire feed rate is established and utilised for on-line process control based on the on-line measured sample thickness.

Chapter 5 explores the in-process deployment of an alternative type of ultrasonic transducers, requiring no contact with the workpiece. A guided Lamb wave is induced in a section of a thin plate butt-weld seam through two air-coupled transducers. The solidification of the weld joint is monitored, and the detected ultrasonic signal is correlated to the Welding Penetration Depth (WPD) across a number of samples. Finally, Chapter 6 summarises the work undertaken and introduces the suggested future developments.

1.6. Lead Author Publications Arising From This Thesis

- Vasilev, M., MacLeod, C., Galbraith, W., Javadi, Y., Foster, E., Dobie, G., Pierce, G. & Gachagan, A., "Non-contact in-process ultrasonic screening of thin fusion welded joints", *Journal of Manufacturing Processes. 64, p. 445-454 10 p.*, 2021

- Vasilev, M., MacLeod, C., Javadi, Y., Pierce, G. & Gachagan, A., "Feed forward control of welding process parameters through on-line ultrasonic thickness measurement", *Journal of Manufacturing Processes. 64, p. 576-584 9 p.*, 2021

- Vasilev, M., MacLeod, C., Loukas, C., Javadi, Y., Vithanage, R.K.W., Lines, D., Mohseni, E., Pierce, G. & Gachagan, A., "Sensor-enabled multi-robot system for automated welding and in-process ultrasonic NDE", *MDPI Sensors, vol. 21, no. 15, Art. no. 15, 2021*

1.7. Co-author Publications Arising From This Thesis

1.7.1. Journal Papers

- Javadi, Y., Sweeney, N. E., Mohseni, E., MacLeod, C. N., Lines, D., Vasilev, M., Qiu, Z., Mineo, C., Pierce, S. G. & Gachagan, A., "Investigating the effect of residual stress on hydrogen cracking in multi-pass robotic welding through process compatible non-destructive testing", *Journal of Manufacturing Processes. 8 p.,* 2020

- Javadi, Y., Sweeney, N. E., Mohseni, E., MacLeod, C. N., Lines, D., Vasilev, M., Qiu, Z., Vithanage, R. K. W., Mineo, C., Stratoudaki, T., Pierce, S. G. & Gachagan, A., "In-process calibration of a non-destructive testing system used for in-process inspection of multi-pass welding", *Materials and Design. 195, 13 p., 108981.*, 2020

- Javadi, Y., Mohseni, E., MacLeod, C. N., Lines, D., Vasilev, M., Mineo, C., Foster, E., Pierce, S. G. & Gachagan, A., "Continuous monitoring of an intentionally-manufactured crack using an automated welding and in-process inspection system", *Materials and Design. 191, 12 p., 108655.*, 2020

- Lines, D., Javadi, Y., Mohseni, E., Vasilev, M., MacLeod, C. N., Mineo, C., Wathavana Vithanage, R. K., Qiu, Z., Zimermann, R., Loukas, C., Foster, E., Pierce, G. & Gachagan, A., , "A Flexible robotic cell for in-process inspection of multi-pass welds", *Insight: The Journal of the British Institute of Non-Destructive Testing. 62, 9, p. 526-532 7 p.*, 2020

- Mohseni, E., Javadi, Y., Sweeney, N. E., Lines, D., MacLeod, C. N., Vithanage, R. K. W., Qiu, Z., Vasilev, M., Mineo, C., Lukacs, P., Foster, E., Pierce, S. G. & Gachagan, A., "Model-assisted ultrasonic calibration using intentionally embedded defects for in-process weld inspection", *Materials and Design. 198, 15 p., 109330.*, 2021

- Javadi, Y., Mohseni, E., MacLeod, C. N., Lines, D., Vasilev, M., Mineo, C., Pierce, S. G. & Gachagan, A., "High-temperature in-process inspection followed by 96-h robotic inspection of intentionally manufactured hydrogen crack in multi-pass robotic welding", *International Journal of Pressure Vessels and Piping. 189, 14 p., 104288.*, 2021

1.7.2. Conference Papers

- Javadi, Y., MacLeod, C. N., Pierce, S., Gachagan, A., Kerr, W., Ding, J., Williams, S., Vasilev, M., Su, R., Mineo, C. & Dziewierz, J. "Ultrasonic phased array inspection of wire plus arc additive manufacture (WAAM) samples using conventional and total focusing method (TFM) imaging approaches", *57th The British Institute of Non-destructive Testing Annual Conference: NDT 2018- East Midlands, Nottingham*, 2018

- Javadi, Y., Vasilev, M., MacLeod, C. N., Pierce, S. G., Su, R., Mineo, C., Dziewierz, J. & Gachagan, A., "Intentional weld defect process: from manufacturing by robotic welding machine to inspection using TFM phased array", *45th Annual Review of Progress in Quantitative Nondestructive Evaluation, New York,* 2019

- Javadi, Y., MacLeod, C., Lines, D., Vasilev, M., Mohseni, E., Foster, E., Qiu, Z., Vithanage, R., Zimermann, R., Loukas, C., Pierce, G. & Gachagan, A., "In-process inspection of multi-pass robotic welding", *46th Annual Review of Progress in Quantitative Nondestructive Evaluation, Portland,* 2019

1.8. Additional Publications by the Author

1.8.1. Journal Papers

- Mineo, C., Vasilev, M., MacLeod, C. N., Su, R. & Pierce, S. G., "Enabling robotic adaptive behaviour capabilities for new industry 4.0 automated quality inspection paradigms", *Insight: Non-Destructive Testing and Condition Monitoring. 62, 6, p. 338-344, 2020*

- Javadi, Y., MacLeod, C. N., Pierce, S. G., Gachagan, A., Kerr, W., Ding, J., Williams, S., Vasilev, M., Su, R., Mineo, C. & Dziewierz, J., "Ultrasonic phased array inspection of wire + arc additive manufacture samples using conventional and total focusing method imaging approaches", *Insight: Non-Destructive Testing and Condition Monitoring. 61, 3, p. 144-148 5 p.*, 2019

- Javadi, Y., MacLeod, C. N., Pierce, S. G., Gachagan, A., Lines, D., Mineo, C., Ding, J., Williams, S., Vasilev, M., Mohseni, E. & Su, R., "Ultrasonic phased array inspection of a Wire + Arc Additive Manufactured (WAAM) sample with intentionally embedded defects", *Additive Manufacturing. 29, 10 p., 100806*, 2019

- Mineo, C., Vasilev, M., Cowan, B., MacLeod, C. N., Pierce, S. G., Wong, C., Yang, E., Fuentes, R. & Cross, E. J., "Enabling robotic adaptive behaviour capabilities for new industry 4.0 automated quality inspection paradigms", *Insight: The Journal of the British Institute of Non-Destructive Testing. 62, 6, p. 338-344 7 p.*, 2020

- Mohseni, E., MacLeod, C., Javadi, Y., Vithanage, R. K. W., Qiu, Z., Lines, D., Foster, E., Lukacs, P., Vasilev, M., Zimermann, R., Pierce, S. G. & Gachagan, A., , "A model-based study of transmit-receive longitudinal arrays for inspection of subsurface defects", *Journal of Nondestructive Evaluation, Diagnostics and Prognostics of Engineering Systems. 3, 3, 8 p., 031102*, 2020

- Loukas, C., Williams, V., Jones, R., Vasilev, M., MacLeod, C. N., Dobie, G., Sibson, J., Pierce, G. & Gachagan, A., "A cost-function driven adaptive welding framework for multi-pass robotic welding", *Journal of Manufacturing Processes. 67, p. 545-561 17 p.*, 2021

1.8.2. Conference Papers

- Daily, P., Windmill, J.F.C., Jackson, J., Vasilev, M., "An in-air ultrasonic acoustic beam shifter metamaterial", *2019 IEEE International Ultrasonics Symposium (IUS), Glasgow*, 2019

1.8.3. Working Papers

- Mineo, C., Wong, C., Vasilev, M., Cowan, B., MacLeod, C. N., Pierce, S. G. & Yang, E., "Interfacing Toolbox for Robotic Arms with Real-Time Adaptive Behavior Capabilities", *Glasgow: University of Strathclyde*, 2019

1.9. Other Output Arising From This Thesis

- Nuclear Institute Young Generation Network speaking competition, “Robotic & Sensing Enabled Welding - Inspect while you weld”, Scottish and National Winner, 2018

- Three Minute Thesis (3MT), University of Strathclyde overall winner, 2019

- Images of Research, University of Strathclyde, *„Manufacturing Beauty“,* Transformative technology category winner (see Figure 3.8), 2020

Chapter 2

Research Background

2.1. Fusion Welding

Joining of metallic structures, or welding, is an important part of our modern world, being employed in numerous high-value manufacturing industries including aerospace, automotive, defence and energy. The roots of modern welding stem back to the end of the 19th century, when technological advancements made it possible to create controlled and focused heat sources [6]. Fusion welding is a permanent joining method, where two solids are fused by a moving liquid weld pool [21]. A localised heat source lies at the heart of all welding processes as the workpiece needs to be heated up beyond its melting point (around 1500°C for mild steel) to create the weld pool and for fusion to occur. This could be induced using a high powered laser beam [22], high current electrodes (in resistance welding), a plasma arc or an electric arc. Fusion welding allows for pieces of material of similar or dissimilar nature to be joined in a variety of configurations ranging from simple butt to butt connections in plates and pipes to more complex shapes, e.g. pipe saddle joints, petrochemical and nuclear vessels, and ship hulls [6] (Figure 2.1).

a) b)

Figure 2.1 a) Saddle weld in pipe structure; b) weld seams in ship hull.

The most common arc welding processes are Manual Metal Arc Welding (MMAW), Gas Metal Arc Welding (GMAW), Gas Tungsten Arc Welding (GTAW), Plasma Arc Welding (PAW), Submerged Metal Arc Welding (SMAW) and Flux Cored Arc Welding (SMAW)[23]. Due to equipment availability, the work in this thesis has focused on the GTAW process detailed in Figure 2.2. In GTAW a non-consumable Tungsten electrode maintains an electric arc to the workpiece, creating the localised weld pool, while a consumable wire, usually from the same material as the workpiece, is added to the melt pool for joint reinforcement [6]. Protection from oxidation is provided through a shielding Argon gas coming from the welding torch.

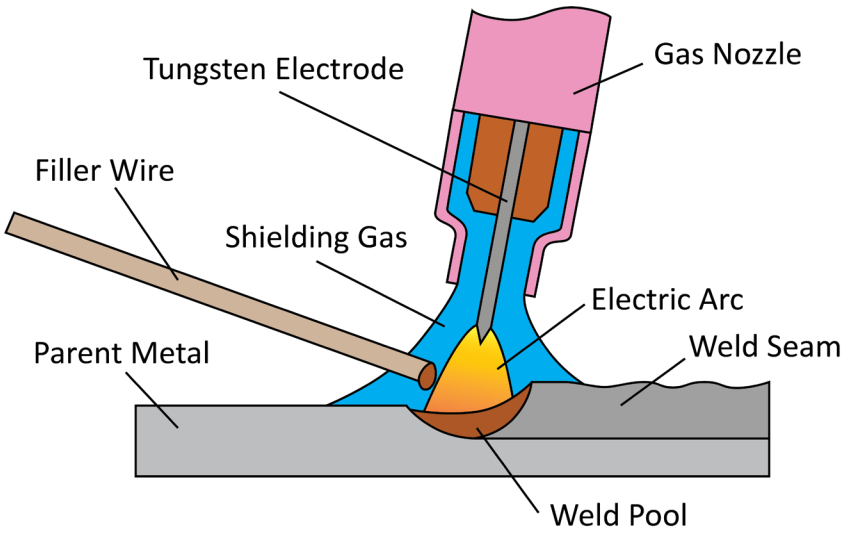

Figure 2.2 Gas Tungsten Arc Welding process diagram.

There are many important parameters that influence the overall properties of a weld, however, there is a universal measure for welding power. The arc energy measures how much energy the welding arc can supply to the workpiece by taking into account the welding current, welding voltage and torch travel speed and is calculated from (2.1) [24].

$$AE = \frac{60 * V * I}{1000 * T_S} \tag{2.1}$$

Where AE = arc energy (kJ/mm), V = welding voltage (V), I = welding current (A) and T_S = welding torch travel speed (mm/min). The GTAW process utilises a variable Constant Current (CC) power source and the arc voltage is controlled by the distance between the non-consumable Tungsten electrode and the workpiece. The GMAW process, on the other hand, utilises a variable Constant Voltage (CV) power source, wire speed and Contact Tip to Work Distance to control arc current. Finally, the SAW process uses either the CV or CC technique to control the overall arc power. When considering automated applications,

modern fusion power sources offer a number of control and programming options, of both a digital and analogue nature, of basic parameters such as arc current (GTAW), arc voltage (GMAW), wire speed (GMAW and automated GTAW), and more advanced parameters such as up- and down-slopes, pulse frequency, balance and amplitude in pulsed and alternating current welding applications.

Unintentional weld flaws and defects can occur in the welded joint and can have a detrimental effect on the safety, integrity and lifetime of welded components. The BS ISO 6520-1:2007 standard [25] covers the classification of geometrical imperfections in metallic fusion welds. Some of the most common defects including lack of root penetration, undercut, slag inclusion, porosity, lack of fusion and cracks are shown in Figure 2.3.

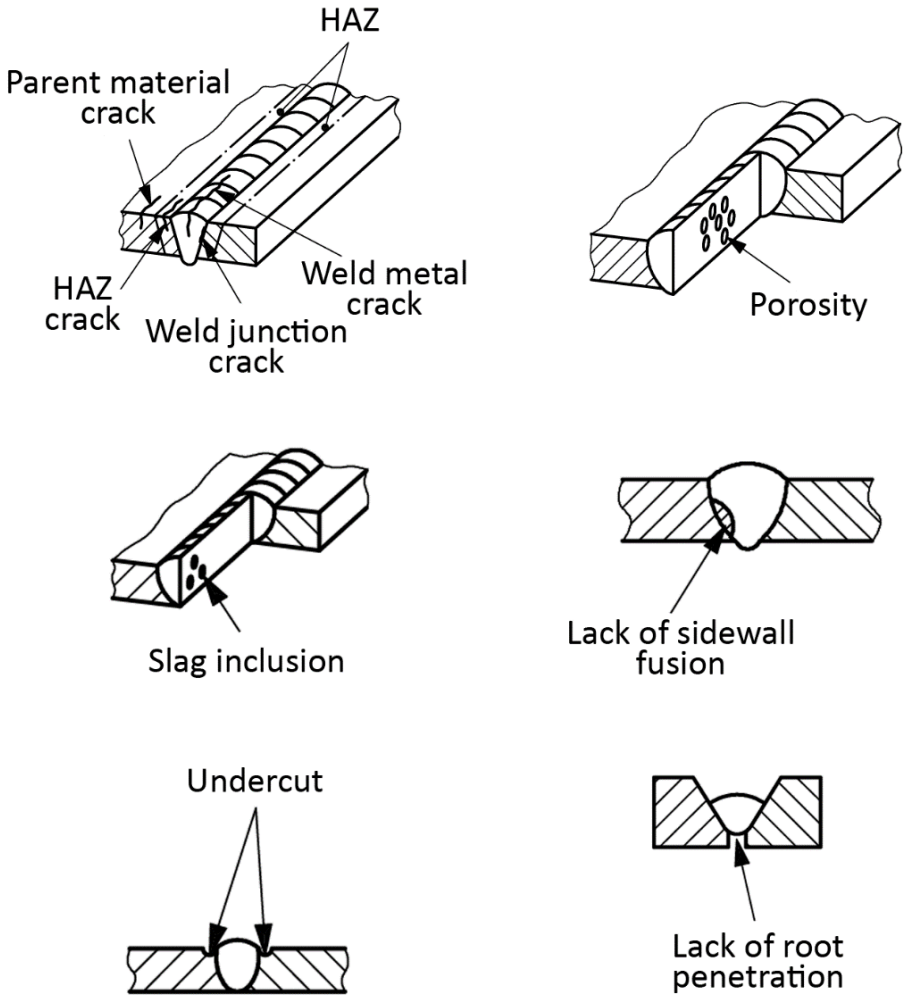

Figure 2.3 Common fusion welding defects.

2.1.1. Welding Process Monitoring

One way of reducing the occurrence of weld flaws is by implementing advanced process monitoring and control approaches during the welding process. On-line process monitoring utilises electrical, optical, auditory and other types of sensors for closed-loop control of the welding process, where the weld pool and deposited weld bead are commonly measured. Typical optical sensor integrations can be split into passive, when consisting of only optical sensors, and active, when a structured light source, usually a laser or a projector, is used in conjunction with the optical sensors. Simpler solutions combine a single camera with image processing, like edge detection, to accurately measure the width of the weld pool (Figure 2.4 a) [26]. In [27] authors demonstrate a more advanced approach that utilises an infrared camera and an artificial neural network to infer the weld bead width and depth based on the measured surface temperature of the workpiece. Moreover, hyperspectral cameras have been used during the welding process to identify welding current variations, protection gas shortages and changes in welding torch offset [28].

With regards to active optical systems, a projected laser line can be used to both track the weld seam [29] and to measure the profile geometry of the produced weld bead for detection of defects such as weld bead misalignment, undercut and plate displacement (Figure 2.4 b)[30]. In [31] such a laser line is projected behind the weld pool in a GTAW butt-weld configuration and the arc current and arc length are closed-loop controlled to maintain full weld penetration. Due to the distance between the weld pool and the laser line, however, certain delays were present in the control loop. Alternatively to a laser line,

a laser dot pattern can be projected on the weld pool. The dot pattern that is reflected off the weld pool surface can be captured using a camera and subsequently used to reconstruct and measure the 3D surface of the weld pool [32]. It has been demonstrated that by measuring the weld pool length, width and convexity of the weld pool surface, the weld penetration can be estimated in real-time [33] and the weld pool surface can be controlled in a closed-loop [34].

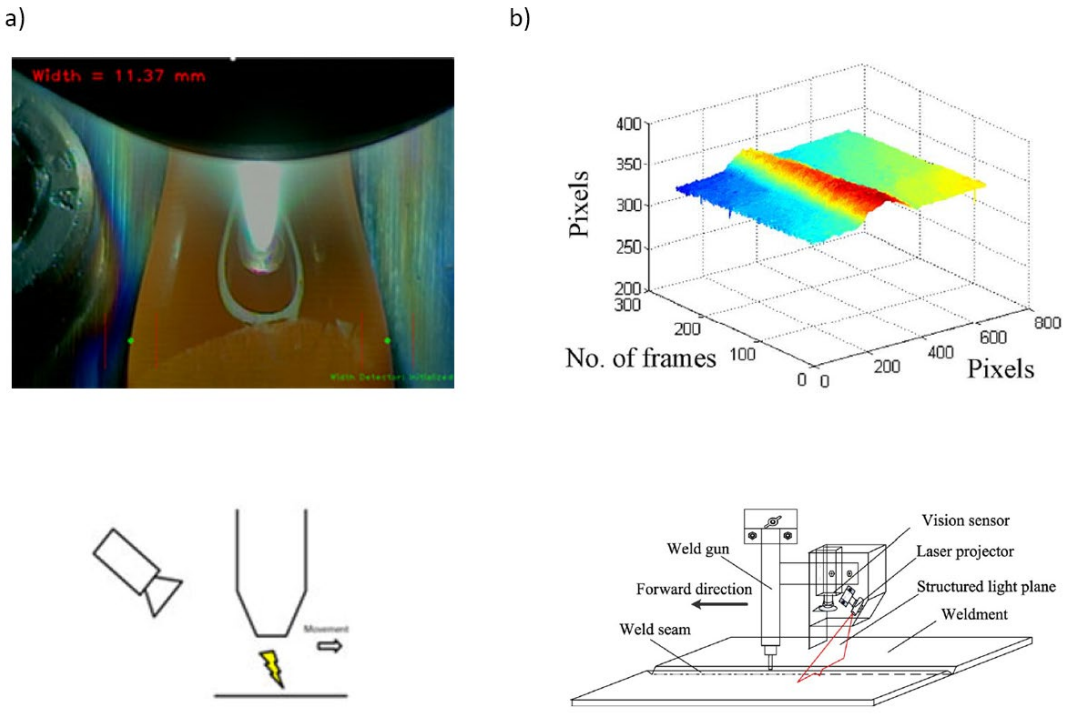

Figure 2.4 a) Passive optical measurement of weld bead width; b) active optical measurement of weld bead profile.

2.1.2. Wire + Arc Additive Manufacturing

Wire + Arc Additive Manufacturing is a 3D metal printing method that has generated a lot of interest from both academia and the private sector over the last decade. The technique utilises arc welding equipment to progressively deposit thin layers of material

to build up the final component, allowing to directly produce highly customised parts. More importantly, complex geometries can be manufactured from fewer parts and without the limitations of conventional machining methods, e.g. straight cuts, slots and round holes, and available stock materials, i.e. billets, sheets and pipes [20]. WAAM makes it possible to rapidly and efficiently deposit large components above 10 kg in weight in materials including titanium, steel and aluminium, as shown in Figure 2.5 [19]. Furthermore, the process has low material and equipment costs, as demonstrated by the open source metal 3D printer presented in [35] that was reported to cost under $2000.

As the metal additive manufacturing techniques are relatively recent, research is currently focused on increasing the deposition rates [36], optimising the path-planning of the build sequence [37] and controlling the metallurgical properties of the manufactured components [38]. Moreover, there are currently no widely accepted standards for testing the quality and assuring the absence of defects in WAAM parts, while the amount of repair that can be carried out on such components is very limited.

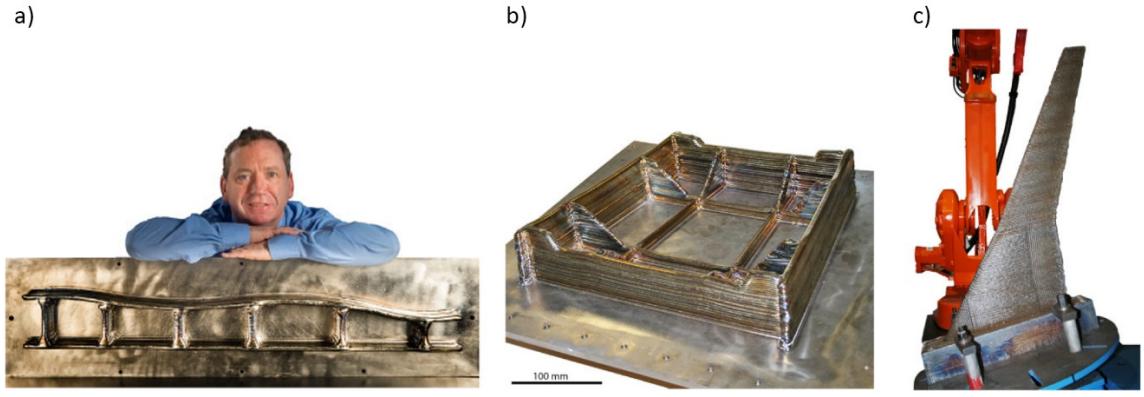

Figure 2.5 WAAM components: a) 1.2 m Ti–6Al–4V wing spar; b) 24 kg Ti–6Al–4V external landing gear assembly; c) high strength steel wing model for wind tunnel testing.

2.2. Non-destructive Evaluation

Many welded joints and components serve a key structural and safety role and a potential failure of these could have catastrophic consequences. Therefore, such welds need to be thoroughly tested to detect and classify any imperfections and to ensure their safety and integrity. Non-Destructive Evaluation (NDE), often used interchangeably with Non-Destructive Testing (NDT), allows for a variety of components including welds to be tested unobtrusively, without the need of cutting or damaging them during the inspection process, and is for that reason widely utilised in practice. While NDT encapsulates all non-destructive testing activities, the aim of NDE is to describe the nature, size and location of any detected flaws and to compare them with an acceptance criteria in order to qualify the end component's fitness-for-purpose [12]. NDE methods have no defined boundaries and can be as simple as a visual examination of the component surface. In general, gross flaws visible from the surface can be detected using visual inspection, while approaches like Dye Penetrant [39] and Magnetic Penetrant Inspection [40] can detect finer surface-connected cracks. Common techniques for detecting flaws embedded under the weld surface, include Eddy Current (EC) [41] , X-ray [42] and Ultrasonic Testing (UT) [43].

2.2.1. Ultrasonic Testing

Ultrasonic Testing is the most commonly employed NDE method for testing welds in materials including mild steel, stainless steel, titanium and aluminium [12], [44], due to its relatively low costs, high accuracy and its ability to detect and size both planar and volumetric defects. Ultrasonic waves are sound waves with a frequency above 20 kHz and are used in many industrial applications. Ultrasonic sensors are commonly associated with the automotive industry for their use in reverse obstacle detection and parking assist [45], operating at low frequencies e.g. 40 kHz [46]. In contrast, the frequency of ultrasonic sensors used for NDE is dictated by its wavelength in the material being examined, and the size of the expected flaws. For example, a 5 MHz ultrasonic wave would have a wavelength of approximately 1 mm in steel, which would generally allow to detect flaws of 1 mm in size.

2.2.1.1. Ultrasonic Wave Modes

There are different modes of ultrasonic waves, based on the nature of the mechanical vibrations, as shown in Figure 2.6 [47]. In longitudinal, or compression/pressure, waves the direction of particle motion is aligned with the travel direction of the wave, whereas in shear, or transverse, waves the particles are oscillating at a normal angle to the direction of travel. While longitudinal waves can propagate through solid, gas and liquid media, transverse waves are limited to solids.

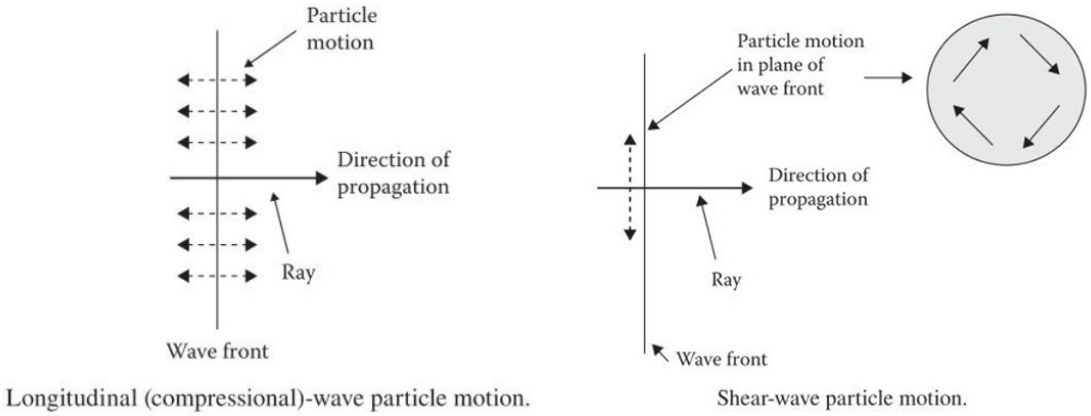

Figure 2.6 Longitudinal and shear wave particle motion

2.2.1.2. Acoustic Impedance

When an ultrasonic wave reaches the boundary between two materials with different acoustic impedances, part of the wave energy is transmitted into the material, and the rest of the energy is reflected. The acoustic impedance for a plane wave in a lossless isotropic material can be calculated from Equation 2.2:

$$Z = \rho c \tag{2.2}$$

Where Z = acoustic impedance (kg/m^{2}s or Rayl) , ρ = density of the material (kg/m^3) and c = speed of sound in the material (m/s). The acoustic transmission coefficient for normal incidence of plane waves can then be calculated by Equation 2.3:

$$RE = \left(\frac{z_1 - z_2}{z_1 + z_2}\right)^2 \tag{2.3}$$

Where RE = reflected energy coefficient, Z_1 = acoustic impedance of first material and Z_2 = acoustic impedance of second material. For example, when a longitudinal wave

propagating in water reaches a steel boundary, 88 % of the ultrasonic wave energy will be reflected, while only 12 % will be inserted into the steel medium.

2.2.1.3. Mode Conversion

Mode conversion can occur when ultrasonic waves are directed to a medium boundary at an angle, different from the normal. Thus, a longitudinal wave can be transformed to a shear wave, for example. Figure 2.7 shows the boundary between a fluid/gas and a solid medium. A longitudinal wave with a speed of V_{L1} is refracted into a longitudinal and a shear wave with angles θ_{2L} and θ_{2S}, which are calculated from the propagation speed inside the solid medium and through Snell's law (Equation 2.4).

$$\frac{V_{1L}}{sin\,(\theta_1)} = \frac{V_{2L}}{sin\,(\theta_{2L})} = \frac{V_{2S}}{sin\,(\theta_{2S})} \tag{2.4}$$

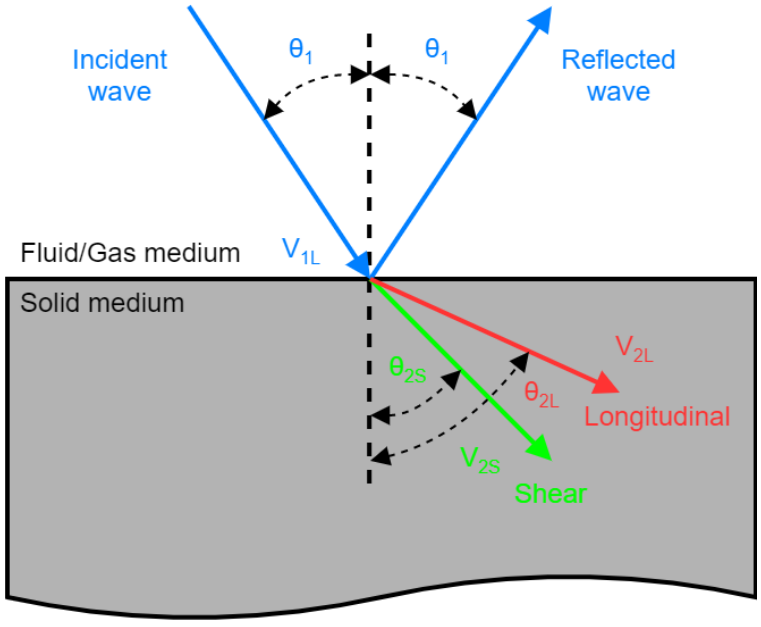

Figure 2.7 Ultrasonic refraction and mode conversion between a fluid/gas and a solid medium.

Two critical angles are present for this configuration. The first critical angle occurs when θ_{2L} reaches 90 °, the longitudinal energy is either reflected, or converted into an interface wave. At angles above the critical angle, only a shear wave is inserted into the solid material. Similarly, the second critical angle occurs when θ_{2S} reaches 90 ° and no significant energy can be inserted into the solid.

2.2.1.4. Conventional UT

Piezoelectric ceramic transducers convert electrical energy into mechanical energy and vice versa, and are for that reason commonly employed for UT. The transducer and material under test are usually in direct contact, with a thin layer of liquid couplant applied in between, reducing the impedance mismatch between the two materials [48]. Figure 2.8 a) shows a pulse-echo configuration, where a single transducer is used to transmit (Tx) a longitudinal wave into the sample, and to receive (Rx) the reflected ultrasonic signal. When looking at the amplitude of the received signal with respect to time, the echo from the back-wall of the sample can be identified. In the presence of a flaw in the sample (Figure 2.8 b), part of the ultrasonic energy is reflected off the flaw, resulting in an additional echo, appearing before the back-wall reflection. As single-element transducers utilise the same piezoelectric crystal to transmit and to receive the signals, the Tx excitation signal introduces a post-transmission ringing in the element that masks any reflections received near the surface of the transducer. This can be avoided by using a split-crystal transducer that contains two separately connected elements, where one is used to transmit, and the other to receive.

If the propagation velocity of the ultrasonic wave in the material is known, the thickness of the sample can be accurately measured. This approach is introduced and utilised in Chapter 4 for in-process thickness measurement and welding power control. Moreover, the location and amplitude of the flaw echo can be used to measure its depth and to infer its size. In the pitch-catch UT configuration shown in Figure 2.8 c), a second transducer receives the transmitted ultrasonic signals. In this case, the presence of a flaw can be identified by a reduction of the direct path signal amplitude, as demonstrated in Figure 2.8 d).

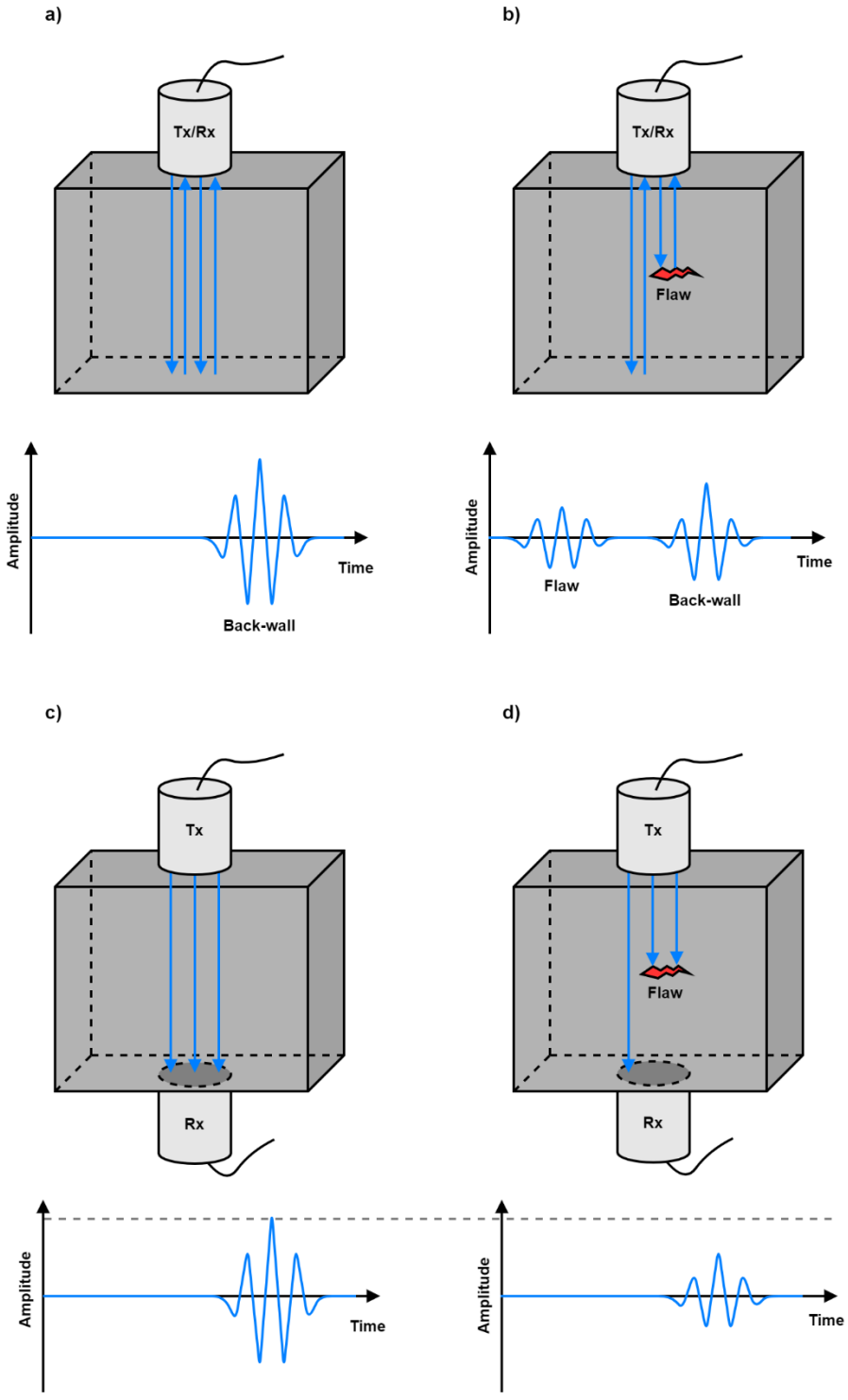

Figure 2.8 Conventional ultrasonic testing: a) and b) pulse-echo; c) and d) pitch-catch.

2.2.1.5. Phased Array UT

Ultrasonic arrays are sensors that contain a number of independently connected piezoelectric elements, offering a higher degree of inspection flexibility than conventional single-element and split-crystal transducers [43]. The transmission and reception can be achieved through any combination of elements, while the amplitude and phase, or delay, of the excitation signal can be individually controlled. This approach is called beamforming, and allows for a number of inspection modalities to be carried out from one location with a single PAUT probe. For example, a range of elements can be excited to achieve plane wave imaging (Figure 2.9 a), focused imaging (Figure 2.9 b) or steered beam imaging (Figure 2.9 c) and d) [43]. Moreover, PAUT probes enable the acquisition of all transmit-receive pairs through Full Matrix Capture (FMC) which offers the advantage of retrospective beamforming and reconstruction of the inspected area through the Total Focusing Method (TFM) [49], [50]. Furthermore, FMC enables the development and use of advanced image processing algorithms, producing results which cannot be achieved using conventional ultrasonics.

The versatility of phased array transducers and their potential to increase the speed, resolution and quality of ultrasonic inspection have lead to their wide use in industrial applications. More importantly, beamforming enables the NDE of complex geometries that would traditionally be very hard or not possible with conventional UT, such as of WAAM components [51]–[53].

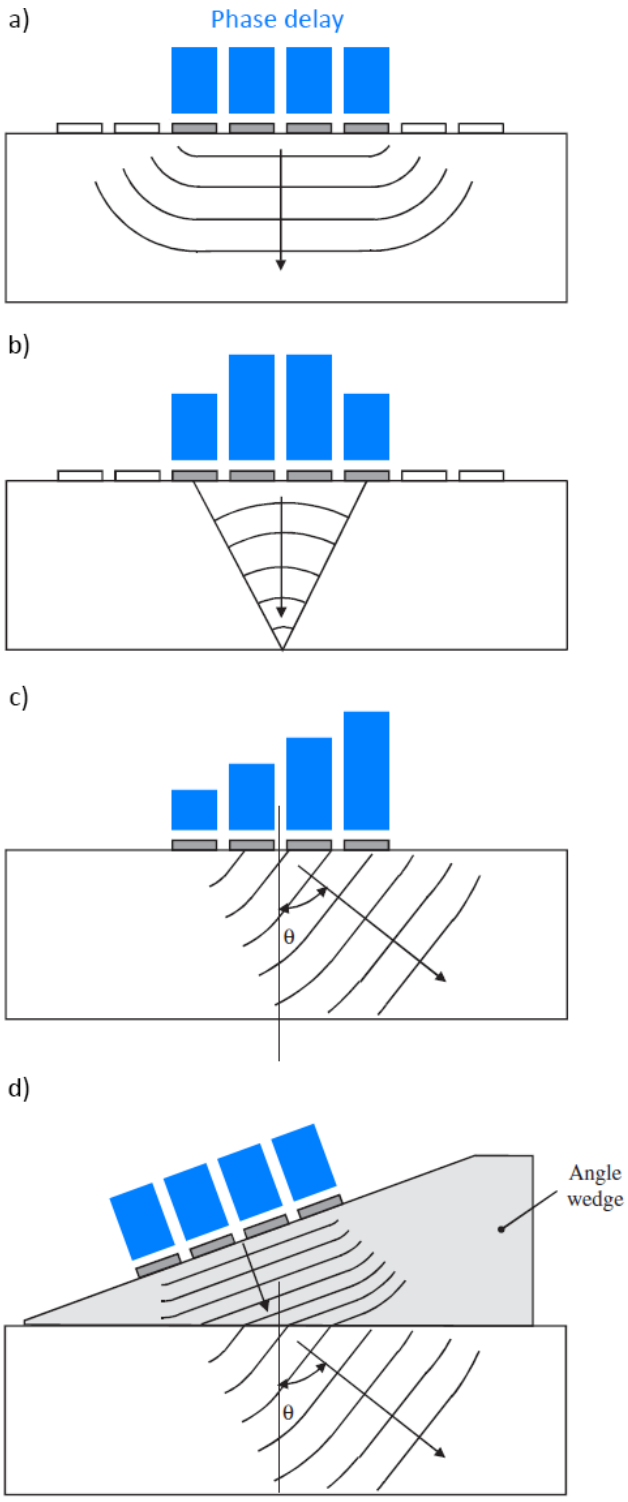

Figure 2.9 Phased array inspection beamforming: a) plane wave imaging; b) focused imaging; c) angular steering; d) angular steering with angled wedge.

2.2.2. Automated NDE

Automation of the NDE process allows to achieve higher scanning rates and more accurate sensor positioning, compared to manual operations. Moreover, automated NDE can be deployed in hazardous environments, where human operators would be of risk of injury, effectively reducing or eliminating their exposure to the harmful conditions. Single-axis scanners offer the ability for axial or circumferential scans of pipes and are suitable for on-site inspection of assets like oil & gas pipelines (Figure 2.10 a). Such scanners can be guided by a track, or can be free-rolling, where a projected laser line is used by the operator to positionally align the scanner with the weld [54], [55]. Mobile crawlers systems offer a higher degree of positional flexibility through a two-axis differential drive and can magnetically attach to the surfaces of assets enabling vertical deployment (Figure 2.10 b) [56]. In addition, their compact size makes them well suited for remote applications with constrained access [16]. One particular challenge with such crawlers is accurately tracking their position, which is achieved through a combination of drive encoders, accelerometers, machine vision and, in often cases, expensive external measurement systems [57]. Multirotor Unmanned Aerial Vehicles (UAV) can deliver visual [58], laser [59] and, more recently, contact ultrasonic (Figure 2.10 c) [60] sensors in remote NDE inspection scenarios, where a magnetic crawler could not be deployed. These systems can typically position and orient sensors in four axes (X, Y, Z and yaw) with recently developed over-actuated UAVs aiming to overcome this in support of omnidirectional contact-based airborne inspection [61]. While umbilical/tether cables are used commonly with mobile crawlers, they pose a challenge for the manoeuvrability and range of aerial systems. As a

result, the power source, driving electronics and data storage for NDE sensors need to be on board the multirotor and, therefore, must be designed according to its limited payload capabilities. Furthermore, UAVs are also highly susceptible to positional instability caused by wind and other aerodynamic effects found in proximity to industrial structures under test.

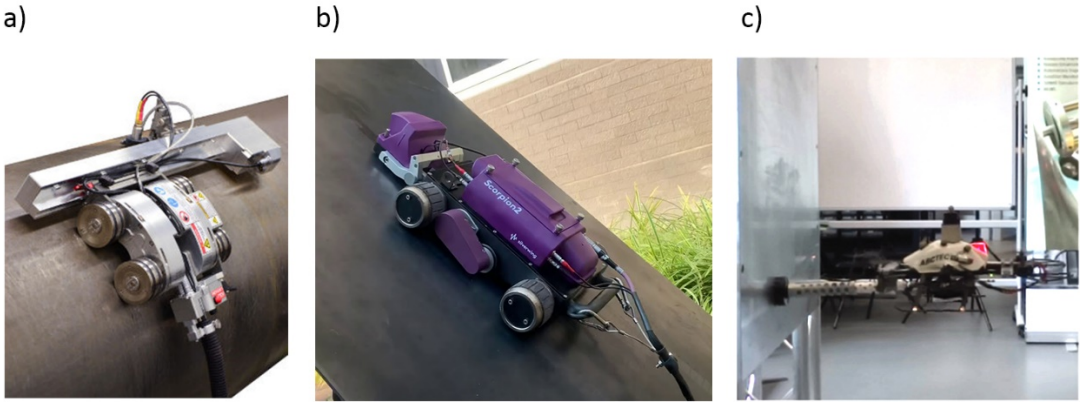

Figure 2.10 Automated welding systems: a) JIREH single-axis motorized scanner; b) Eddyfi Scorpion crawler; c) AscTec Firefly UAV.

Fixed inspection systems offer the highest degree of positional accuracy, compared to other automated systems. Gantries and cartesian scanners (Figure 2.11 a) operate in a planar or boxed work envelope and are suited for components with simple geometries. Articulated robotic arms (Figure 2.11 b), on the other hand, operate in a spherical work envelope and enable the precise delivery of sensors in 6 Degrees of Freedom (DoF) with pose repeatability of under 0.05 mm and maximum linear velocities of 2 m/s [62]. They are widely used in industry thanks to their flexibility and reprogrammability, and their positional repeatability makes them suited for operations with well controlled conditions such as component dimensions, position and orientation. 7 DoF robots are also available, with the additional 7th axis in the form of a linear track or a rotational joint allowing for a

wider range of robot poses to reach the same end-effector position, enabling the inspection of highly intricate structures (Figure 2.11 c).

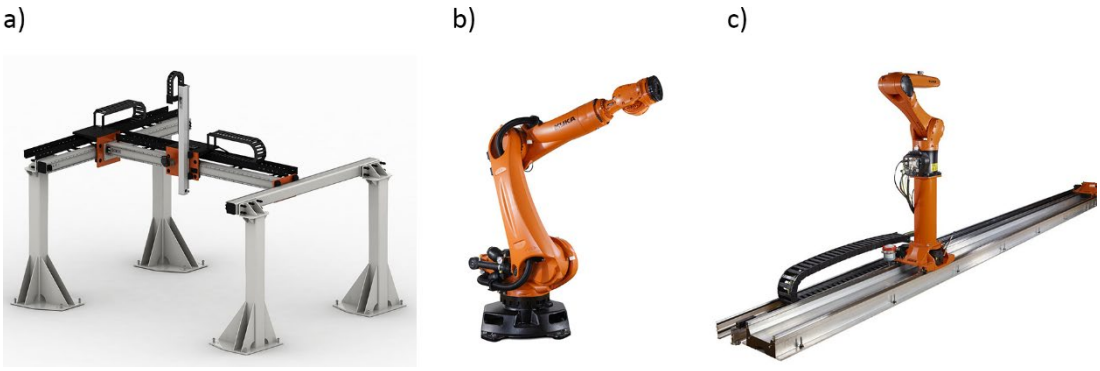

Figure 2.11 Fixed robotic systems: a) gantry/cartesian robot; b) articulated robotic arm; c) articulated robotic arm on a linear track.

2.2.3. In-process Ultrasonic NDE

While traditional weld inspection is performed up to 72 hours after all welding is complete [13], in-process NDE carried out during the manufacture, allows for the detection of weld flaws as they form, introducing the opportunity for early repair. The liquid couplant used for conventional UT is effective for inspecting as-built components, however introducing such liquid compounds to a workpiece during welding is undesirable, as it could produce defects like lack of fusion and porosity [63]. Furthermore, such couplants have high thermal conductivity which would accelerate the heat transfer from a hot workpiece to the transducer. Traditional piezoelectric probes can safely operate at temperatures up to 60 °C, with commercial contact high-temperature wedges allowing the inspection of surfaces of up to 150 °C for very short periods of time [64] making in-process inspection impractical. Therefore, dry-coupled and non-contact techniques that do not require any additional couplant are particularly suitable for in-process UT.

Another key challenge of in-process welding inspection is the large amount Electromagnetic Interference (EMI), which is radiated from the welder power source, robotic motor drives and other industrial equipment, ultimately increasing the system noise and contributing to inaccurate measurements. Furthermore, in GTAW a high-frequency signal (250 kHz for the available welding equipment) is superimposed to the welding current for the first few seconds after triggering the power source in order to develop the electric arc between the electrode and workpiece [65]. Therefore, from an ultrasonic measurement perspective, welding is considered as a harsh environment and a robust UT system deployed during welding should be able to tolerate the aforementioned challenges introduced by the process.

Chapter 3

Sensor-enabled Robotic Welding and NDE System

3.1. Introduction

The current industrial automated fusion welding approaches largely consist of either column and boom gantries or 6 DoF robotic manipulators equipped with controllable welding power sources. Such systems generally do not possess the ability to react to any changes in the workpiece, process or environment and, therefore, require additional sensors to achieve an intelligent, adaptive behaviour. State-of-the-art robotic systems rely on robot controllers for calculating the kinematics and executing the motion, which is usually programmed by manually jogging the robot to individual positions through a teach pendant. As a result, the deployment of any external sensors is highly dependent on the commercially available software provided by industrial robot manufacturers and the supported communication protocols. Therefore, it would be particularly beneficial to bypass the internal motion planning of a robotic controller and to perform external real-time positional control, effectively shifting the path-planning and sensor integration to an external controller. In particular, the Robot Sensor Interface (RSI) [66] communication

protocol could be leveraged in order to provide such an external positional control capability.

RSI was developed by industrial robot manufacturer KUKA for influencing a pre-programmed motion path through sensor input, in order to achieve an adaptive robotic behaviour. The protocol is based on an interpolation cycle, which executes in real-time intervals of 4 ms for KRC 4 (KUKA Robot Controller) controller-based robots, and 12 ms for legacy KRC 2 based robots. During this, an XML string with a special format, described in Section 3.3.1, is transmitted over a UDP (User Datagram Protocol) link between the robotic controller and an external sensor or system. In [15] RSI was used in conjunction with a force-torque sensor to maintain constant contact force between a composite wing component and an ultrasonic roller probe, effectively accounting for any discrepancies between the CAD model of the part and the as-built geometry. This method, however, required that the motion path is pre-set within a robotic program, making use of the built-in KUKA trajectory planning algorithm. In [67] a custom trajectory planning algorithm was developed and embedded on a KRC 4 controller through a real-time RSI configuration diagram. This gave the capability to dynamically set and update the target position over Ethernet, and the layer of abstraction based on a C++ Dynamic-Link Library (DLL) made it possible to utilise the toolbox in various programming environments e.g. MATLAB, Python and LabVIEW. Although providing a fast response time, the toolbox did not have a provision for real-time motion correction based on sensory input, and was fully reliant on the KRC for execution.

This chapter presents the development of a sensor-enabled multi-robot system for automated welding and in-process ultrasonic NDE inspection. A real-time control algorithm for adaptive robotic behaviour is introduced and its deployment for automated GTAW welding is demonstrated.

3.2. Hardware

The automated welding and NDE system depicted in Figure 3.1 is based around a National Instruments cRIO 9038 [68] real-time embedded controller. The cRIO features a real-time processor and a Field-Programmable Gate Array (FPGA) on board, which enables fast, real-time parallel computations. Eight expansion slots for additional Input/Output modules enable direct sensor connectivity in addition to the Ethernet, USB and other interfaces, featured on the cRIO. The expansion modules used were the NI 9476 Digital Output, NI 9263 Analogue Output, NI 9205 Analogue Input, NI 9505 DC Motor Drive and NI 9214 Thermocouple Input.

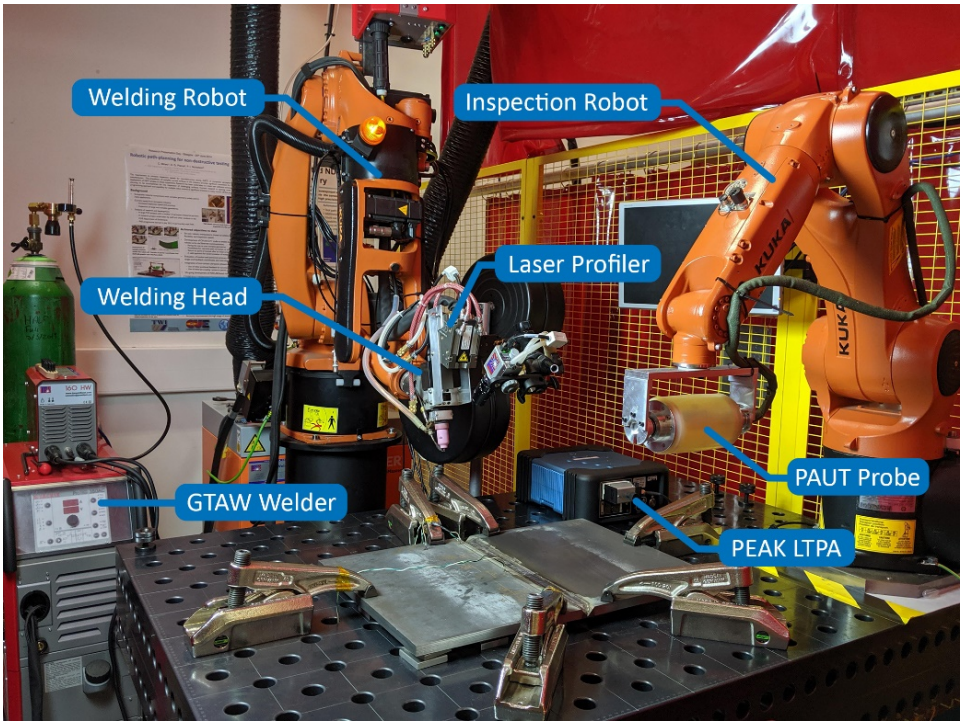

Figure 3.1 Novel sensor-enabled multi-robot welding and in-process NDE system.

Automation was implemented through two 6 DoF industrial manipulators: a KUKA KR5 Arc HW with a KRC 2 controller was used as the Welding Robot (WR), while a KUKA AGILUS KR3 with a KRC 4 controller was used as an Inspection Robot (IR). The welding hardware utilised were a JÄCKLE/TPS ProTIG 350A AC/DC [69] welding power source and a TBi Industries water-cooled welding torch, mounted on the welding robot end-effector. The welding arc was triggered through a 24 V digital signal connected to the power source, while the arc current was set through a 10 V differential analogue line. The power source featured process feedback in the form of measured arc current and arc voltage, also transmitted through differential analogue lines. A JÄCKLE/TPS 4-roll wire feeder, with an optical encoder was powered and controlled via the NI 9505. Its rotational speed was measured and controlled using Pulse Width Modulation (PWM) and was

related appropriately to the desired control metric of linear wire feed rate. Unless otherwise stated, a SUPRAMIG solid wire, with a 1 mm diameter was used as a filler wire.

A MicroEpsilon ScanControl 9030 [70] seam tracker was utilised for weld seam tracking and measurement, while a XIRIS XVC 1100 [71] High Dynamic Range (HDR) weld monitoring camera provided visual feedback of the process. The workpiece temperature was measured through permanently attached thermocouples, which were used to maintain the workpiece within a desired interpass temperature range. The thermocouples were also utilised for monitoring the temperature gradient across the workpiece, which is a crucial requirement for temperature compensation of the ultrasonic images. A high-temperature PAUT probe was attached to the flange of the IR and was driven by a PEAK LTPA [72] low-noise ultrasonic phased array controller. The bandwidth and storage of the cRIO were only sufficient for inspection with conventional UT probes, therefore, the LTPA had to be directly connected to the host PC when using phased array probes. This bandwidth limitation could be addressed by substituting the cRIO with a high-performance NI PXI real-time controller. Finally, the Graphic User Interface (GUI) was deployed on the host PC, facilitating the user input, process monitoring and control. A high-level diagram of the system architecture is shown in Figure 3.2, where the hardware components are represented by blue blocks, the software tasks are represented by green blocks and the communication links are shown as arrows.

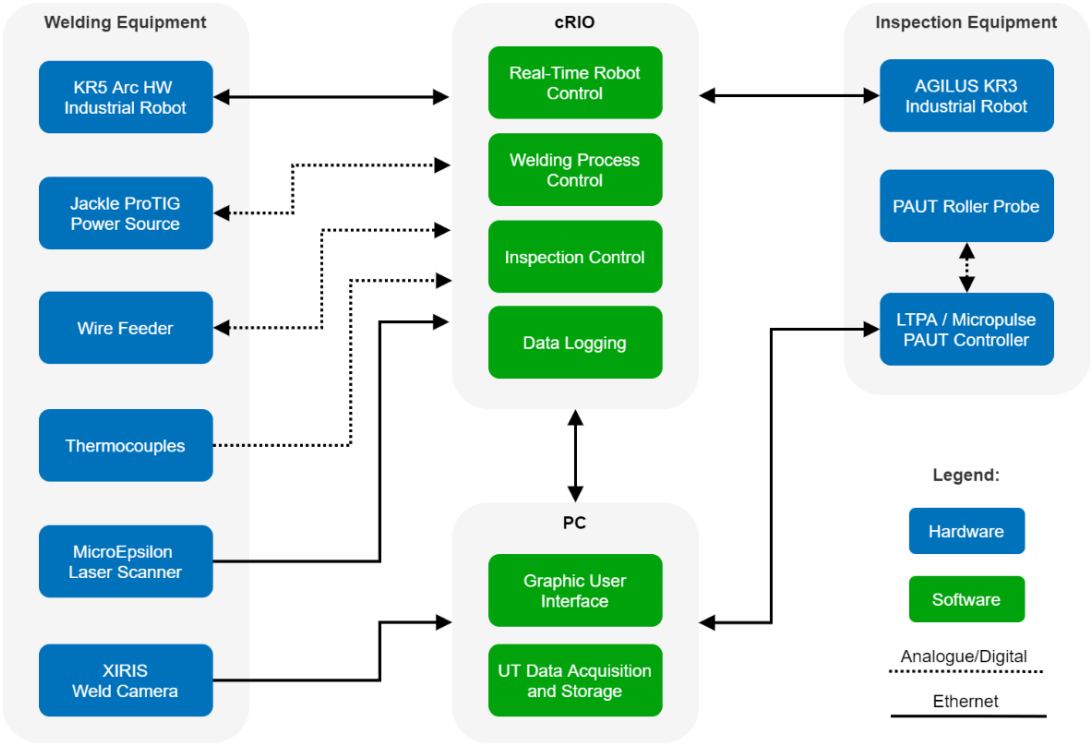

Figure 3.2 Novel sensor-enabled multi-robot welding and in-process NDE system architecture.

A custom end-effector was designed for mounting the welding torch and laser profiler to the robot flange. The modular design in Figure 3.3 was manufactured from Aluminium, which provided a good combination of light weight, durability and sufficient temperature resistance. An ultrasonic wheel probe could also be attached to the end-effector through a 6 DoF adjustable arm which allowed for optimum coupling, whilst offering flexible positioning around the welding torch. The deployment of the wheel probe for in-process ultrasonic thickness measurement is described in Chapter 4.

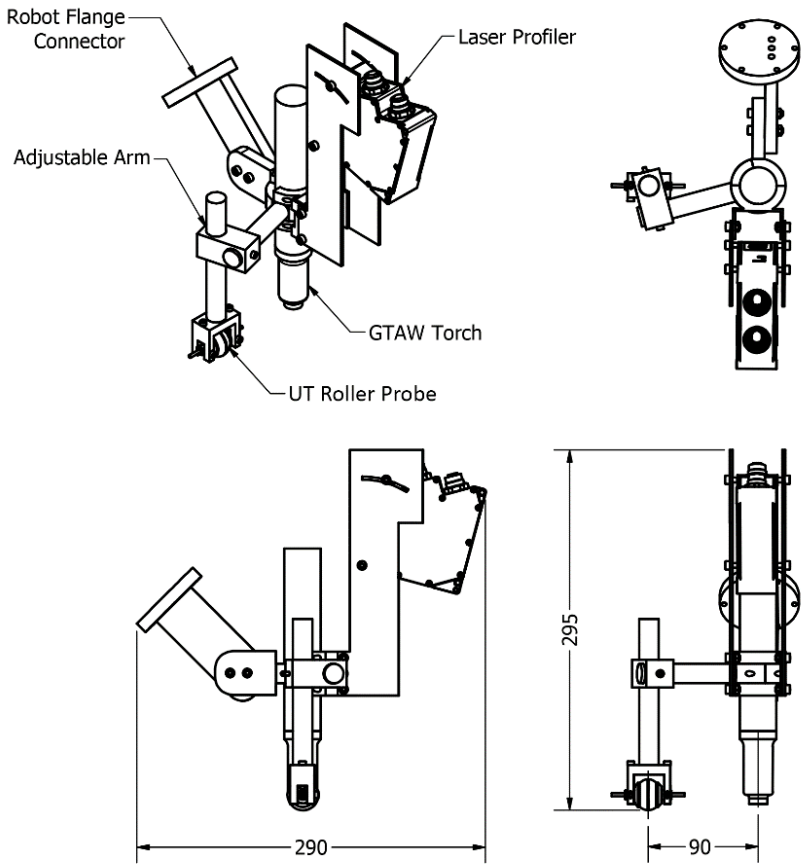

Figure 3.3 Custom robotic end-effector and ultrasonic wheel probe mount technical detail; all dimensions are in mm.

3.3. Software

All software was developed in the cRIO native LabVIEW environment [73] which enabled rapid prototyping, due to the wide range of supported communication protocols and software libraries. The software architecture was built using the JKI state machine [74] and parallel real-time Timed Loops, ensuring program flexibility while also providing reliable and fast response times. Three parallel state machines were responsible for executing the program sequence, controlling the WR and controlling the IR, respectively. The GUI front panel pictured in Figure 3.4 facilitated all user input through button switches and input fields, while allowing to monitor all process variables via Boolean and numeric indicators.

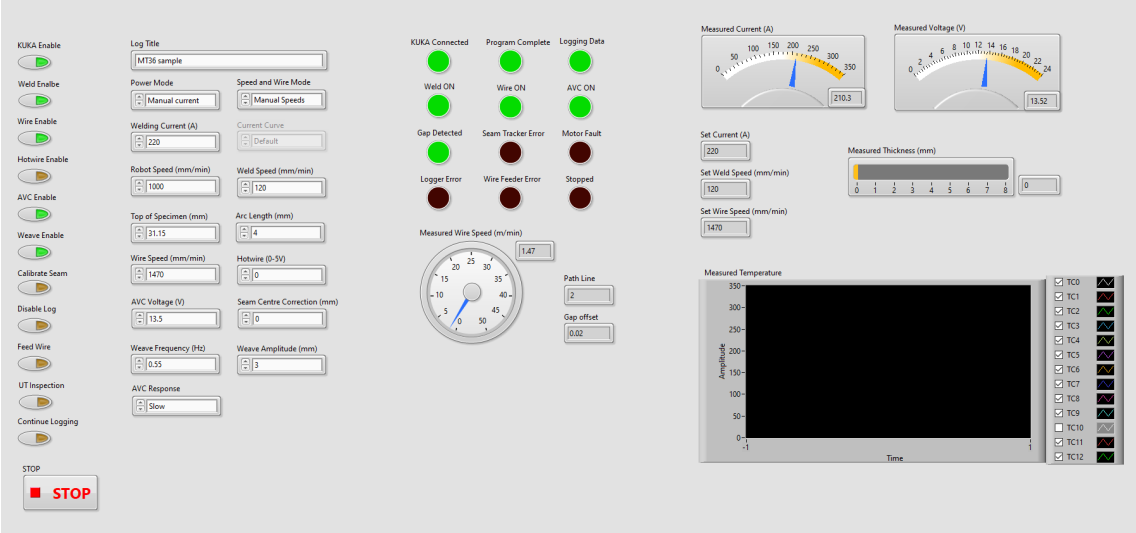

Figure 3.4 LabVIEW GUI for process monitoring and control.

3.3.1. Real-time Robotic Control

The developed real-time robotic control strategy employed full external positional control of the robots. This was achieved through a correction-based RSI motion, meaning that the robot controller did not hold any pre-programmed path, and the robot end-effector position was updated on-the-fly through positional corrections. At every iteration of the interpolation cycle the current position (RIst) and timestamp of the internal clock (IPOC) are sent by the robot controller as an XML string (Figure 3.5 (1)). An XML string response is returned by the cRIO, mirroring the timestamp to keep the connection alive, and providing positional corrections (RKorr) in each axis (Figure 3.5 (2)) which determine where the end-effector will move to over the next interpolation cycle (Figure 3.5 (3)). An additional Boolean variable (Stop) is used to request the termination of the RSI motion by the external system. There are two types of positional corrections – absolute, where the new position is given with respect of the robot base, and relative, where the new position is given with respect to the current position. For example, an absolute correction of 1 mm in the X-axis will move the end-effector to the absolute coordinate X = 1 mm, while the same relative correction will move the robotic end-effector by 1 mm in the positive X-axis direction, irrespective of its current position. Relative corrections were chosen for this body of work, as the smaller magnitude of corrections sent to the robot controller made them safer for use during the development and testing stage.

Figure 3.5 RSI communication between KRC and cRIO via XML string messages.

A welding and inspection robot paths are input by the user as individual points in a table through the GUI, where each row corresponds to a point in the path, and the columns hold the cartesian coordinates for each axis (X, Y and Z) and the rotation around each axis (A, B and C) as shown by the example in Figure 3.6. Additional columns in the welding path table provide control over the process while approaching the target, i.e. an “Arc On” Boolean determines if the WR should be welding, and a “Log On” Boolean enables the data logging. When considering simpler geometries like a plate or pipe butt-weld, the robotic paths can be manually entered as individual point coordinates, for example a straight line weld would only require two points – the start and the end of the weld (i.e. line (3) and line (7) in Figure 3.6). Additional points can also be entered in the weld path

to ensure a sufficient clearance above the workpiece is achieved before and after the weld motion, as shown in Figure 3.7.

	X	Y	Z	A	B	C	Arc On	Log On	
Weld Path									
0	0	3	50	0	90	0	0	0	(1)
0	0	3	0	0	90	0	0	0	(2)
	300	3	0	0	90	0	1	1	(3)
	300	3	50	0	90	0	0	0	(4)
	0	-3	50	0	90	0	0	0	(5)
	0	-3	0	0	90	0	0	0	(6)
	300	-3	0	0	90	0	1	1	(7)
	300	-3	50	0	90	0	0	0	(8)

Figure 3.6 Example path entry for the deposition of two welds.

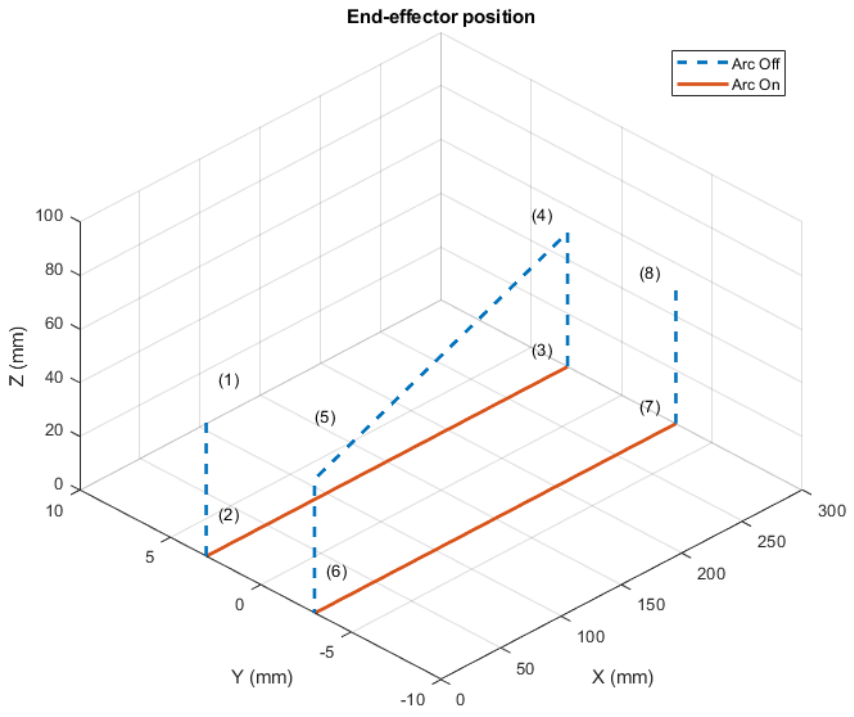

Figure 3.7 Example welding path trajectory for the deposition of two welds.

The weld path input can also be extended to include more sophisticated data as additional columns, for example to choose the welding parameters through a lookup table containing the settings for a root, hot, filling, and cap passes. This would allow the user to import and reuse the parameters from a relevant Welding Procedure Specification (WPS) document alongside the robotic path. More intricate weld paths for complex component geometries can be generated by Computer Aided Manufacture (CAM) or robotic path-planning software and imported into the developed program [75]–[77], as shown by the manufactured autogenous weld pattern in Figure 3.8.

Figure 3.8 Complex pattern created through autogenous GTAW welding for the Images of Research Competition.

3.3.2. Adaptive Trajectory Planning

An on-the-fly calculated trajectory planning algorithm running at the RSI interpolation cycle rate was designed as specified by the process diagram in Figure 3.9. A relative positional correction is sent to the KRC at each iteration of the interpolation cycle, consisting of a linear motion component d_L and an adaptive motion component d_A. The Linear Motion Controller (LMC) generates a straight line trajectory between the current end-effector position P_C and a target position P_T'. It is based on a linear acceleration-cruise-deceleration curve with the setpoint cruise speed V entered by the user. Figure 3.10 demonstrates an example linear motion between two points that are 2 m apart with a setpoint cruise velocity of 2 m/s and an acceleration of 4 m/s^2. In parallel to the LMC, the Adaptive Motion Controller (AMC) generates an instantaneous adaptive correction d_A in response to the sensory input and process requirements. The absolute adaptive correction D_A, which is the cumulative total correction output by the AMC during the adaptive motion, is summed to the current target position P_T taken from the robotic path table to form P_T'.

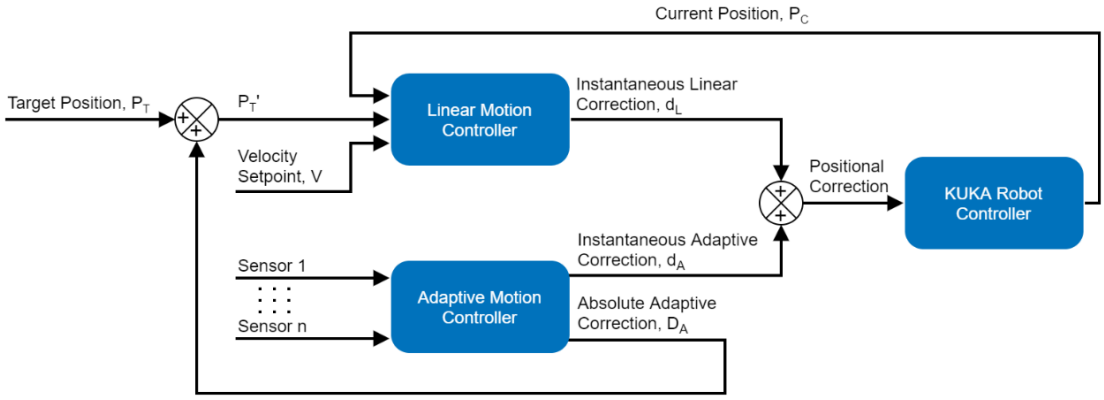

Figure 3.9 Trajectory planning and on-the-fly sensor-based motion correction algorithm.

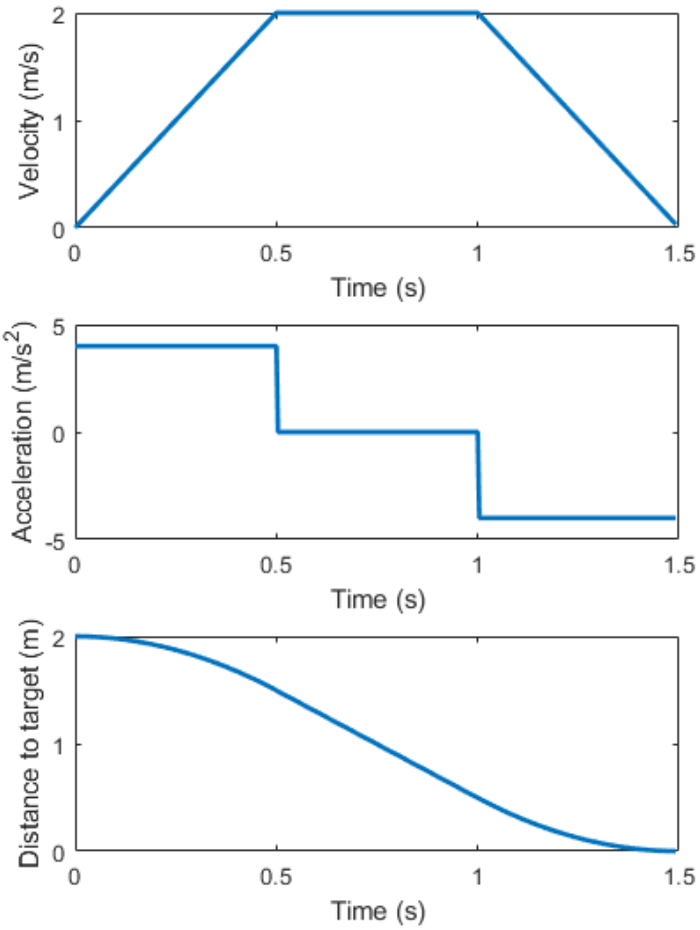

Figure 3.10 Example linear motion between two points that are 2 m apart with a cruise velocity of 2 m/s and a linear acceleration/deceleration of 4 m/s^2.

3.3.2.1. Adaptive Motion Examples

An example linear motion along the X-axis between a starting point P_S and a termination point P_T is shown in Figure 3.11 a). The linear motion velocity vector V_L at an arbitrary point P_0 along the path is always directed towards the target point P_T and is, therefore, parallel and coinciding with the P_SP_T vector. Furthermore, as the P_SP_T vector is aligned with the X-axis, the V_L vector only consists of an X-axis component. In Figure 3.11 b) an example AMC output d_A, consisting of a sinusoidal oscillation in the Y-axis, is summed with d_L before sending the positional correction to the KRC, resulting in a weaving motion between P_S and P_T. However, as the linear motion vector V_L is always directed towards the target P_T, a Y-axis component is introduced at all points that don't lie on the P_SP_T vector, which results in a distorted trajectory. The effects of this distortion become stronger and more evident closer to P_T as illustrated by V_{L0} and V_{L1} in Figure 3.11 b). In order to avoid the distortion in the LMC trajectory caused by the instantaneous correction d_A, the absolute adaptive correction D_A is summed with P_T to give P_T'. This offsetting of the target point ensures that the LMC generated trajectory remains linear as shown in Figure 3.11 c). As a result, a trade-off between target point accuracy and adaptive correction is inherently introduced in the control system.

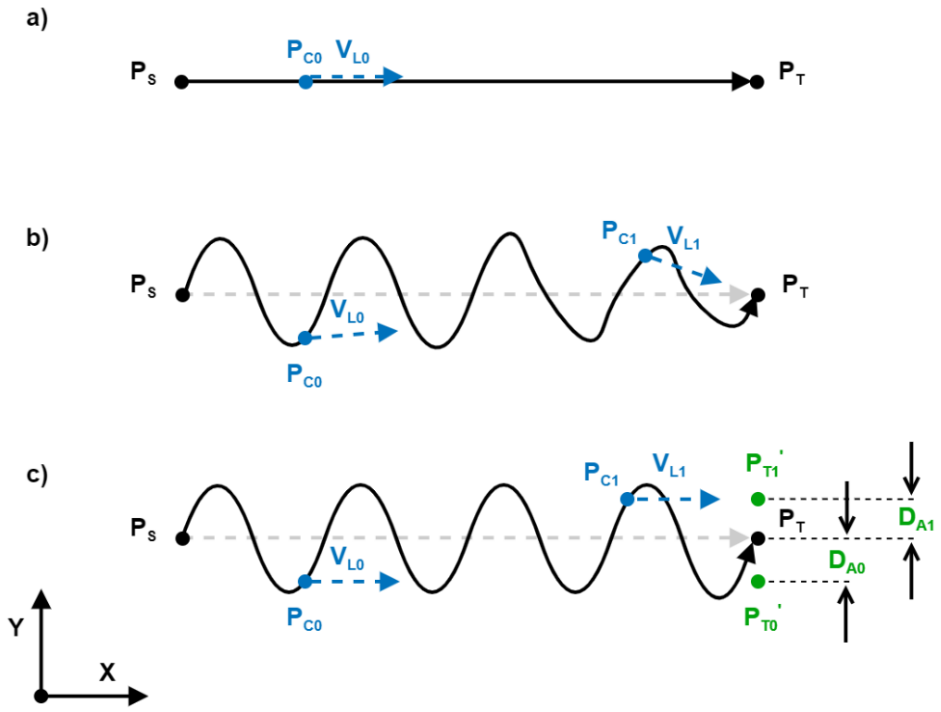

Figure 3.11 a) Example linear motion generated by the LMC; b) trajectory distortion introduced by instantaneous adaptive correction d_A; c) target point offsetting through absolute adaptive correction D_A.

The demonstrated weaving motion is useful in various scenarios, for example in welding, when mimicking the motion of manual welding techniques. Such a weaving motion is generally not achievable through a robotic teach pendant and requires path-planning software. The path-planning software would normally construct the path from a number of fundamental linear and circular motions, which would require a full trajectory recalculation if any of the parameters like the travel speed, amplitude or frequency of weaving need to be modified. In contrast, as the weaving motion is calculated in real-time through the developed approach, its parameters and driving function can be readily changed and updated on-the-fly. This approach can be applied to multiple axes at the same time and can be implemented with multiple sensors. For example, most modern automated

welding power supplies offer the ability to monitor the arc current and arc voltage in real-time, which can be utilised for process control. As the supplied arc voltage in the GTAW process is directly correlated to the distance between the welding torch and the workpiece, it is a suitable sensory input for adaptive motion control. When welding a workpiece that is assumed to be flat, but in reality it has surface height variations, the offset between the welding torch and the sample surface would vary along the weld as shown in Figure 3.12 a), resulting in an inconsistent arc voltage and, therefore, inconsistent weld properties. In order to adapt to the surface height variations, the measured arc voltage can be used as the control variable of a proportional-integral-derivative (PID) control loop, the output of which is an instantaneous adaptive correction applied in the Z-axis. This allows to achieve Arc Voltage Control (AVC), maintaining the welding torch to workpiece distance constant as illustrated in Figure 3.12 b). The demonstrated approach can be applied for a variety of scenarios with sensor input from equipment like laser profilers, force-torque sensors and machine vision cameras among others.

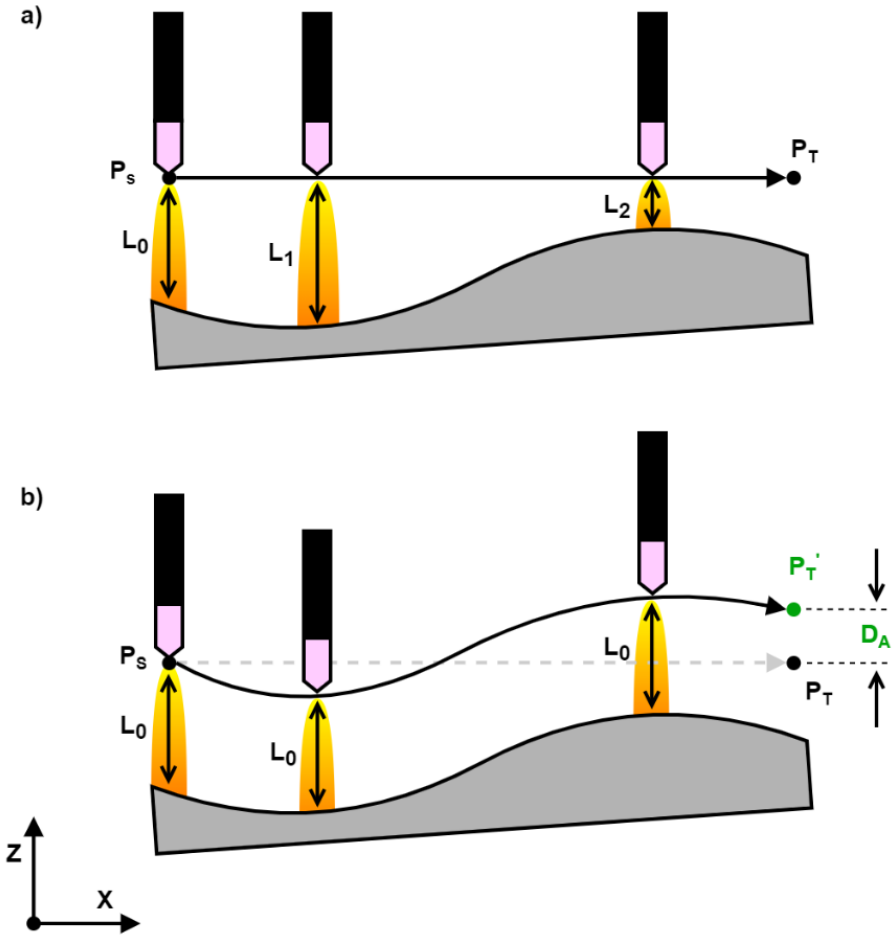

Figure 3.12 Welding of a sample with an uneven surface through: a)linear trajectory; b) linear trajectory with AVC.

3.3.3. Welding Sequence

Before any welding, the position of the workpiece had to be calibrated to allow for the welding path entry with respect to the weld geometry coordinate system shown in Figure 3.13. The first calibration was performed manually, by measuring the distance from the top of the workpiece to the surface of the welding table through digital callipers, which was used to automatically align the origin of the Z-axis with the top surface of the workpiece. The second calibration was performed automatically by the WR using the laser profiler, locating the weld groove and aligning the origin of the Y-axis with the weld groove centreline.

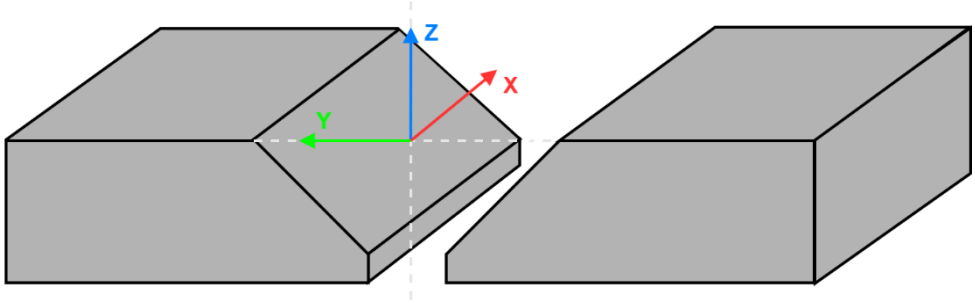

Figure 3.13 Calibrated weld path coordinate system with respect to workpiece and weld groove.

The calibration procedure was performed only once per workpiece, as the samples were fixed to the table using 6-point clamping and their location did not shift with respect to the WR. In applications where an initial calibration of the weld groove is not practical, or where the weld groove is expected to shift between welding passes, the laser profiler output could be utilised for real-time seam tracking through the AMC as demonstrated in Figure 3.14.

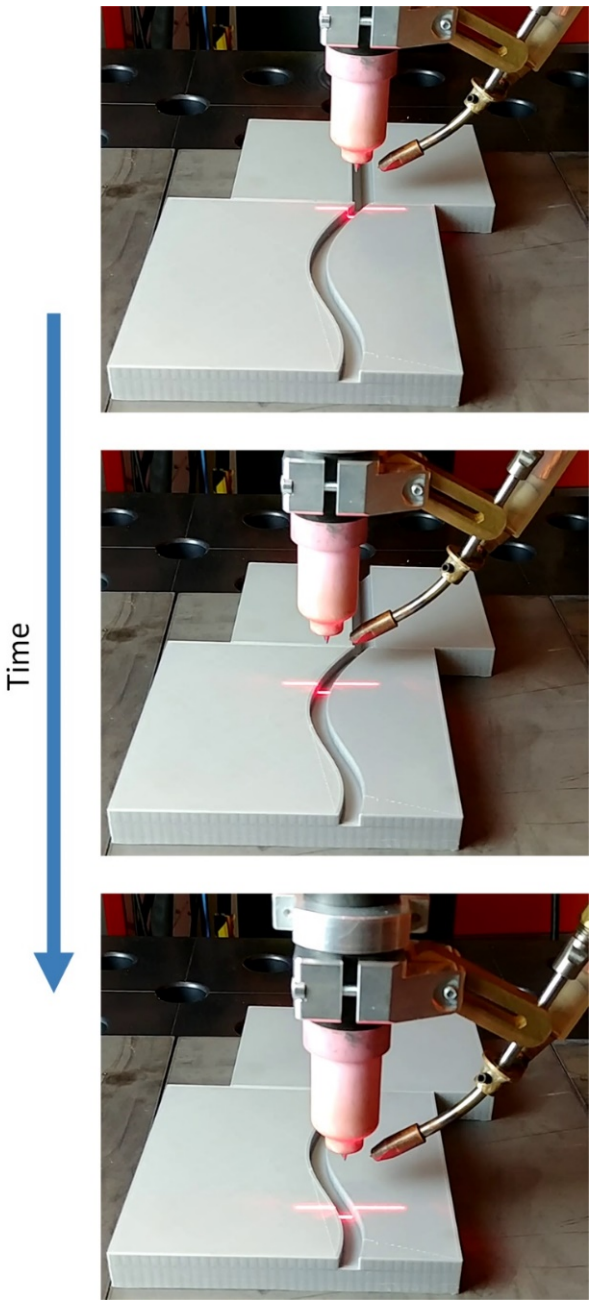

Figure 3.14 On-the-fly seam tracking achieved through laser profiler controlled adaptive motion.

All relevant process parameters and ultrasonic measurements were timestamped and positionally-encoded by the robot position to allow for subsequent analysis. This data was recorded in real-time and was saved in a binary format, which reduced the overall file size. The motion algorithm drove the end-effector to each position in the weld path sequentially. When it reached a position row with an “Arc On” command set to 1, the welding arc was switched on and the WR paused for 2 seconds to allow for the welding arc to stabilise as shown by the positional log in Figure 3.15 a). The wire feeder was switched on at the 3 second mark (Figure 3.15 c) when the weld pool stabilised, followed by the weaving (Figure 3.15 b) and AVC (Figure 3.15 d) which were enabled at the 4 second mark as the wire feed stabilised. Figure 3.15 c) and d) show that the applied positional corrections were effective at maintaining the arc voltage close to the AVC setpoint of 12 V, even when the welding torch was oscillating with respect to the weld groove. When the end of the weld was reached, the filler wire was retracted from the weld pool and the WR paused once again to allow for the post-current and post-flow of the shielding gas over the seam end.

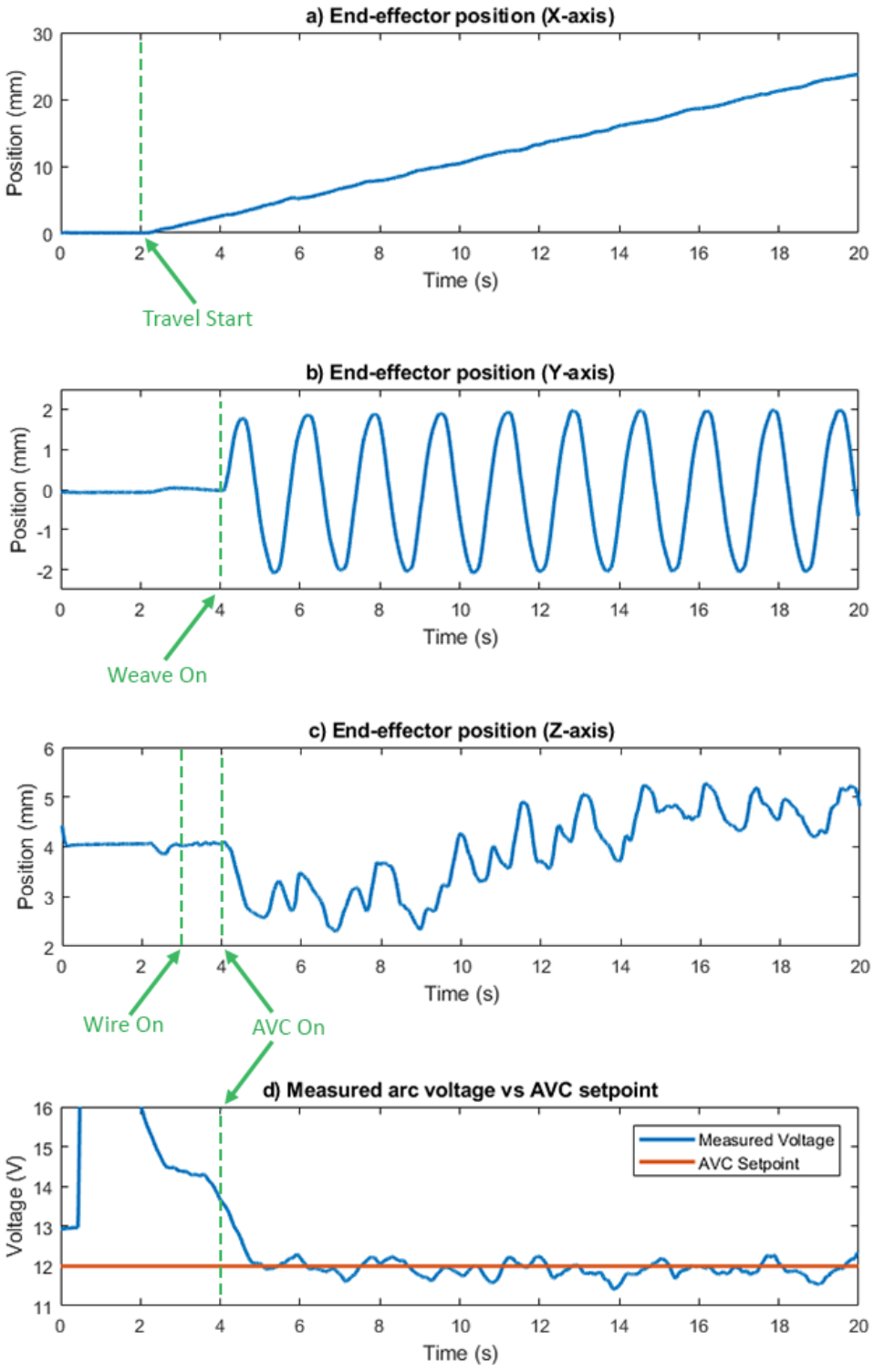

Figure 3.15 Welding sequence demonstrated through logged positional and arc voltage data.

The KR 5 arc HW robot (WR) was specially designed with a hollow wrist for welding applications and as such featured a tension belt drive for 3 of its 6 axes. A study into the accuracy of this specific model [78] had found that as a result of this design, the end-effector suffered a static positional error of 1 mm and a dynamic error of 4.5 mm. This positional instability can be seen upon closer inspection of the robot trajectory in the X and Y axes and was most prominent in the Z-axis, where the end-effector position experienced a "dip" around the 2.5 second mark. The developed motion algorithm has been tested and deployed on a number of more recent KUKA robot models with the KRC 4 controller available in the University of Strathclyde, including the KR3 R540, KR6 AGILUS and KR90. Speeds of up to 2 m/s with an acceleration of up to 4 m/s^2 were achieved, and the positional performance has been found to be more stable. The latest beta version of the software has been extended to allow for external axis control (e.g. a rotary stage) and is currently tested on a wider in-process NDE project in CUE.

3.4. Conclusion

A novel sensor-enabled robotic system for automated welding and ultrasonic inspection was developed and evaluated. The system architecture based around the NI cRIO real-time embedded controller enabled real-time communication, data acquisition and control. A real-time external robotic control strategy for adaptive behaviour, allowing for on-the-fly sensor-based trajectory corrections, was designed and evaluated. The developed system was a key enabler for research in automated welding and in-process NDE.

Chapter 4

On-line Ultrasonic Thickness Measurement For Welding Parameter Control

4.1. Introduction

4.1.1. Fusion Welding Parameters

It is imperative to accurately control the power and energy of fusion welding operations to ensure optimal weld penetration, integrity and process efficiency. Knowledge of the thickness of both parts to be welded is of significant importance when considering optimum welding parameters and subsequent arc power in order to avoid undesirable effects such as defects, distortion, and Heat-Affected Zone (HAZ) abnormalities, and to ensure high production efficiency [79]. In most automated manufacturing scenarios the base material (steel, aluminium, Inconel etc.) is well known, understood and controlled, and hence, can be pre-set or selected prior to initiating work. In traditional fusion welding and manufacturing operations, welders adjust arc power, torch travel speed and wire feed rate manually, dependent on parameters such as welding process, material, part thickness, and welding torch orientation [80].

This can be pre-programmed or inputted to some modern automated welding systems alongside careful part, process and placement tolerance and control. However, such approaches do not support flexible manufacturing or repair operations where tolerances, unconstrained part placement, or part/process tolerances are unknown or varying.

In simpler manufacturing operations, knowledge of constant part thickness allows pre-setting of input parameters and arc power, based on pre-loaded part thickness/welding power synergic curves or operator experience. When considering complex manufacturing, operations with parts of varying thickness requires either accurate pre-measurement, control and fixturing, or operator skill in manual operations to compensate for such variations. Examples of applications involving changing and differing part thickness include design-optimised structures, where light-weighting through the use of thinner sheets is desired alongside high-strength thicker sections in key areas – these would include multi-thickness sheet arrays used in modern large-section fabrications in the shipbuilding, energy and defence sectors. Additional applications, in both manufacturing and asset repair applications, include tapered sections and varying thickness joints due to manufacturing and plate tolerances, corrosion and thickness loss.

The desired arc power for producing a satisfactory joint is dependent on many variables such as parent material, joint preparation, and material thickness. Therefore, in samples with thickness variations the arc energy would need to be adjusted on-the-fly to ensure adequate arc energy is maintained. Furthermore, the wire feed rate would also need to accommodate changes in part thickness and travel speed in order to supply a consistent flow of filler material to the joint.

4.1.2. Automated Thickness Measurement

Automated thickness measurement of the parts to be joined during the welding operation presents the opportunity to ensure adaptive and optimum welding parameters for the parts under fusion. Such a technique offers benefits for both manual and automated welding operations in terms of final product integrity, production rate and reduced re-work. The opportunity exists to employ a thickness measurement system to provide feed-forward control of the welding parameters in samples of changing thickness. Such a system would require a lower computational complexity when compared to structured light systems that employ 3D calculations and machine learning to measure and control the weld pool size and subsequent penetration depth. Moreover, a feed-forward thickness measurement could be integrated with a feed-back control system, using suitable weld sensors such as structured light systems [34] or ultrasonic phased array [81] so that the deposited weld can be measured, verified and controlled, providing optimum process automation and part quality. Furthermore, an on-line thickness measurement system would complement a weld penetration control system as an additional sensory unit, as the thickness measurements would provide an accurate setpoint for the desired penetration depth.

While, optical laser systems have been shown to detect and compensate for a variety of weld disturbances such as variations in gas flow rate, root opening and heat transfer conditions, as discussed in Chapter 2, they have not been deployed on samples with thickness variations. Furthermore, as all optical methods require a direct line of sight to the weld pool and weld seam, they are not suitable for some applications like SAW. Although optical laser systems can provide joint preparation profile information and

subsequently infer part thickness in open joint configurations, when considering close knit or butt joint configurations, such surface inspection techniques are often unable to provide reliable part thickness measurements. Furthermore, such weld bead and weld pool measurement techniques provide useful sensory inspection information on the surface, but they do not perform any internal or sub-surface measurement. In separate industrial applications such as post-build NDE, internal imaging of parts and components is commonly undertaken using UT not only to provide internal information on the part but also, with knowledge of the speed of sound in the material, the thickness of the part. Such wall thickness measurements can be taken in-situ and can be utilised for process control [82], [83] in a feed-forward architecture for optimised weld penetration for a given plate thickness.

Thickness mapping is used extensively in inspection and NDE applications where measured information relates to corrosion loss and remaining life of the components and structures. The two main methods for thickness mapping are the UT and EC techniques. EC, and more recently Pulsed EC, methods based on the electromagnetic induction principle ascertain sample thickness through a variation of measurement coil inductance [84]. EC testing is fully non-contacting, making it attractive for welding process, but sensitive to changes in lift-off distance and local changes of both material conductivity and permeability [85], [86]. Furthermore, the high electric current and EMI in fusion welding (usually in the range 100 A to 300 A) are likely to interfere with the low-current EC measurements. Traditional Ultrasonic Thickness Measurement (UTM) sensors, on the other hand, are particularly suitable for thicker materials. Through reference calibration

against a known thickness, and the fact that probe frequency and material wave velocity is nominally constant at a given temperature, the thickness of the material can be ascertained from back-wall time-of-flight measurement. Such thickness measurement instruments are commercially available with high accuracy options reaching a resolution of 0.001 mm [87]. As conventional UT sensors utilise a liquid couplant for energy transfer from transducer to part, challenges related to maintaining optimal stand-off, sufficient couplant and orientation to the surface limit their deployment in automated applications. Wheel or roller ultrasonic probe designs [88] feature an outer acoustically matched conformable tire that supports wave propagation into the part with reduced or no couplant requirements. This, along with their ability to roll along a surface, ensuring optimum sensor-surface perpendicularity, makes them ideal for automated applications [76], [89].

This chapter presents contributions to the field of advanced manufacturing through real-time process control of automated fusion welding parameters based on simultaneous forward-looking ultrasonic thickness mapping. A proof-of-concept demonstrator is introduced and subsequent characterisation of system performance is evaluated.

4.2. Experimental Method

4.2.1. Hardware

The purpose designed automated GTAW welding cell introduced in Chapter 3 was configured for in-process ultrasonic thickness measurement, as shown in Figure 4.1. Although the GTAW process was implemented due to equipment availability, the measurement and control system could be readily deployed and replicated for other welding processes such as GMAW and SAW. While modern GMAW welding power sources have synergic and parametric control of arc power and wire speed based on material thickness, this is less common on GTAW power sources which typically accept control directly of desired arc current. In traditional GTAW the general convention on the current required to sufficiently fuse a joint increases non-linearly with increasing material thickness [90]. Additionally, the optimum arc current for a given joint is affected by many parameters such as material, weld type, joint configuration and welding torch design. Therefore, to sufficiently control arc current, a suitable real-time conversion strategy from measured material thickness was researched, developed and characterised.

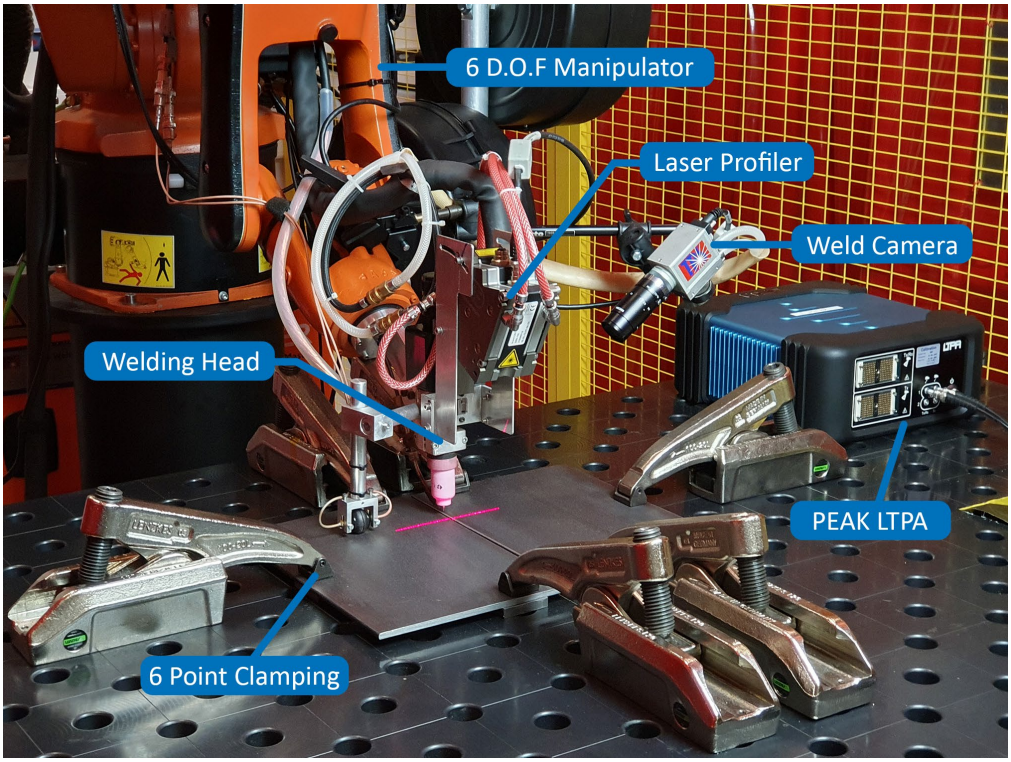

Figure 4.1 Automated GTAW welding cell configured for feed-forward control of welding parameters through in-process ultrasonic thickness measurement.

4.2.2. Sample Manufacture

To validate the concept, characterise the performance of the control method, and develop the parameter relationships, a number of sample geometries were considered. Mild steel plates (S275) with a nominal thickness of 6 mm were selected for stock material, as the material is commonly used and the specific thickness could be butt-welded in a single pass using the available GTAW setup. The two sample geometries shown in Figure 4.2 were created using the Computer Aided Design (CAD) software Autodesk Inventor [91]. A calibration sample geometry was designed to feature a continuous slope ranging from the full thickness of the plate, to a 33 % reduction of wall thickness, decreasing at a rate of 10 mm per 1 m.

The validation geometry weld profile was designed to feature sections with various thicknesses between 6 mm and 4 mm, where the wall thickness was increasing in some regions, and decreasing in others, at a rate of 30 mm per 1 m. 3D models of the two samples were imported into the CAM software Mastercam, which allowed to manufacture the samples on a 3-axis Computer Numerical Control (CNC).The final samples had a dimensional deviations of up to 0.2 mm due to the machining process, and up to 0.1 mm due to variations in the stock material.

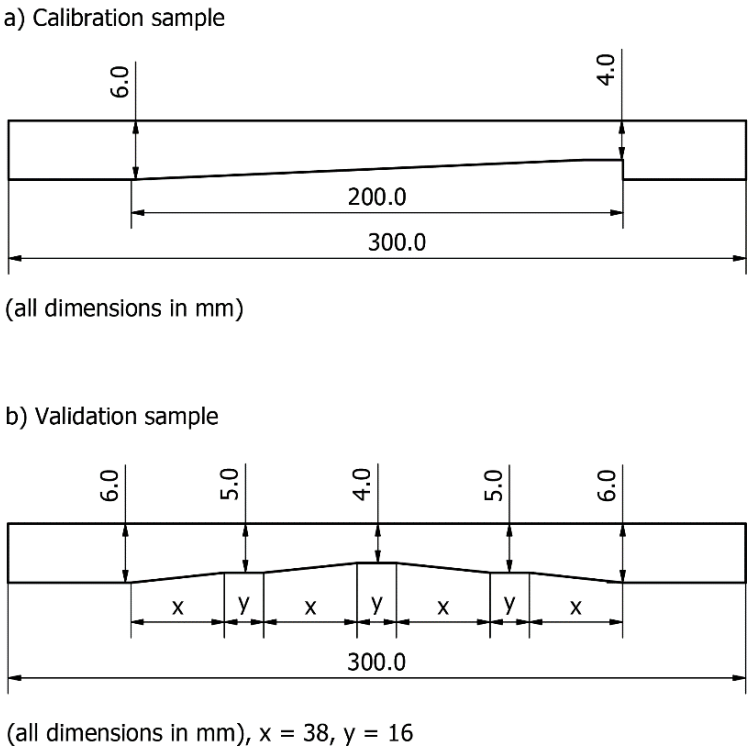

Figure 4.2 Designed sample geometries for a) calibration trials; b) validation trials.

4.2.3. Ultrasonic Thickness Measurement

An EddyFi 5 MHz split-crystal dry coupled ultrasonic wheel probe was chosen, as it is capable of measuring thicknesses between 2.5 mm and 100 mm [92]. The probe was fitted with high-temperature resistant cables and was attached to the robot end-effector as demonstrated in Figure 4.3.

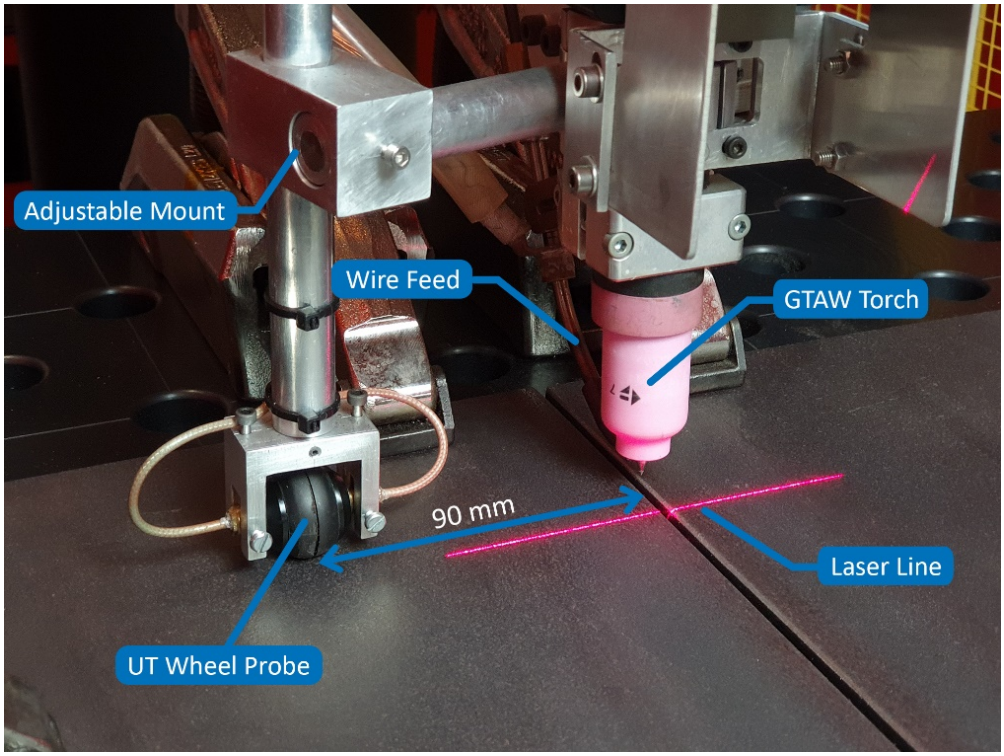

Figure 4.3 Custom robotic end-effector for real-time feed-forward thickness measurement based control of the GTAW process.

The thermal propagation during GTAW welding across the range of applicable thicknesses was captured by measuring the surface temperature using a FLIR infrared thermal camera. The measured temperature profile in Figure 4.4, showed that there was no significant increase in surface temperature at a distance of 60 mm or more to the side of the welding torch, as measured in the thinnest section of the sample (4 mm thick).

Therefore, the ultrasonic wheel probe was not subjected to any hazardous temperatures, capable of damaging the piezoelectric transducer (usually 60º C or above), as it was positioned at a distance of 90 mm to the side of the welding torch. Moreover, as all ultrasonic measurements were taken at a location where the material was at uniform temperature, no measurement error arising from to changes in the speed of sound, due to temperature, were expected.

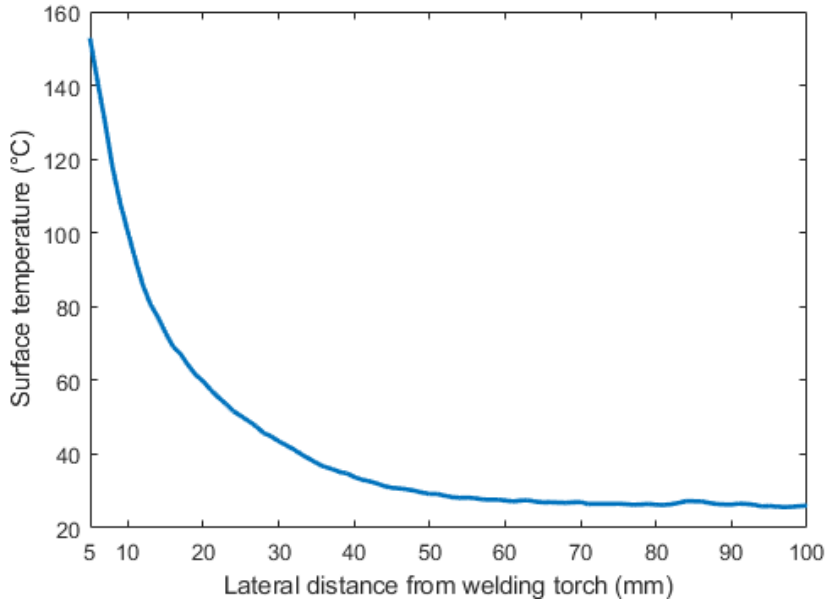

Figure 4.4 Surface temperature of mild steel plate during GTAW fusion welding. Measurement was captured at a section, where the thickness of the plates was machined down to 4 mm.

The transducer required no external liquid coupling, as it consisted of two solid acoustically matched rubber tyres, rotating around a transducer housing, to allow propagation of the transmitted compressional wave and receive signals into, and from, the base material (Figure 4.5 b) [76]). Internal coupling between the transducer and rubber tyre was achieved by a small amount of machine oil. The wheel probe had an approximate footprint size, or lateral minimum spatial resolution, of 8 mm.

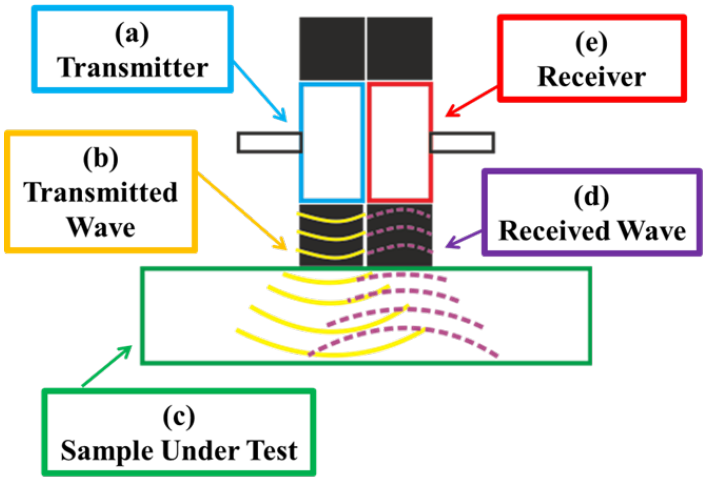

Figure 4.5 Diagram of split piezoelectric crystal ultrasonic wheel probe.

As found in [76], due to the compressive nature of the wheel probe tyre and the difference in sound propagation velocity through the tyre and base material, accurate calculation of the thickness of the sample based on conventional time-of-flight information between the transmitted pulse and the first back-wall echo return was unsuitable. This meant that any variations in contact force, and the resulting compression/expansion of the tyre, would lead to a decrease/increase of the distance travelled by ultrasonic waves in the rubber, which would fundamentally shift the location of the first back-wall echo. Therefore, the corresponding thickness of the base material was determined using successive back-wall echoes, with three or more successive echoes utilised for averaging purposes.

Moreover, small variations in coupling between the tyre and surface could arise from reduced tyre to surface contact pressure, based on variations of robot end-effector to surface height variations, local surface anomalies and rubber tyre wear and tear. These variations of coupling level yield corresponding changes in the multiple back-wall echo amplitudes, with poorly coupled instances providing reduced amplitudes. The minimum

peak detection amplitude of each back-wall echo must, therefore, take into consideration the coupling efficiency and the amplitude of waves physically transferred into the base material.

Delayed time gating of the received pulses excludes the initial trigger of the firing pulse and removes the valueless portion of the captured data, corresponding to the wave propagating through the tyre. Therefore, the largest peak in the acquired time window corresponds to the first back-wall echo, and each following peak corresponds to an internal reflection of the ultrasonic wave. Considering the attenuative nature of metallic materials, successive back-wall echoes are expected to have reduced amplitudes as depicted in Figure 4.6 [76].

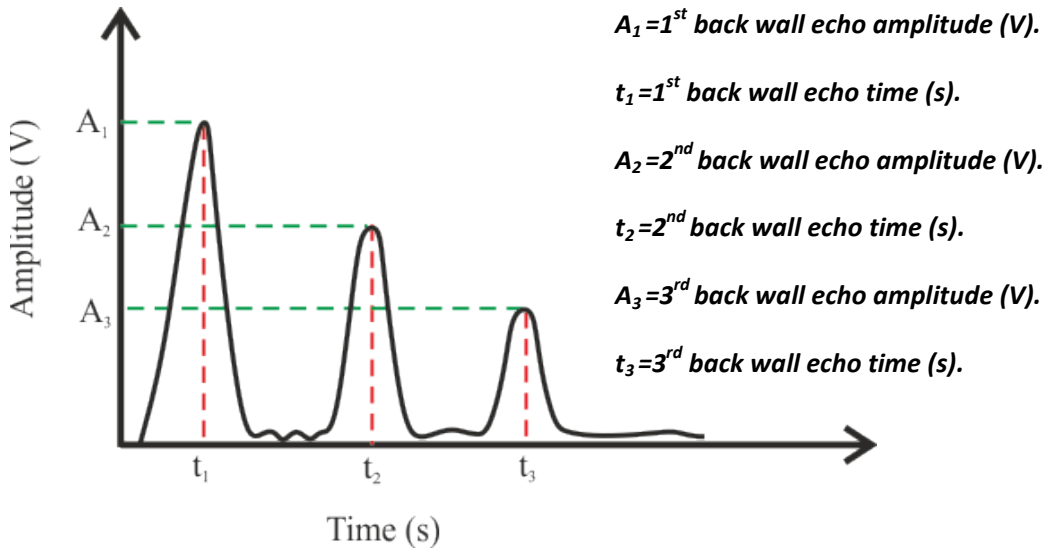

Figure 4.6 Material thickness measurement based on time-of-flight of ultrasonic back-wall echoes.

The thickness of the tested material if, for example using three back-wall echoes, can be calculated through (4.1):

$$m_t = \left(\frac{v_c \times (t_3 - t_1)}{4} \right) \tag{4.1}$$

Where m_t = material thickness (mm), v_c = Speed of sound in material (mm/s), t_1 = time index of 1st back-wall echo (s) and t_3 = time index of 3rd back-wall echo (s). The peak detection developed for this body of work, in terms sensitivity and robustness, adapts for variation in the amplitude of the actually transmitted wave and the subsequent amplitude of the first and a number of repeat back-wall echoes. The algorithm and technique implemented in this paper required real-time calculation of material thickness for in-the-loop correction of welding parameters.

4.2.4. Acquisition and Signal Processing

The wheel probe transmitter and receiver were driven via the PEAK LTPA, which was configured to acquire 8-bit rectified A-scans at a Pulse Repetition Frequency (PRF) of 20 kHz. 128 sample averaging and a 3 MHz to 15 MHz hardware bandpass filter were employed to reduce the electromagnetic noise emitted from the welding equipment and robotic manipulator. All received and recorded raw ultrasonic signals were digitised and transferred over Ethernet to the cRIO controller for further processing. Envelope detection was implemented using an Equiripple low-pass filter with a pass frequency of 3.9 MHz and a stop frequency of 4 MHz. The peaks of the material back-wall reflections were detected using an adaptive detection threshold, in order to minimise the effect of any

variations in coupling. The threshold utilised process feedback and was set as a proportion of the amplitude (25 %) of the largest peak detected in the previous A-scan, in order to capture a number of successive echoes. A minimum value of 10 % screen height was utilised for the adaptive (in the axis of direction of travel) threshold, to provide against falsely identifying system noise as back-wall echoes, in case no back-wall echoes were detected. Figure 4.7 shows the peak detection and thickness measurement from a processed ultrasonic A-scan.

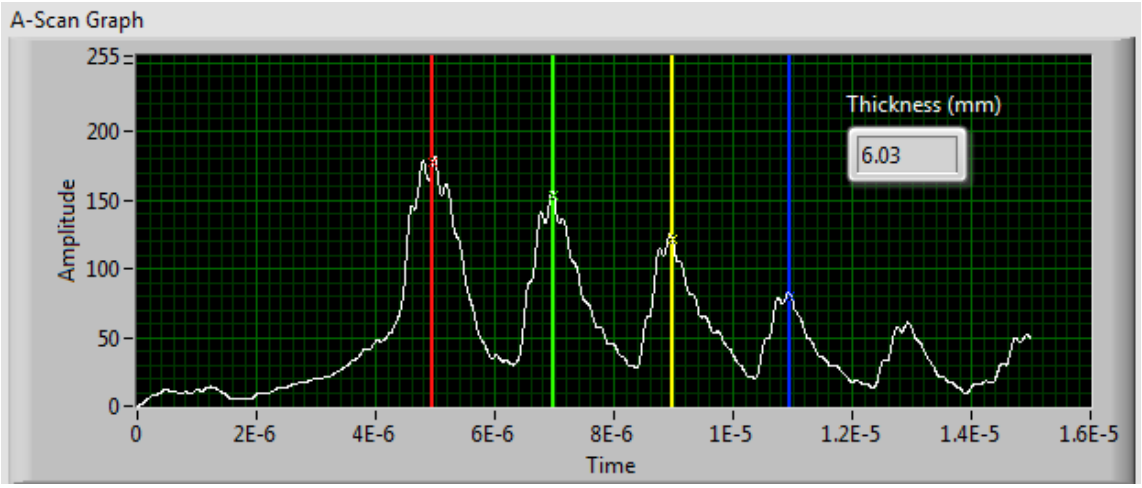

Figure 4.7 Ultrasonic thickness measurement in LabVIEW.

The developed code allowed for two or more peaks to be used for thickness calculation, as long as they satisfied a minimum 2nd derivative value condition. This was a measure of peak "sharpness" and ensured that lower amplitude peaks corrupted by noise did not affect the accuracy and repeatability of the final thickness measurement. If fewer than two peaks satisfied this condition, meaning that material thickness could not be inferred from the ultrasonic signal, the last valid measurement was used for control purposes until this condition was once again satisfied. In the final step of the signal processing, a median

filter of 128 samples was applied to the measured thickness, removing any outlier measurements. The measured thickness was then used to calculate in real-time the welding current, welding torch travel speed and filler wire feed rate through pre-established relationships. The complete control strategy flowchart can be seen in Figure 4.8.

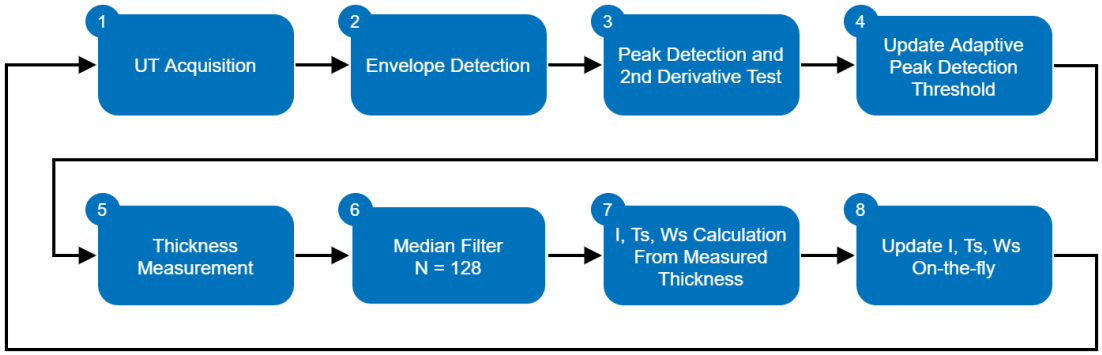

Figure 4.8 Process flowchart for feed forward control of welding parameters through on-line ultrasonic thickness measurement.

As discussed in Chapter 3, the welding current was externally set in the welding power source, while the torch travel speed and wire feed rate were internally set in the cRIO, updating the setpoints of the real-time motion control loop and PID motor control loop, respectively. As the acquisition and signal processing parameters were constant, the only variable that affected the spatial measurement resolution was the torch travel speed. Given the used PRF of 20 kHz, 128 sample averaging and the maximum welding torch speed used in the trials of 172 mm/min (based on the maximum applicable weld plate thickness of 6.0 mm), the surface length covered by a single measurement could be calculated by Equation (4.2):

$$spatial\ resolution = \frac{T_s * N_{avg} * N_{med}}{PRF * 60} \tag{4.2}$$

Where T_S = travel speed (mm/s), N_{avg} = number of acquisition averages and N_{med} = median filter length. Therefore, the minimum spatial resolution for weld parameter control was 2.3 mm in the worst case. The response time of the welding equipment should also be considered and accounted for in very high-accuracy applications. The position of each thickness measurement was encoded through the robotic manipulator and was logged from the cRIO at 12 ms intervals. As the distance between the wheel probe contact point and the robotic welding torch in both X and Y axes was known and constant, each measurement was recorded relative to the correct location along the sample.

4.2.5. On-line Thickness Measurement

To determine the influence of the environmental noise introduced by the GTAW process, the thickness of each sample was measured both off-line (Figure 4.9 a), before any welding had commenced, and on-line (Figure 4.9 b), during the welding process. The Root Mean Square (RMS) difference between the on-line (Figure 4.10 solid line) and off-line (Figure 4.10 dashed line) measurements was 0.02 mm with a maximum discrepancy of 0.07 mm at any point. The above values take into account the measurement repeatability error introduced by various factors such as irregular tyre wear, robotic positioning error, EMI and background noise. Therefore, robust the thickness measurement strategy was suitable for on-line deployment.

a) Off-line thickness measurement

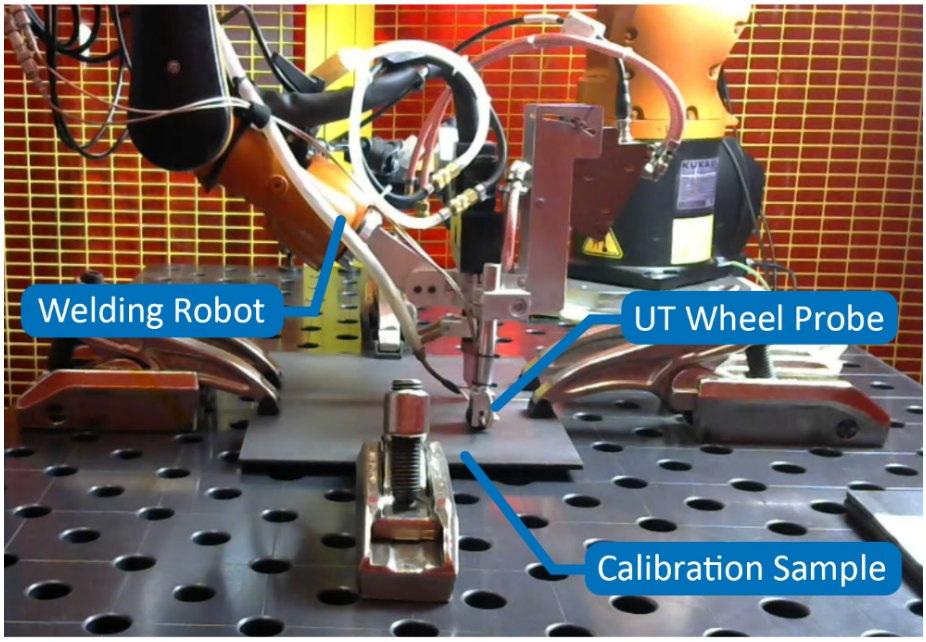

b) On-line in-process thickness measurement

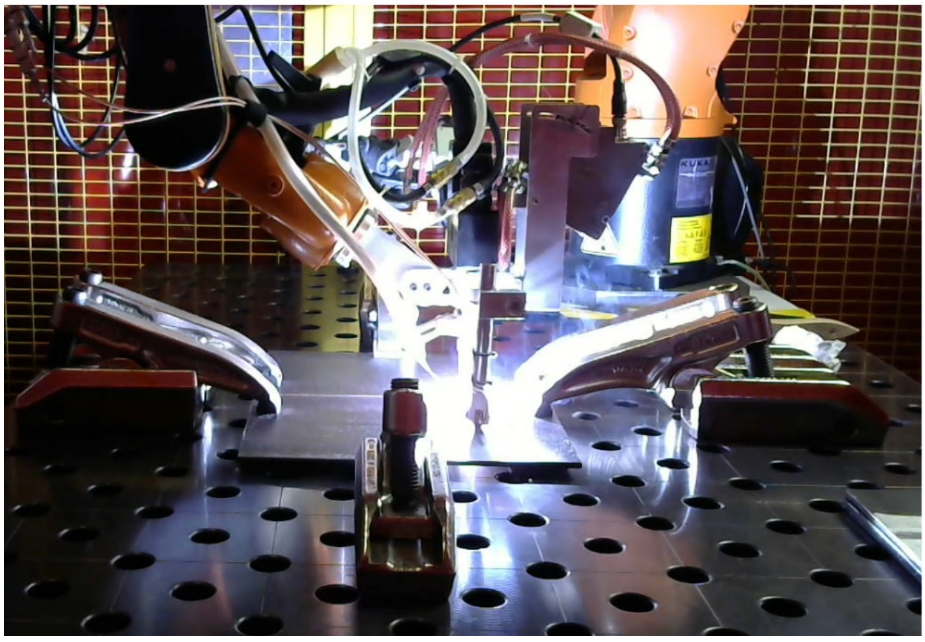

Figure 4.9 Video frame still images capturing a) off-line thickness measurement for verification and b) on-line in-process thickness measurement and feed-forward control of welding parameters.

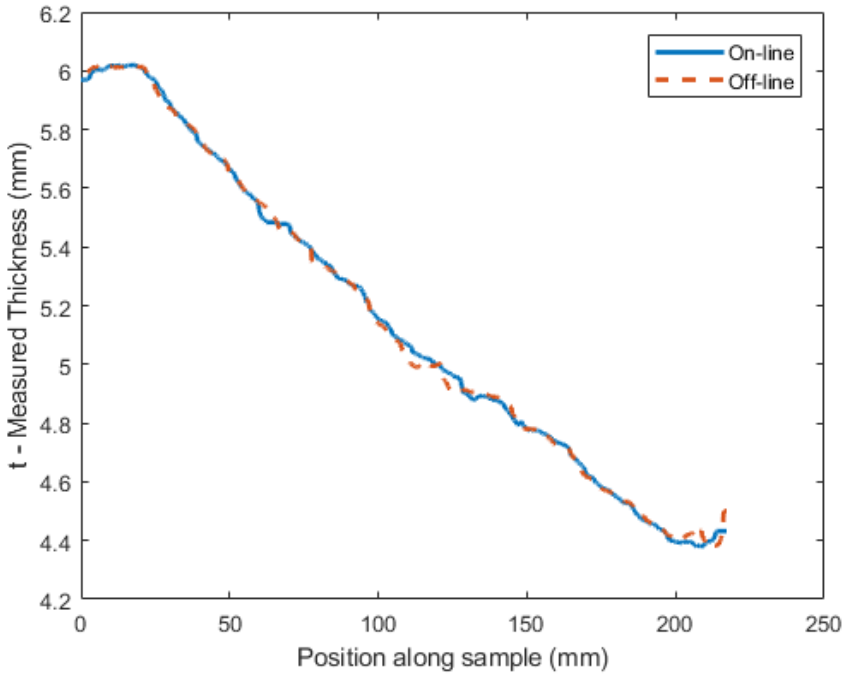

Figure 4.10 On-line (solid) and off-line (dashed) ultrasonic thickness measurement of calibration sample.

4.2.6. Control Strategy And Calibration

A control strategy was designed to demonstrate how the arc current, torch travel speed and wire feed rate can be updated on-line based on the measured sample thickness. Data from available reference thickness current ranges for manual GTAW butt-welding of mild steel [90] was used as initial starting points for developing the arc current-thickness parameter relationship (Figure 4.11, marked with ‘o’ and ‘x’). Due to material thickness having a direct nonlinear relationship to the arc current, a polynomial was selected to best fit all reference current range data points. Through inspection of the data in the MATLAB software package[93] it was established that a third order polynomial (Figure 4.11, dashed line) sufficiently captured the overall curve trends without overfitting the reference data points.

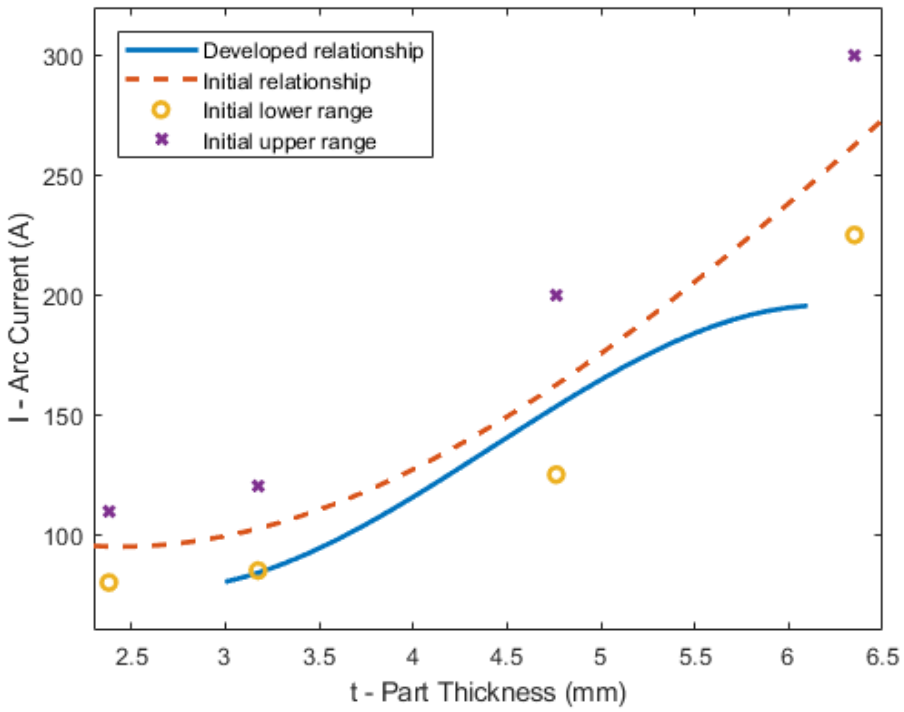

Figure 4.11 Reference arc current values for manual GTAW butt-welding of mild steel [29] represented as a range with lower bound (marked with 'o') and upper bound (marked with 'x'). A third order polynomial (dashed line) was fitted to the reference points and was used as a starting point for the final arc current-part thickness relationship(solid line), which was developed through incremental manual adjustments based on experimental results.

The next step of the calibration process was to develop a control strategy for the torch travel speed. To reduce the number of variables and overall calibration complexity, it was decided to control the torch speed based on the arc current through a linear relationship, as the arc current was already directly calculated from the measured sample thickness. Therefore, in order to establish the initial linear arc current-torch speed relationship, two reference points were required. To obtain these, preliminary butt-weld trials with 6 mm and 3 mm thick samples were carried out. The arc current was set based on the initial thickness-arc current curve, and the torch travel speed and wire feed rate were manually

adjusted until a satisfactory weld seam was achieved for both thicknesses. A linear function was then fitted between the two established torch travel speed points to generate the initial torch travel speed-thickness relationship. Finally, it was decided to maintain the wire feed rate proportional to the plate thickness and torch speed, in order to provide a weld cross section area that is consistent and appropriate for the material thickness.

The sloped calibration samples were welded in the direction of decreasing thickness so that the effects of the parameter relationships could be observed with respect to the reducing sample thickness. A number of calibration trials were carried out, each followed by a close inspection of the produced weld seam. Visual inspection was suitable for determining the overall weld quality, as this work was focused on demonstrating the adaptive deposition method, and not at obtaining any specific metallurgical qualities of the produced welds. Thus, the welding parameter relationships were iteratively updated based on a number of factors, e.g. amount of weld penetration, presence of undercut or burn-through, visible size of the HAZ and weld bead size. For example, if the deposited weld seam was consistent for thicknesses between 6 mm and 5 mm but then featured an excessive penetration for thicknesses below 5 mm, the polynomial coefficients for obtaining the arc current would be manually adjusted, optimised and recalculated in MATLAB, in order to provide a lower arc current for thicknesses below 5 mm. This process was repeated until a consistent weld seam and penetration were successfully achieved along the full length of the weld, as shown in Figure 4.12.

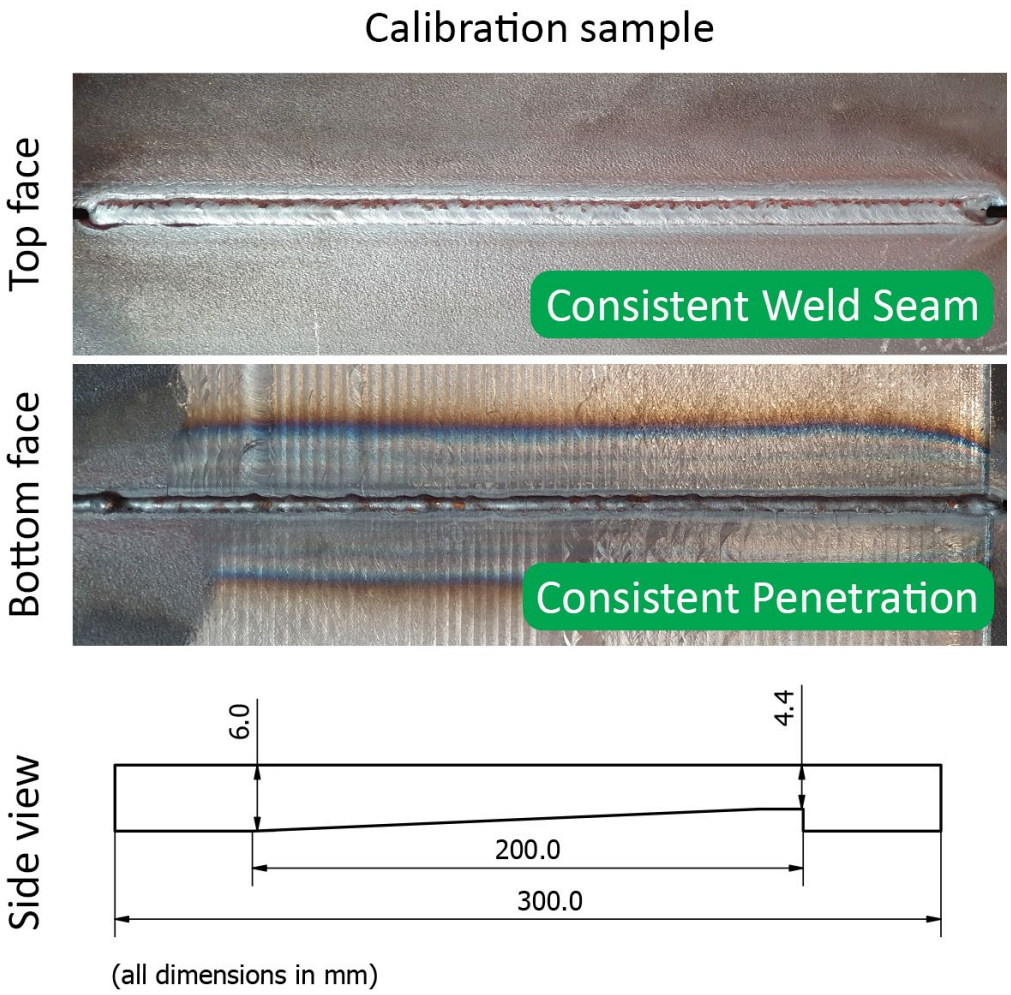

Figure 4.12 Calibration GTAW butt-weld of two mild steel plates with a machined slope representing wall thickness loss from 6.0 mm to 4.4 mm (measured using calibrated digital callipers).

The final forms of the developed welding parameter relationships after the calibration procedure was complete are shown in Equations (4.3), (4.4) and (4.5), and the final arc current-thickness curve is plotted in Figure 4.11 (solid line).

$$I = -5.4 * t^3 + 71.58 * t^2 - 265.58 * t + 379.4 \quad (4.3)$$

$$T_S = 31.5 + 0.69 * I \quad (4.4)$$

$$W_S = 3.6 * t * T_S \quad (4.5)$$

Where I = welding current (A), t = measured part thickness (mm) and W_S = filler wire feed rate (mm/min). Using the produced relationships, a preliminary estimate for arc current, torch travel speed and filler wire feed rate could be determined for GTAW butt-welding a given thickness of mild steel plates between 4 mm and 6 mm.

4.3. Validation and Results

Further trials with the validation geometry samples were carried out in order to test the developed parameters with a more realistic workpiece and to evaluate its benefits over traditional automated welding systems. A control sample was welded with constant parameters set based on a single digital calliper measurement of the full plate thickness (6.1 mm) and Equations (3), (4) and (5), resulting in an arc energy of 1.2 kJ/mm. Figure 4.13 shows that the suboptimal arc energy used in the control sample has caused an undercut of the weld seam, and, in the thinner middle section, weld burn-through in the form of holes, as seen from the top face. Moreover, paired with the constant wire feed rate, the bottom face of the produced weld was irregular with an excessive root penetration.

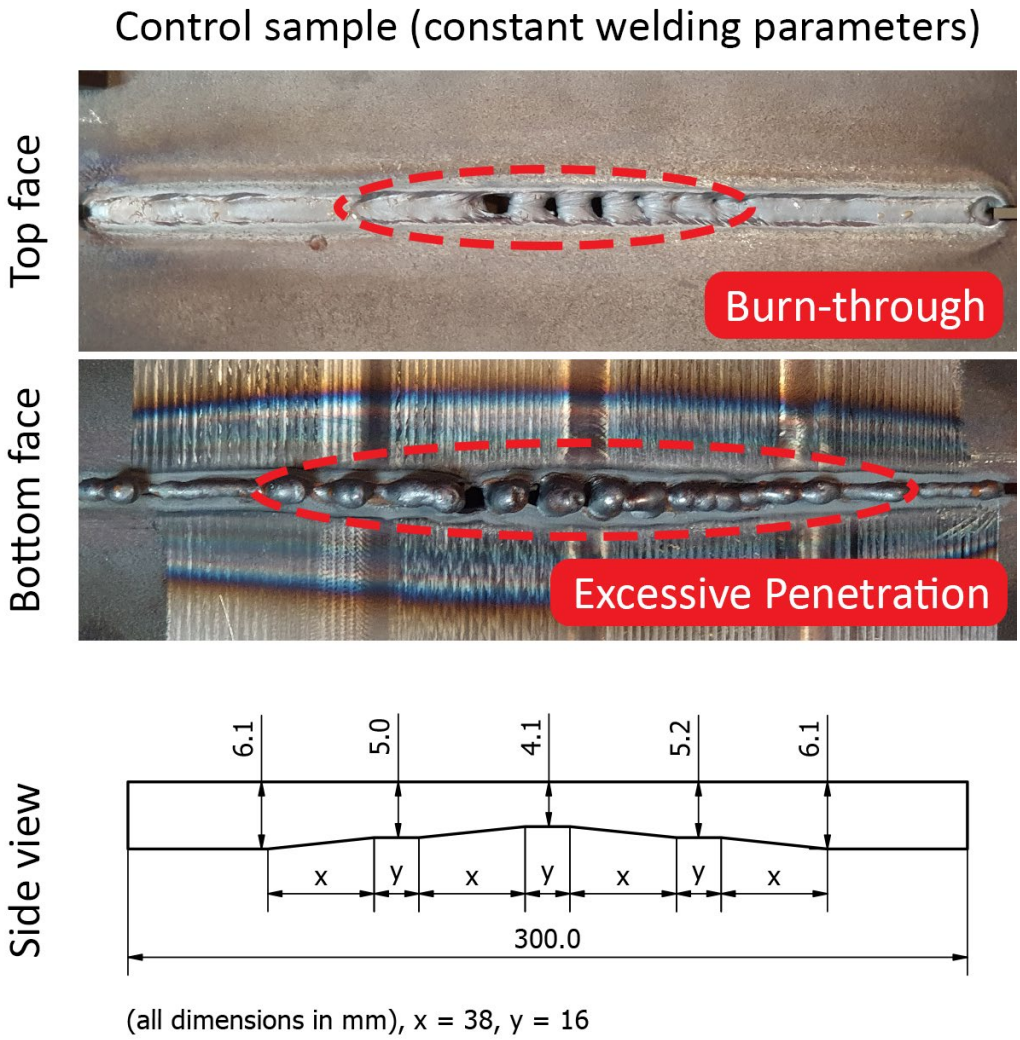

Figure 4.13 Control sample manufactured with constant welding parameters assuming a constant plate thickness of 6.1 mm, as obtained by a single point measurement with calibrated digital callipers

In contrast, the manufactured validation sample employing on-line thickness measurement in Figure 4.14 exhibited both a consistent weld bead and root penetration. This was a direct result of the adaptive welding parameter control, enabled by the ultrasonic wheel probe measurements.

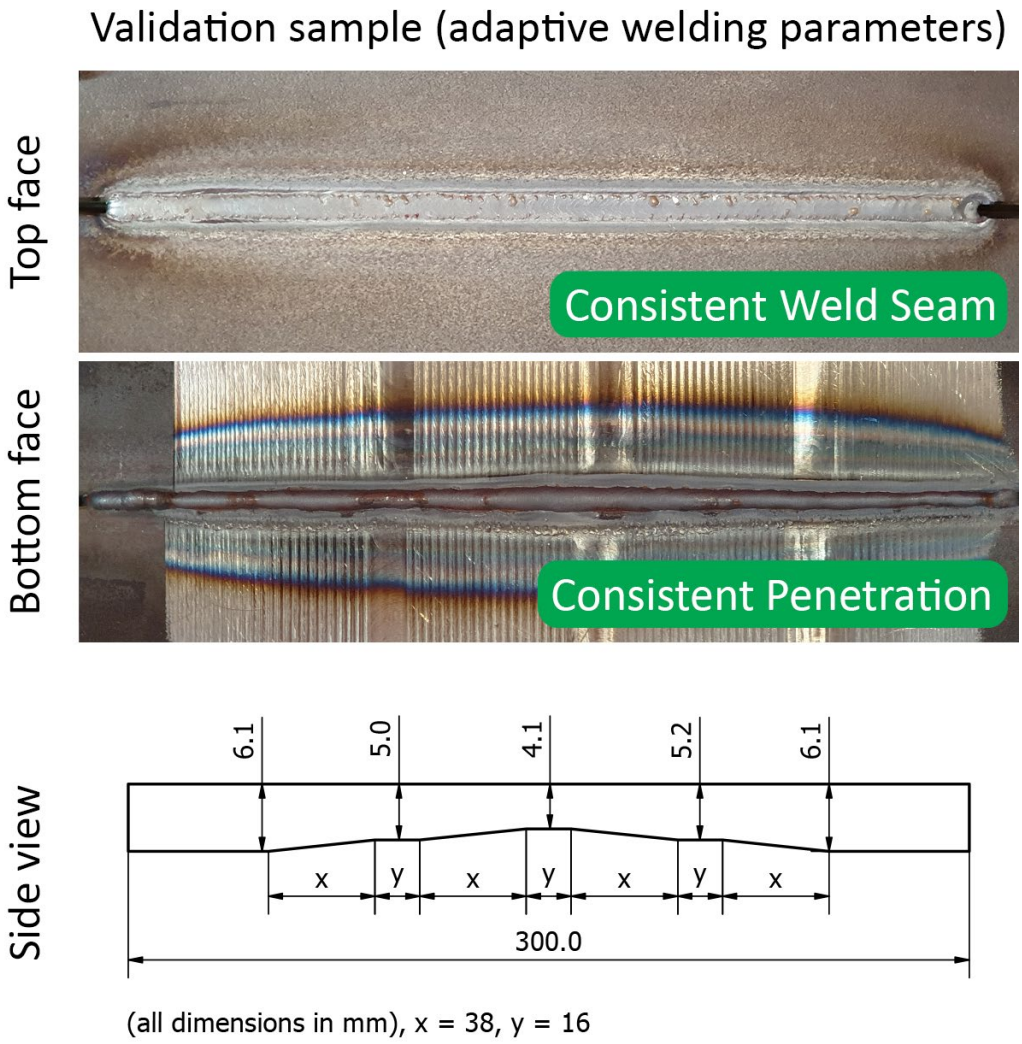

Figure 4.14. Validation sample manufactured with adaptive welding parameters based on ultrasonically measured sample thickness and the herein developed welding parameter relationships.

The significance of the obtained results became evident when the data log from the validation sample was inspected. The measured thickness, arc current, torch travel speed and wire feed rate values are plotted in Figure 4.15, Figure 4.16, Figure 4.17 and Figure 4.18, respectively. For this sample, the arc energy was automatically adjusted on-the-fly between 0.8 kJ/mm and 1.2 kJ/mm, equating to a total of 33.3 % reduction in welding power between the thickest and thinnest section of the sample. The highest thickness measured by the ultrasonic wheel probe was 6.06 mm, corresponding to an arc current of 203.6 A, welding torch travel speed of 172 mm/min and wire feed rate if 3832 mm/min. The lowest thickness measured was 4.12 mm at the thinnest middle section of the weld seam, with subsequently calculated arc current of 128.6 A, torch travel speed of 120.3 mm/min and wire feed rate of 1822 mm/min.

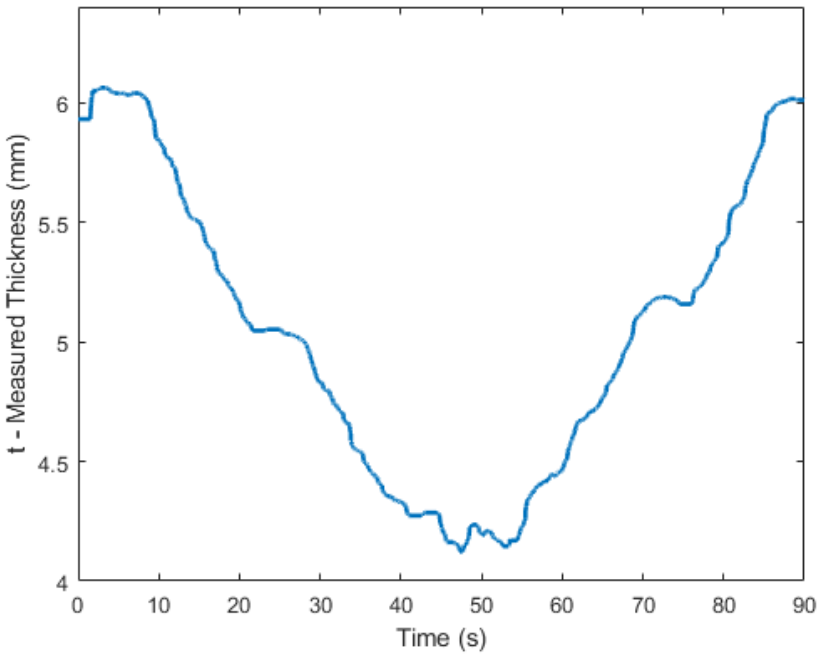

Figure 4.15 On-line thickness measurement of validation sample.

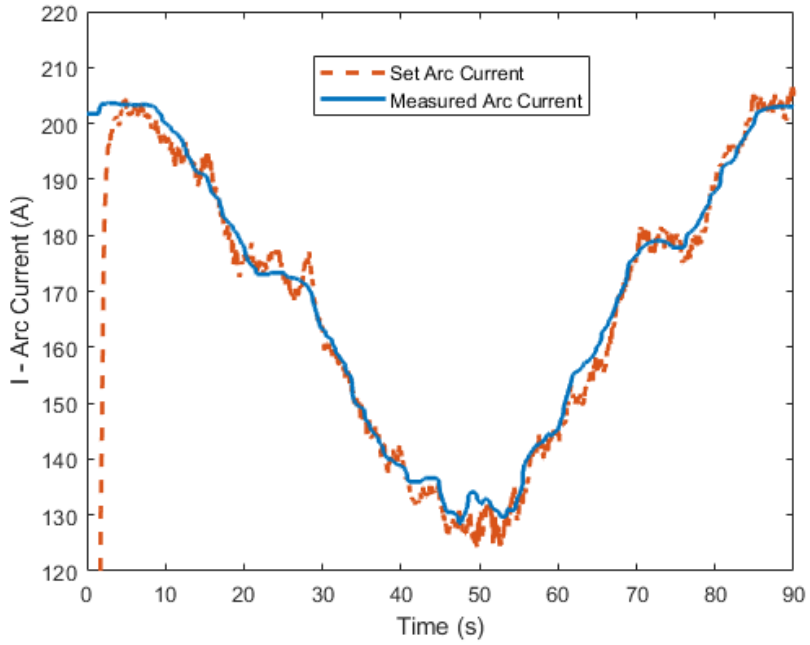

Figure 4.16 On-the-fly adjusted arc current (dashed) and measured arc current (solid) for validation sample.

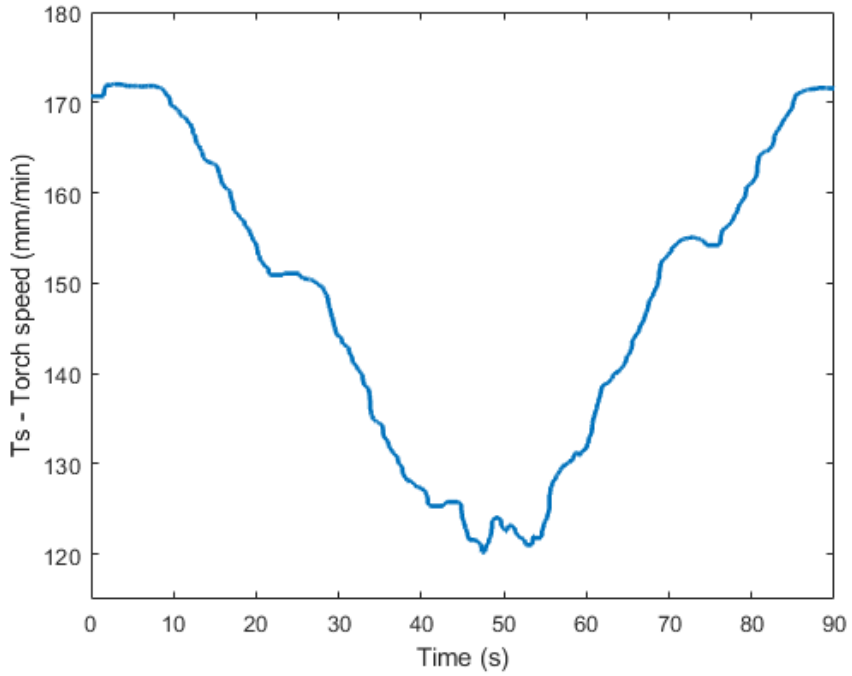

Figure 4.17 On-the-fly adjusted welding torch travel speed for validation sample.

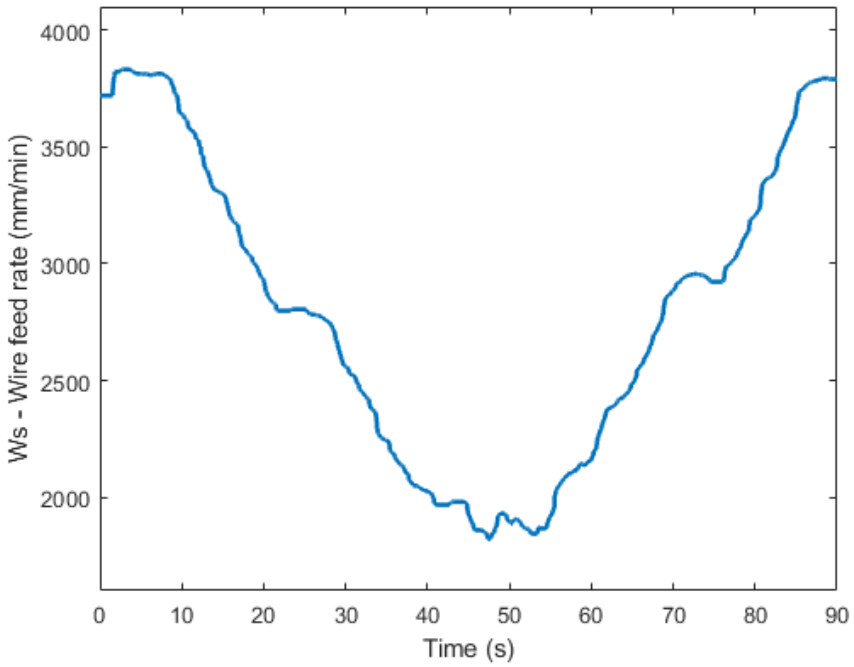

Figure 4.18 On-the-fly adjusted filler wire feed rate for validation sample.

The results of the welding trials demonstrated that ultrasonic thickness measurement was fit for on-line welding parameter adjustment. The measurement accuracy given the harsh industrial environment, i.e. deployment during welding deposition, was sufficient and the control speed of the welding power source did not introduce any noticeable latency into the system. Furthermore, the developed method significantly outperformed current open-loop automated welding deposition, when considering parts with loss of wall thickness.

4.4. Conclusion

The work outlined in this chapter has described the design and testing of a sensor-enabled automated GTAW welding system, employing an in-process ultrasonic thickness measurement and feed-forward welding parameter control of arc current, torch travel speed and wire feed. A number of significant contributions have been outlined:

Firstly, a novel sensing approach employing a robotically deployed ultrasonic wheel probe was described. The designed and manufacture custom 6 DoF mount attaching the wheel probe to the robotic end-effector allowed for the wheel probe to be positioned freely around the welding torch. Real-time signal processing was implemented to enable suppression of environmental noise emitted by the welding power source and manipulator robot, enabling a robust on-line ultrasonic measurement of the workpiece.

Secondly, an ultrasonic thickness measurement algorithm was introduced that could accommodate variations in the distortions of the tyre of the wheel probe and in the sample surface to provide accurate estimations of thickness in real time.

Thirdly a parametric relationship between sample thickness and arc current, welding torch travel speed and filler wire feed rate for butt-welding S275 mild steel plates of thickness between 4 mm and 6 mm using the demonstrator system was established and verified.

It was demonstrated that the closed-loop feed-forward control of arc current, torch travel speed and wire feed rate can maintain a consistent weld seam and uniform penetration on variable thickness steel samples. Furthermore, the developed approach can accommodate for changes in sample thickness, which under normal open-loop circumstances would lead to sample burn-through and excessive penetration. Therefore, the developed control approach lead to an improvement in terms of final product quality and integrity.

Chapter 5

Non-contact In-process Screening of Thin Welded Joints

5.1. Introduction

Safety critical welds in thin sheet metals are used in sectors where space and light-weighting are essential, such as in aircraft ducting, low-pressure boilers, pipework and nuclear storage cannisters. There exists demand for a fast, in-process inspection that provides screening of manufactured components to notify operators and process control systems of the presence of flaw indications. Due to the nature of these inline manufacturing systems, the accuracy of the measured potential flaw is deemed not as important as the rapid in-process screening and detection.

Previous attempts have been made to incorporate NDE and other welding measurement and screening approaches to improve the resultant joints and process control. A system for inspecting partially filled welds using Electromagnetic Acoustic Transducers (EMATs) inducing ultrasonic surface waves was introduced in [94], and in [95] authors use EMAT generated guided waves to inspect tailor welded blanks. However, although in both [94]

and [95] a non-contact UT method was implemented, this was only shown to work off-line, after the welding deposition and passes were fully complete, and was not demonstrated to measure on-line during weld deposition.

As a crucial parameter for the integrity of a joint, the Weld Penetration Depth (WPD) and its measurement is of particular interest to researchers. Attempts have been made in measuring the WPD through visual [96]–[98] and auditory [99] sensors, however such approaches can only provide an indirect measurement through outer weld appearance or sound. In [100] researchers utilised a Laser Ultrasonic (LU) system to generate Lamb Waves in thin plate welds. WPD was measured using transmission coefficients of the multimodal ultrasonic signal and an artificial neural network. Ultrasonic testing was performed on multiple samples with variations of WPD and the neural network was able to accurately predict the WPD. Due to the complexity of the system all signals were acquired offline, after welding, and were stored in memory before being post-processed. A similar system was demonstrated in [101], where authors employed time-of-flight measurement of bottom surface-guided Rayleigh waves for WPD measurement. The system was tested in-process during the weld deposition and it was concluded that an accurate measurement could only be performed once the plates have sufficiently cooled down, as the lower speed of sound at elevated temperatures lead to a measurement error. Furthermore, as Rayleigh waves are bound to the surface of the medium, this approach was not sensitive to any internal weld flaws.

This chapter introduces a novel non-contact gas-coupled ultrasonic method deployed in-process during weld deposition, for screening of weld penetration directly at the point of manufacture. Two non-contact air-coupled ultrasonic transducers were utilised in a pitch catch arrangement to inspect the weld between two thin mild steel plates (3 mm) using Lamb waves. The transducers were coupled to application-optimized low-noise electronics and frequency matched hardware filters to achieve sufficient SNR. A total of seven butt-weld joints different levels of WPD were created in order to test the capabilities and performance of the proposed approach. The method presented herein is suitable for in-process inspection of other metals such as stainless steel and aluminium and could be deployed within different welding processes such as GMAW, PAW and SAW.

5.2. Non-contact UT

Given the outlined challenges of in-process weld inspection, outlined in Chapter 2, non-contact ultrasonic testing proves to be favourable. LU systems generate soundwaves through the impact of photons on the test surface using pulsed laser beams and can be used to detect defects and measure the WPD in thin metal sheets [100]–[102]. However, such high power laser systems are currently far more expensive than conventional UT systems and are cumbersome to implement, due to the beam enclosures and other health and safety measures that are required to be in place [103]. Non-contact gas-coupled UT on the other hand is rather inexpensive to implement, using air as the coupling medium between the transducer and test piece to transmit the sound waves.

There is, of course, a distinct disadvantage to such a concept, as due to the acoustic impedance mismatch, air is not as efficient at transmitting acoustic energy as liquid couplants. The result is an expected 140 dB reduction in signal amplitude, when comparing air-coupled to traditional contact based UT methods [48]. Air-coupled UT was previously shown to successfully detect coarse burn-through defects arising from the GTAW process [104]. However, the magnetic interference from the welding process constrained the inspection to take place off-line, after the welding deposition. In [105] researchers attempted air-coupled UT during the GTAW process, as well as deploying acoustic emission sensors in an attempt to monitor the weld quality. The study utilised a contact based transmitter to achieve satisfactory transduction and Signal-to-Noise Ratio (SNR) when the welding arc was initiated and present. The experiments were focused on an autogenous bead on single plate configuration with no actual joining of components.

5.2.1. Gas-coupled Ultrasonic Lamb Waves

Ultrasonic waves can be guided by the sample geometry, with Rayleigh waves following the surface of the component, while Lamb waves can vibrate the full volume of plate-like samples with a thickness in order of a few wavelengths [106]. Guided waves have been used since the 1980s to inspect composite structures [107], [108] and are currently also employed in Structural Health Monitoring (SHM) and NDE for oil and gas pipelines [109], [110], railway tracks [111] and remote structural inspection platforms [16]. Lamb waves are a type of guided ultrasonic plate waves which are made up of longitudinal and transverse waves, and can detect discontinuities and flaws inside the material under test. As transverse waves can only propagate in solid media, Lamb waves can also only

propagate through solids. Their nature is such that encountering a flaw in the specimen would result in reflection and scattering, reducing the amplitude of the signal propagating across to the receiving transducer. Therefore, by monitoring the amplitude of the received Lamb waves it is possible to detect any potential flaws in the test specimen. Figure 5.1 demonstrates how Lamb waves can be induced in thin plates through the angled incidence of a longitudinal wave with the surface of the sample. The proposed inspection approach could be used in-process as a screening tool to aid process control and thus provide an early indication the welded joint quality and integrity.

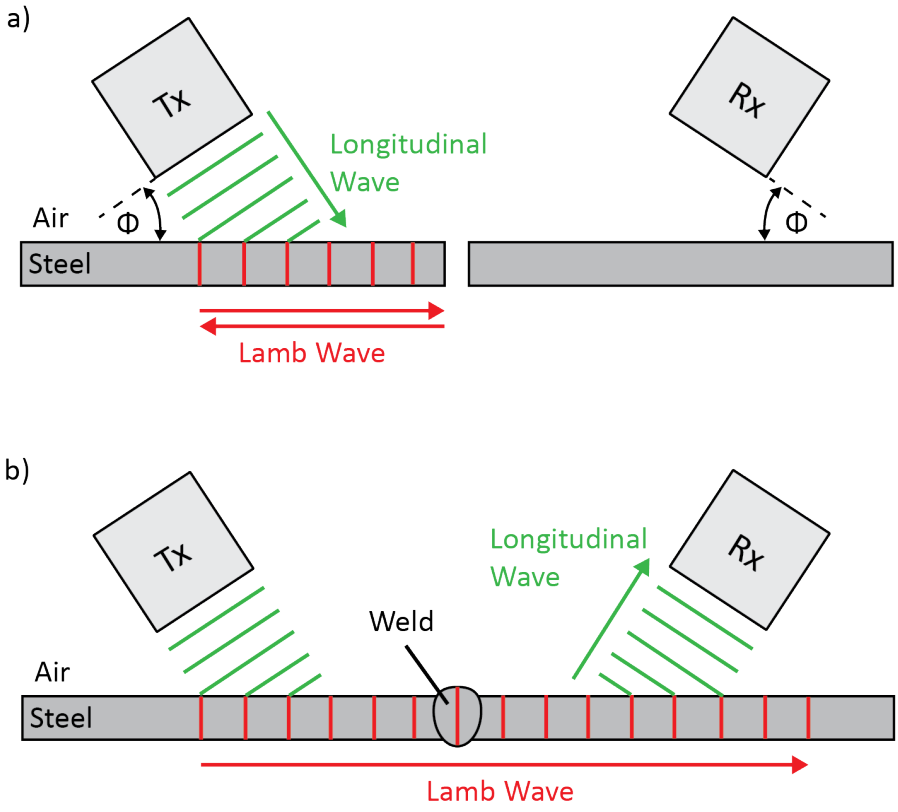

Figure 5.1 Side view schematic of a non-contact air-coupled ultrasonic inspection of thin plates using guided Lamb waves. a) Prior to welding the plates, the Lamb waves are internally reflected at the plate boundary; b) after welding the ultrasonic Lamb waves propagate through the welded joint and are transmitted to the receiving transducer.

Dispersion curves provide the phase velocity of the possible guided wave modes that can be excited in a material as a function of the Frequency-Thickness Product (FTP). The FTP, as the name suggests, is equal to the ultrasonic frequency multiplied by the thickness of the plate under test. The zeroth order antisymmetric guided Lamb wave mode (A_0) was selected, as it has a linear phase velocity at the FTP specified by the transducer frequency and sample thickness. A sample thickness of 3 mm was selected as a compromise between the range of materials that are welded in industry and the suitability for Lamb wave generation. Furthermore, the A_0 Lamb wave mode is suitable for generation by angled air-coupled transducers due to the substantial amount of out-of-plane displacement [112]. To do so, the air-coupled transducers have to be accurately set at an angle of incidence calculated using the phase velocity of the guided wave and the velocity of the incident wave in air (5.1) [48].

$$sin\,(\Phi) = \frac{V_i}{V} \tag{5.1}$$

Where Φ = Angle of incidence (°), Vi = Phase velocity of induced Lamb wave mode (m/s) and V = Velocity of incident ultrasonic wave in air (m/s). Figure 5.2 shows the phase velocity of the A_0 mode in S275 mild steel as a function of the frequency-thickness product for a range of temperatures between 17 °C and 1200 °C, a suitable range of temperatures being encountered in fusion welding applications. The curves were calculated via Disperse [113] using experimentally acquired measurements of the velocity of sound in S275 mild steel at the different temperatures [114]. The results demonstrate that an increase in

temperature of the workpiece at the point of ultrasonic wave incidence would lead to a reduction of the propagation velocity of sound in the material and hence the optimal angle of incidence would be modified. Therefore, when considering both the elevated temperature at the weld interface and gradient present across the workpieces during weld deposition, the transducers should be placed a sufficient distance away from the weld interface in order to minimise the negative effects of incidence angle misalignment due to temperature.

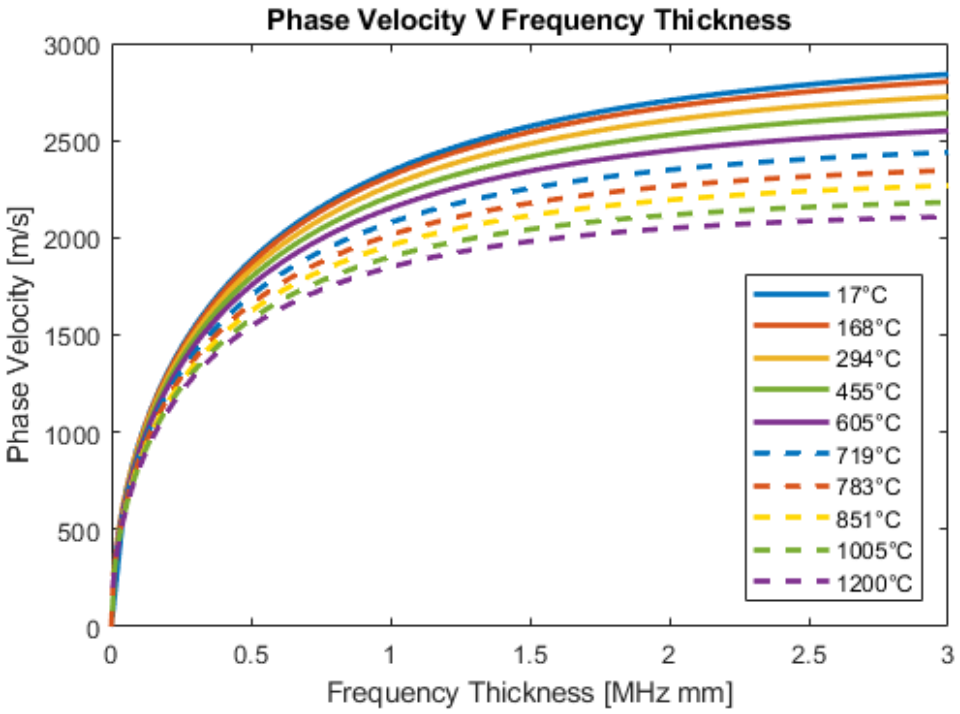

Figure 5.2 Zeroth order antisymmetric Lamb wave dispersion curves for S275 mild steel. Different lines represent the A_0 curve in the temperature range 17°C to 1200°C.

5.3. Experimental Method

5.3.1. Air-coupled Ultrasonic Transducers

Two ultrasonic non-contact 1-3 piezocomposite transducers with a 30x30 mm element size and frequency matched to a 500 kHz centre frequency were further optimised from [115] and [116] and manufactured for in-process NDE. To maximise the amount of energy transmitted into the gas coupling medium, the transducers were fitted with a custom matching layer as shown in Figure 5.3. Such a matching layer was necessary in order to compensate for the high mechanical impedance mismatch between the piezoelectric transducer and air [116]. The two components of the matching layer were silicone rubber (SR) [117] and a 0.12 mm thick nylon microporous membrane filter (MF). The SR was applied on the MF through an RK K202 Control Coater machine to obtain a consistent layer structure with a final matching layer thickness of 0.5 mm. A transition layer of modified silicone rubber (MSR) and a layer of membrane filter saturated with the silicone rubber (SF) were formed between the SR and MF as a result of the manufacturing process. The SR side of the matching layer structure was directly bonded to the transducer face leaving the MF side to interface with air as shown in Figure 5.3. The resulting matching layer approach, when applied to both transmitting and receiving transducers, accounted for a 35 dB improvement in signal amplitude, compared to an unmatched pair of transducers.

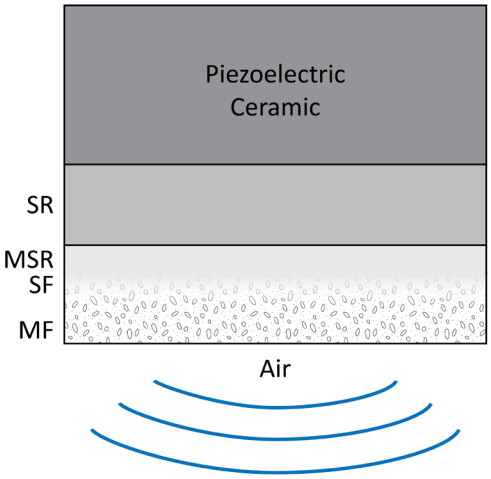

Figure 5.3 Air-coupled ultrasonic transducer with applied matching layer, increasing the mechanical coupling between the piezoelectric element and air.

5.3.2. Ultrasonic Method

The two transducers were laterally positioned on either side of the weld seam in a pitch-catch arrangement as per Figure 5.1. To minimise the negative effects of workpiece temperature gradient on the incidence angle, the transducers were positioned at a distance of 150 mm from the weld seam and the set-up was initially optimised for the material at room temperature. The plate thickness and transducer frequency used in the experiment provided an FTP of 1.5 MHz.mm, which according to the calculated dispersion curves in Figure 5.2. corresponds to an A_0 phase velocity of 2560 m/s at room temperature. The angle of incidence was then calculated to be 7.7° by substituting the phase velocity and velocity of sound in air (344 m/s) in (5.1). 3D printed plastic wedges were created to accurately achieve this angle in practice. The wedges were placed under the transducers only to fix the angle, and were removed before any welding was carried out. The

transducers were not exposed to any high temperatures, due to their distance from the weld seam and the air gap (above 4 mm) insulating them from the workpiece.

Apart from the importance of the matching layers, the transmitter and receiver resonance frequencies, and hence excitation frequency, must also be carefully designed, especially when operating in a pitch-catch configuration [118]. In particular, the electrical resonance frequency f_e of the transmitter, i.e. the frequency at which the electrical impedance is minimum, should be equal to the mechanical resonance frequency f_m of the receiver, i.e. the frequency at which the receiver will naturally resonate from an incident acoustic wave [119], [120]. Due to the differences between the as-built and theoretical transducers, the exact excitation frequency was chosen experimentally, by placing the transducers facing each other for a pitch-catch transmission through air and adjusting the frequency until a maximum amplitude was recorded at the receiving transducer.

The transmitting transducer was excited through a 520 kHz 10 cycle tone burst at a PRF of 200 Hz with an amplitude of 170 V (Figure 5.4, dashed line). An A_0 wave was excited in one plate with a travel direction perpendicular to the weld interface. The acquisition gate was set so that it only captured the Lamb wave transmitted through the material and did not include the direct pressure wave transmitted through air, as due to the large difference in the speed of sound in steel and air, the two waves had different times of arrival at the receiver.

The dominating factor that contributed to signal attenuation between the transmitter and receiver was the acoustic impedance mismatch and resulting reflection of the signal when

it reached and passed through the boundary between two media with different densities. Therefore, as the two plates were separated by a 3 mm air gap prior to welding, the ultrasonic signal was reduced to only negligibly small values and orders of magnitude below the sensitivity of the receiver transducer, and hence, no guided waves could be detected. Upon deposition and solidification of the weld joint, however, the induced Lamb waves propagated through any subsequently welded joint and were received by the positionally aligned receiving transducer. After reception by the receiver, the signal was fed through two cascaded pre-amplifiers with sensor-matched hardware bandpass filters (manufactured by McWade Associates Ltd), giving a total gain of 80 dB. The received signal amplitude measured at the amplifier output when testing a reference plate of the same material and thickness was 200 μV (Figure 5.4, dotted line) or 119 dB lower than the excitation voltage. Therefore the total amplitude loss between the transmitter and receiver was around 199 dB. Moreover, the received waveform significantly differs from the excitation waveform due to the dispersive nature of Lamb waves and the post-transduction temporal ringdown, introduced by the lightly damped nature of the transducers. Lastly, the signal was digitised by the PEAK LTPA ultrasonic driver and acquisition system [72], at a 25 MHz sampling rate, using 128 averages and an additional hardware gain of 16 dB. The averaging used by the acquisition system was cumulative, meaning that it returned one A-scan for every 128 acquired samples, hence, with the above configuration, one sample was recorded every 0.64 seconds.

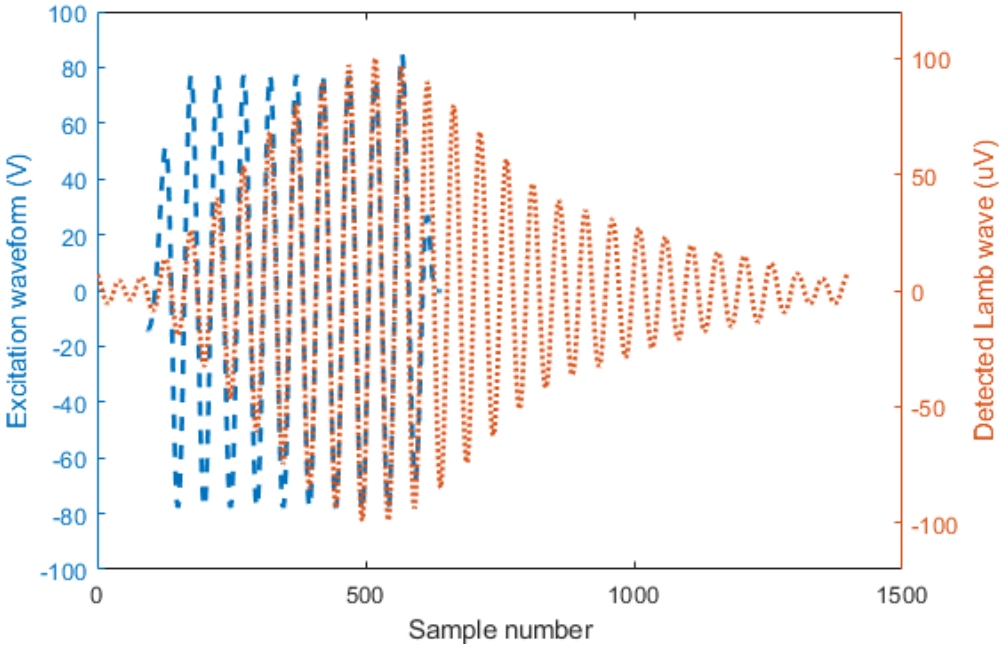

Figure 5.4 Excitation waveform, comprising a 10 cycle 520 kHz tone burst with a peak-to-peak amplitude of 170V (dashed line) and detected Lamb wave(dotted line). The received Lamb wave had a peak-to-peak amplitude of 200 µV after 80 dB of hardware pre-amplification.

5.3.3. Experimental Procedure

The flexible welding cell described in Chapter 3 was utilised for the experimental trials. To measure the temperature gradient across the samples, three thermocouples were tack welded along the ultrasonic wave path at a distance of 20 mm, 60 mm and 100 mm away from the weld seam respectively as shown in Figure 5.5. The thermocouples were positioned on one side of the weld only, making use of the symmetry of the workpiece and were found to have no measurable effect on the propagation of the guided waves. The ultrasonic A-scans were recorded and encoded using the positional information of the manipulator-held welding torch.

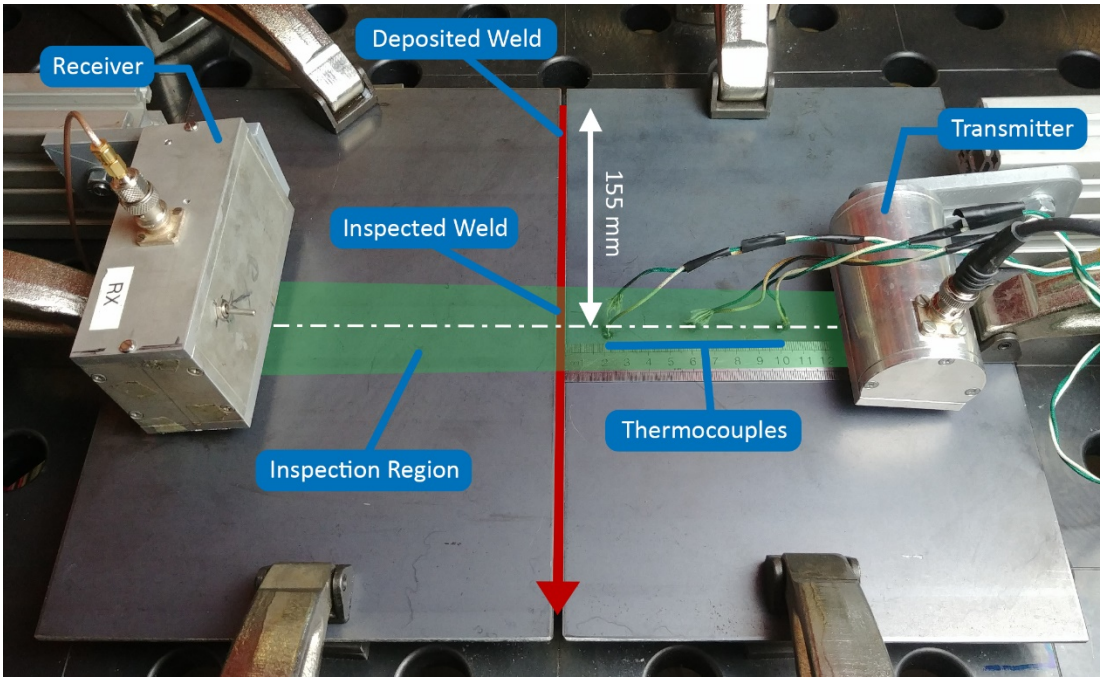

Figure 5.5 In-process non-contact ultrasonic inspection set-up; the transmitting and receiving transducers are located on either side of the weld interface with the inspection region shown between the dashed lines.

A 290 mm butt weld was deposited between two 200 mm x 300 mm x 3 mm S275 steel plates along their long side using a weaving torch motion. The two plates were separated by a 3 mm gap, which was experimentally selected in order to maintain a constant gap between the plates during welding, based on the clamping force, clamp arrangement and the fact that no tack welding was performed prior to welding. The starting point of the deposited weld was located at an approximate distance of 155 mm from the centre of the inspection region between the two transducers, as annotated in Figure 5.5. This distance was maintained constant for all samples, as the position of the robotically delivered welding torch was calibrated with respect to the welding table, and the transducer position was fixed to the welding table. Although the element size of the transducers used was 30 mm, the inspection region was wider due to beam spread. Through Finite Element

Analysis (FEA) simulation, it has been calculated that for air-coupled transducers with the same element size, located at a similar distance from the inspection point, the width of the generated Lamb wave beam would be approximately 50 mm [121], [122]. Therefore, the length of the inspected weld section was around 50 mm.

5.3.4. Welding Trials

A concept validation study was conducted with a total of 7 samples, marked S1-S7. The samples were welded with varying levels of arc energy from 0.59 kJ/mm to 1.03 kJ/mm. The arc energy was adjusted between the samples in order to obtain welds with different WPDs. A travel speed of 80 mm/min was selected as suitable for the sample thickness and was maintained constant between the different trials. Appropriate wire feed rates were selected so that a stable weld pool could be developed in each sample and the two plates could be connected with a weld bead. Values of arc energy under 0.59 kJ/mm were found to be too low to create a stable weld pool and values above 1.03 kJ/mm were found to result in weld burnthrough. Continuous in-process ultrasonic testing was performed during the manufacture of all samples, as shown by the video frames in Figure 5.6**.**

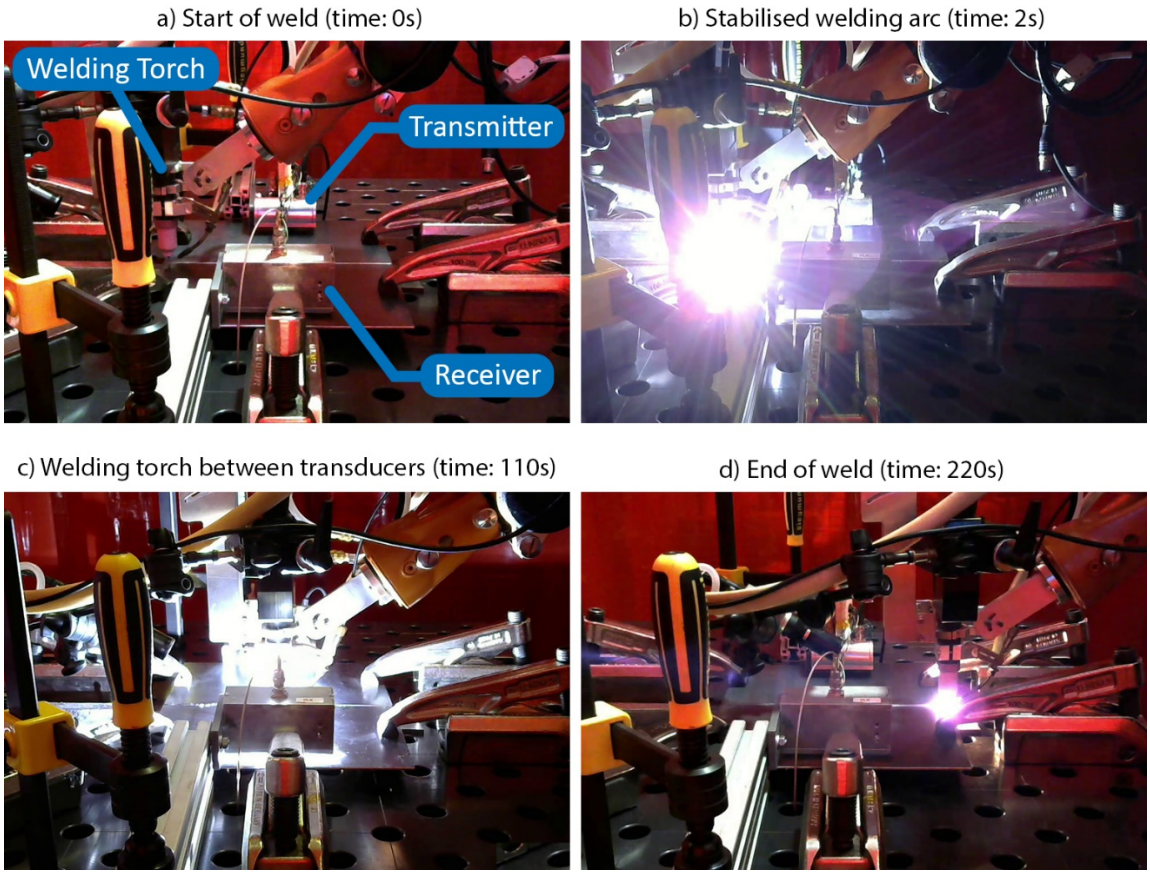

Figure 5.6 Video frame stills from welding trials with in-process non-contact ultrasonic screening.

5.3.5. Destructive Testing

Tensile specimen sections were waterjet cut from the weld seam in the inspection region directly between the two transducers and were put under tensile stress until failure. A second section measuring 40 mm x 20 mm was similarly cut from each sample for weld macrography and visual inspection. A weld macrograph was performed by polishing and etching the weld sections using acid, which revealed the shape and size of the fused area. The WPD of each sample, expressed as the distance between the top surface of the base plates and the root face of the weld bead, was measured from the macrograph photographs in Figure 5.7 through a spatial calibration in the image processing software Adobe Photoshop [123]. The welding parameters and measured WPD for each sample are shown in Table 5.1

.

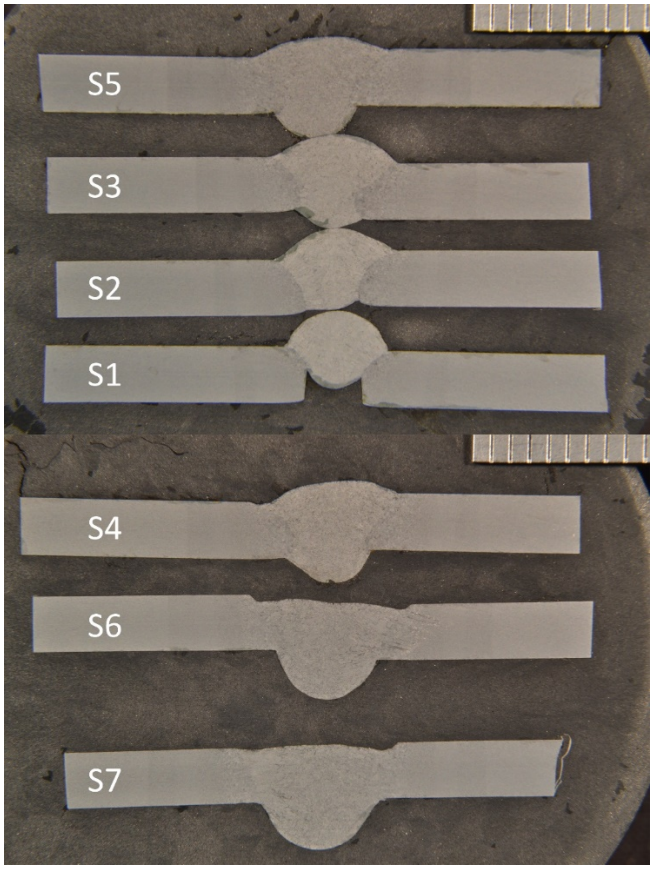

Figure 5.7 Weld macrographs of samples S1 through S7.

Table 5.1 Welding parameters and measured weld penetration depth for welding trials S1 through S7. Wire feed rates were selected so that a stable weld pool could be developed in each sample.

Sample	***Current (A)***	***Voltage (V)***	***Travel Speed (mm/min)***	***Arc Energy (kJ/mm)***	***Wire Feed Rate (mm/min)***	***WPD (mm)***
S1	66.5	12	80	0.59	1330	2.11
S2	76	12	80	0.68	1520	2.82
S3	85.5	12	80	0.77	1710	3.48
S4	90	12	80	0.81	1800	4.53
S5	95	12	80	0.86	1900	4.3
S6	104.5	12	80	0.94	2000	5.08
S7	114	12	80	1.03	2100	5.52

The macrographs revealed that samples S1 and S2 observed a lack of root penetration due to the low arc energy used. On the other hand, samples S6 and S7 suffered from undercut and lack of weld crown due to the excessive arc energy. Results from tensile stress testing to failure in Figure 5.8 confirmed that the two samples with identified incomplete WPD had a lower failure point, compared to the rest of the samples. The samples with complete and excessive WPD, however, did not show a reduction in tensile strength. Although this was true at the time of manufacturing, excessive welding power and undercut are known causes of weld cracking when the components are exposed to fatigue loading [124] and undercut is, therefore, undesirable.

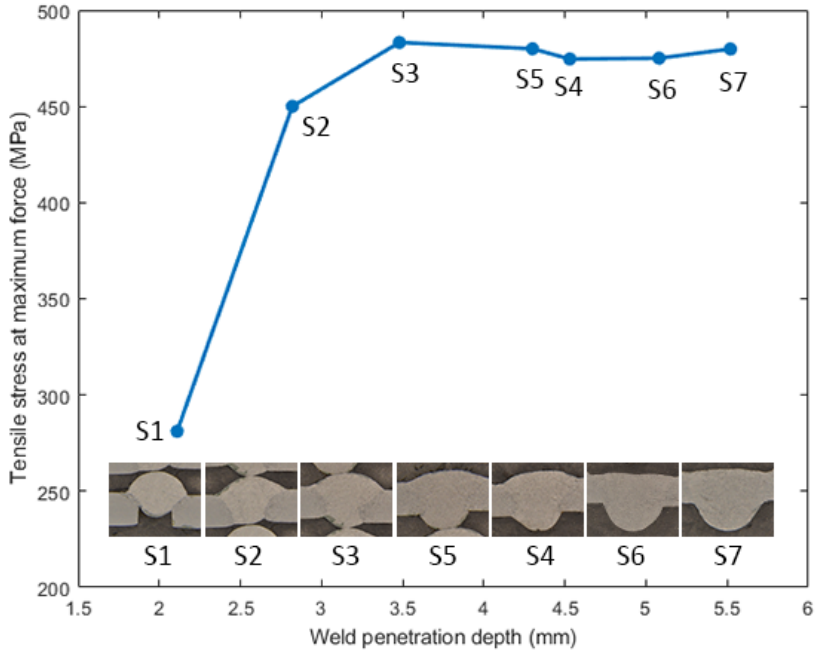

Figure 5.8 Relationship between weld penetration depth and maximum tensile stress at failure for samples S1 through S7..

5.3.6. Temperature Measurement

The thermocouple temperature measurements from samples with optimal (S5), below optimal (S2) and above optimal (S6) are shown in Figure 5.9. The temperature plots can be split into three regions, depending on the location of the welding torch, with respect to the inspection region: No weld, Welding, and Cooling. When the welding torch was inside the inspection region, a sharp temperature gradient was introduced, which started to reduce as the torch moved past the transducers and the section of the sample began to cool. Based on the temperature measured by the thermocouples located closest to the transducers, no incidence angle misalignment was expected, when the welding torch was in the inspection region.

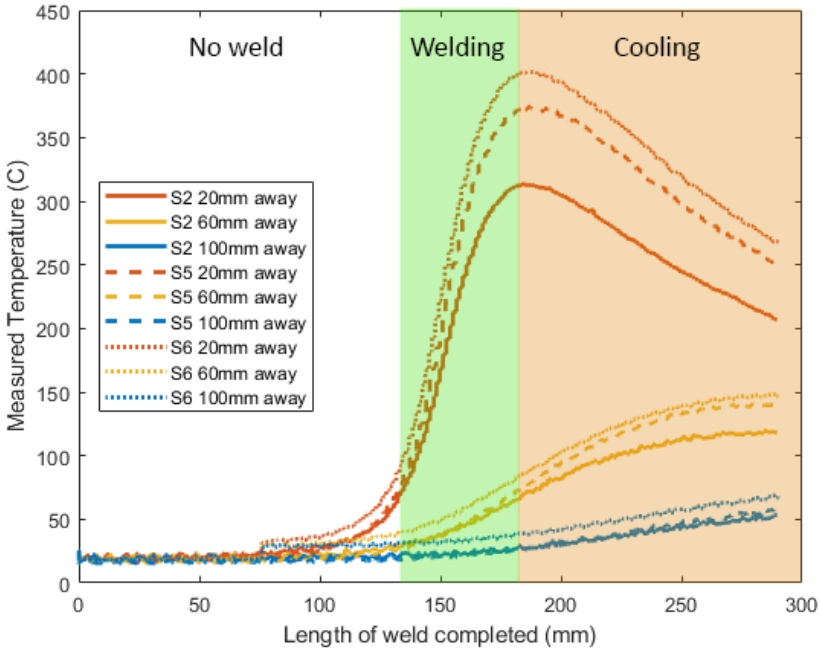

Figure 5.9 Sample temperature in the inspection region measured via thermocouples mounted at a distance of 20mm (red lines), 60mm (yellow lines) and 100mm (blue lines) for samples with below optimal (solid lines), optimal (dashed lines) and above optimal (dotted lines) arc energy.

5.4. Signal Processing

5.4.1. Frequency Domain Analysis

A spectrogram of the ultrasonic signals acquired during the manufacture of the reference sample S5 was generated by concatenating the captured A-scans in the acquisition gate and applying a Short-Time Fourier Transform (STFT). The STFT of the signal utilised a Hamming window spanning the length of one acquired A-scan (3500 samples with no overlap), evaluated at 8001 frequencies (giving a frequency resolution of 25 MHz / 8001 = 3.125 kHz) and resulting in one time bin per acquired A-scan. The spectrogram was thresholded at 0 dB to remove the noise floor present in the first half of the acquisition, where no Lamb waves could propagate to the receiving transducer. The acquired spectrogram shown in Figure 5.10 a) shows that the received signal consisted of two prevalent components – intermittent system noise emitted by the industrial robot drives at approximately 425 kHz and the received Lamb wave at the transducer frequency, appearing in the second half of the spectrogram. The system noise was removed through a bandpass filter around the frequency of the excitation signal (470 kHz and 550 kHz cut-off), as can be seen by the spectrogram of the filtered signal in Figure 5.10 b).

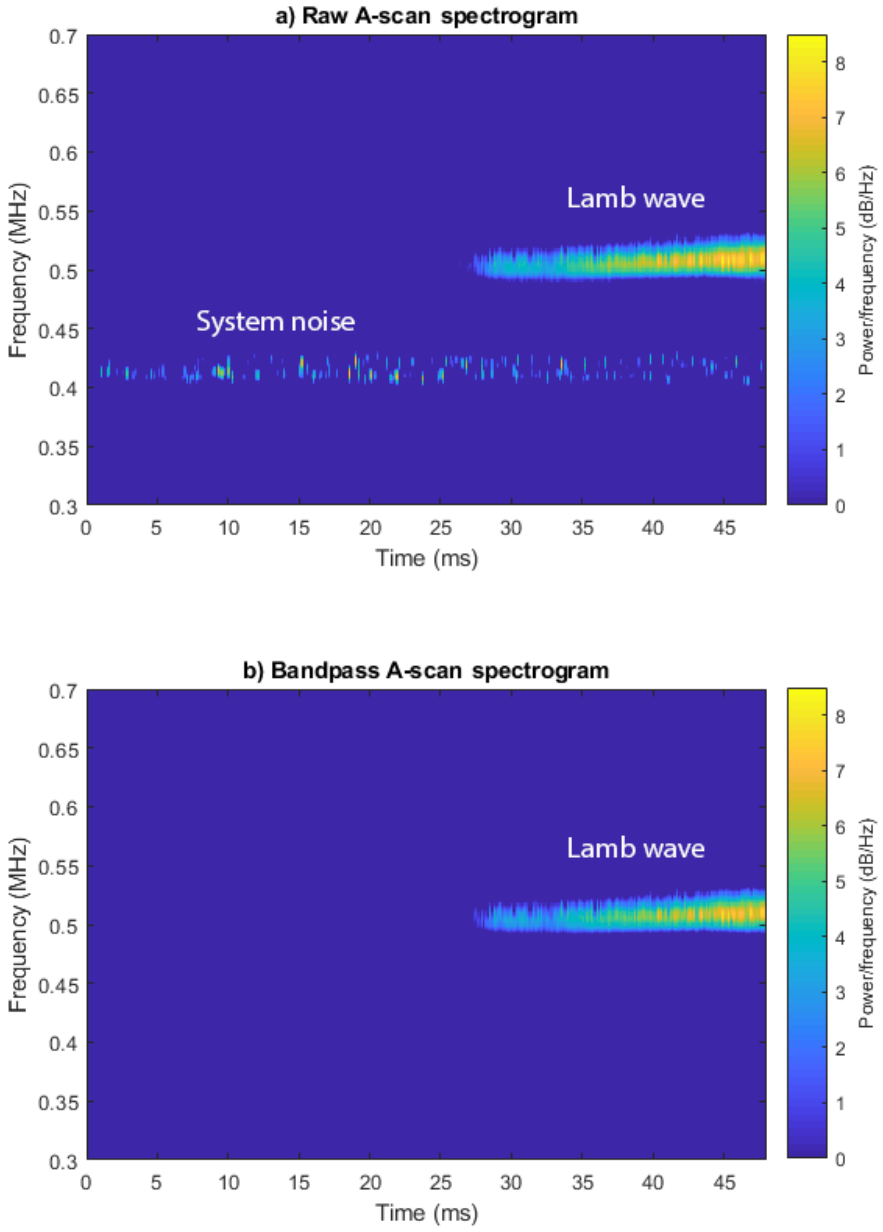

Figure 5.10 STFT spectrogram of a) raw A-scans from sample S5; b) bandpass filtered A-scans from sample S5.

The STFT also indicated that the Lamb wave experienced a frequency shift, seen by the upward trend in the spectrogram. The Discrete Fourier Transform (DFT) was calculated to measure the power of the frequency components present in the detected Lamb wave (Figure 5.11 a). Figure 5.11 b) shows that frequency with the highest magnitude shifted from around 505 kHz to 510 kHz, while Figure 5.11 c) shows that the phase of the 520 kHz component shifted with around 360 ° during the time of measurement. This phenomenon could be attributed to the temperature gradient along the propagation path of the ultrasonic signal, which reduced as the sample in the inspection region cooled down.

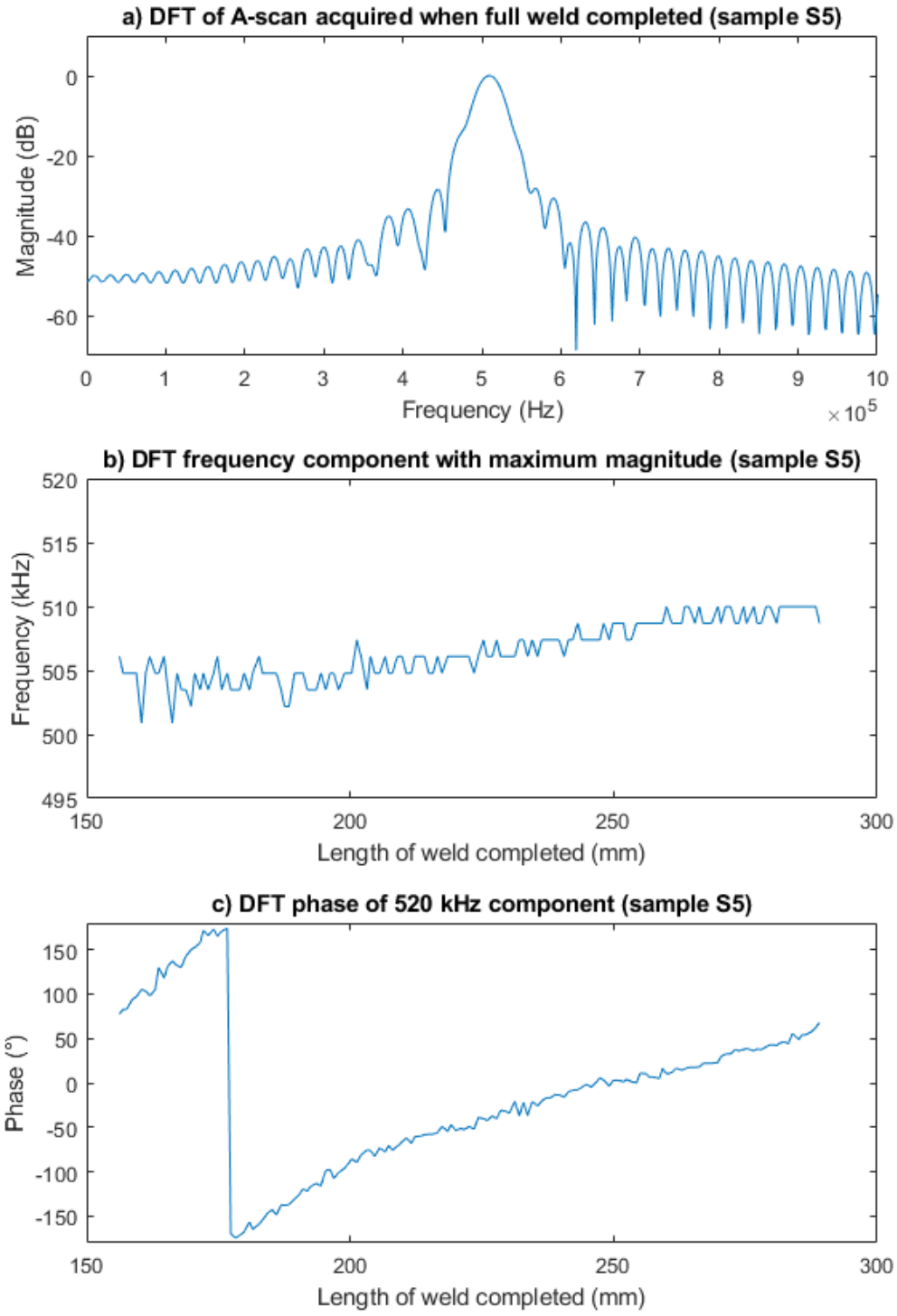

Figure 5.11 DFT analysis of acquired A-scans for sample S5.

5.4.2. Time Domain Analysis

A digital matched filter using the excitation signal waveform was applied to the detected signals to maximise the SNR. The envelope of each signal was detected and the amplitudes were normalised using a percentage scale, so that amplitude scaling could be performed. Figure 5.12 shows the waveform of the received Lamb wave at each step of the applied digital signal processing. The processing of each acquired A-scan took under 1 ms when the computation was implemented on-line in LabVIEW.

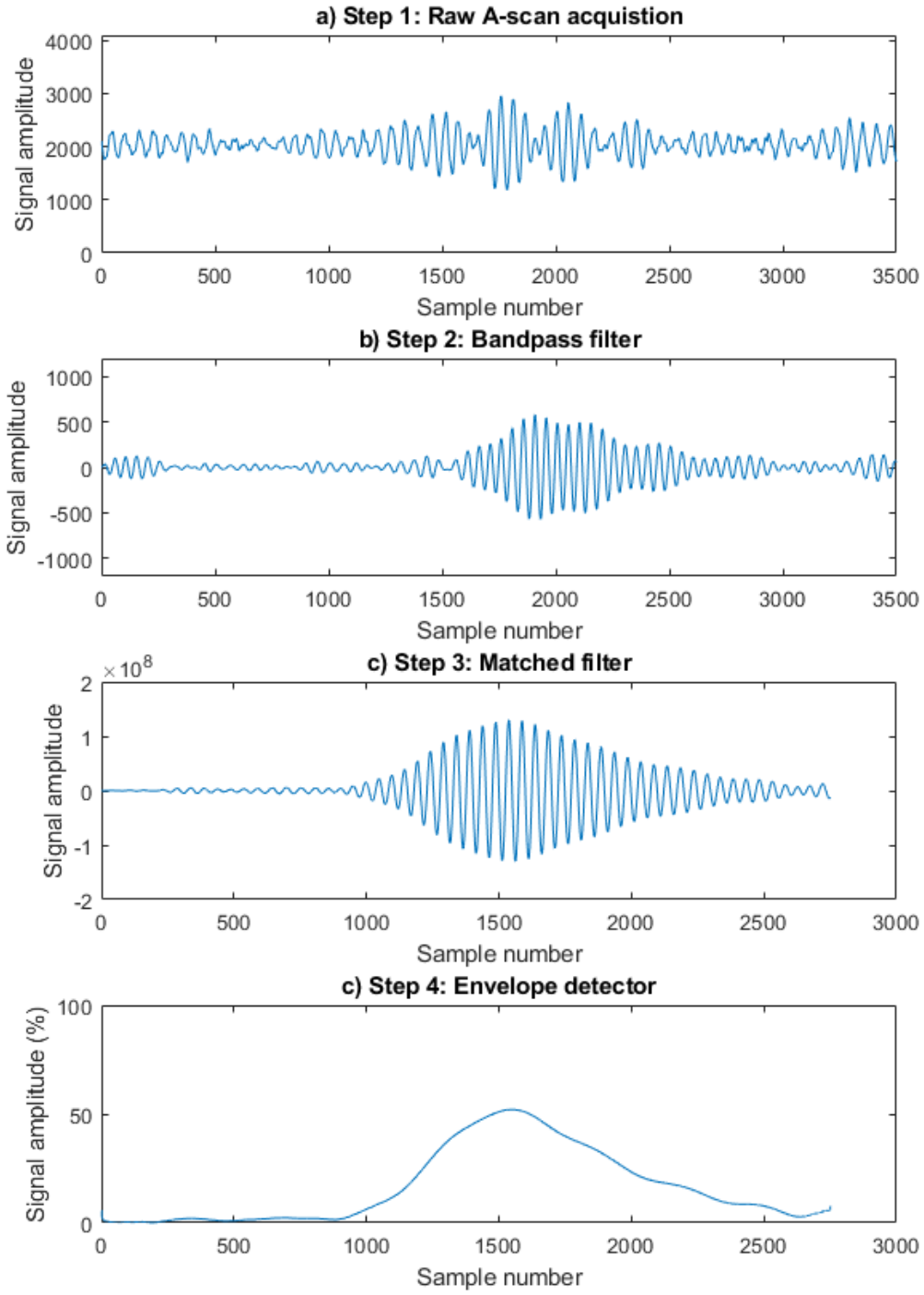

Figure 5.12 Digital signal processing steps for acquired A-scans (sample S5; A-scan number 200 out of 344, acquired when 167mm length of weld was completed)

The maximum amplitude of the processed A-scans was recorded for each position of the welding torch and the resulting trace was filtered to remove high frequency noise for analysis purposes. The obtained curves shown in Figure 5.13 can once again be separated into three regions, based on the location of the welding torch with respect to the inspection region. In region (1) only the background noise was observed at the receiver, as there was no weld present between the transducers, and no guided waves could propagate across the gap. For the samples with optimal and close to optimal arc energy, region (2) contained a Sigmoid (S-shaped) curve with an approximate length equal to the length of the inspected weld seam (50 mm). This occurred when the welding torch was in the inspection region between the transducers at the time of measurement and, therefore, corresponded to the solidification of the weld, as the Lamb waves cannot propagate through the air gap between the plates prior to this.

The turning point in the curve at the end of region (2) occurred when the full weld in the inspection region solidified. Any subsequent weld deposited outside the region of sensitivity would not affect the amplitude of the ultrasonic wave, therefore this would be the point at which amplitude sizing should be carried out. However, the Lamb wave amplitude in all samples continued to increase linearly in region (3).

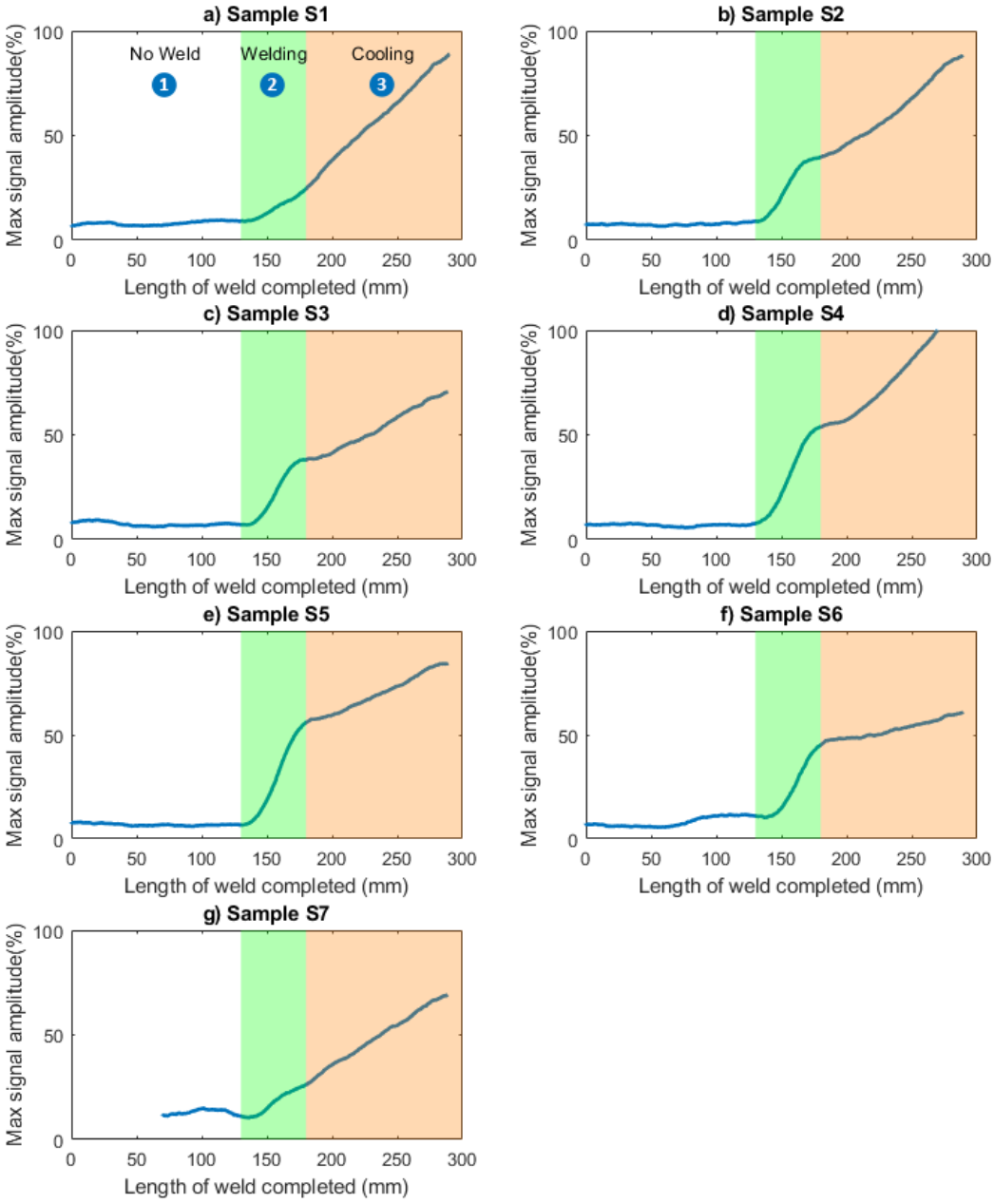

Figure 5.13 Maximum signal amplitude vs length of weld completed for samples manufactured with below optimal (S1, S2, S3 and S4), optimal (S5) and above optimal (S6 and S7) arc energy.

When plotting the maximum signal amplitude against the temperature measured by the thermocouple located closest to the weld (20 mm away), the same three regions can be identified and overlayed on the traces in Figure 5.14.

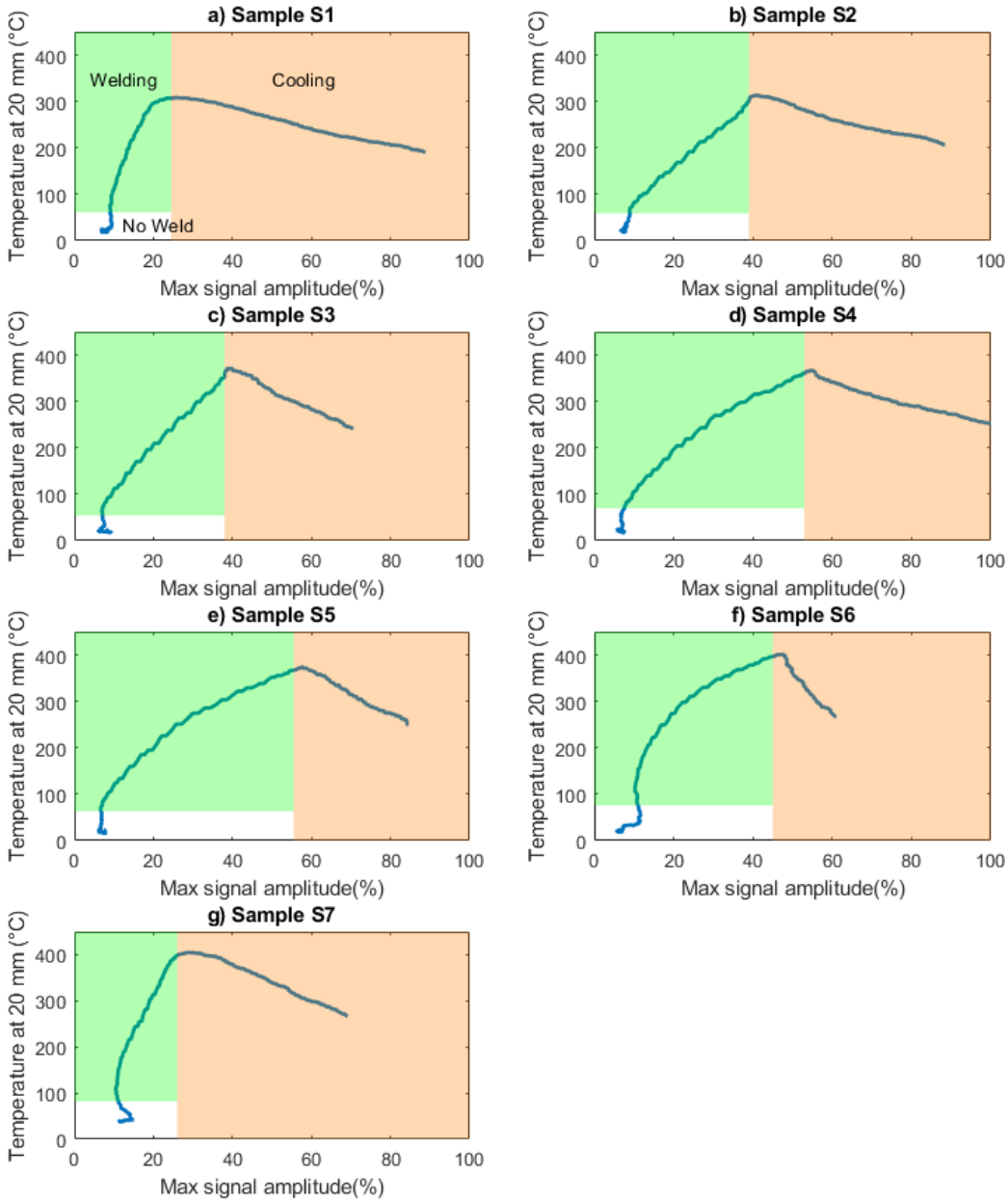

Figure 5.14 Relationship between maximum signal amplitude and sample temperature measured at a distance of 20 mm from the weld seam.

At the start of each welding trial when the welding torch was outside of the inspection region, the traces were contained in the bottom left corner of the graph, as the signal amplitude and sample temperature were both low. When the welding torch entered the

inspection region the traces started to move diagonally, as both the signal amplitude and temperature were increasing. However, when the welding torch left the inspection region, the signal amplitude continued to increase, while the temperature was decreasing. As the sample temperature was the only variable changing during this portion of the welding trials, it can be concluded that the increase in signal amplitude is caused by the decreasing sample temperature. This correlation explains the continued increase in signal amplitude after the weld in the inspection region had fully solidified.

The signal amplitude correlation with temperature and the dynamic nature of the welding process and varying input arc energy between the welding trials ruled out traditional ultrasonic signal amplitude comparisons. Instead, due to the fact that all measurements were taken in the same position, it was decided to follow the evolution of the Lamb wave amplitude and phase over time. As the Lamb waves could not propagate through the liquid weld pool, the increase in amplitude when the welding torch is in the inspection region can be directly attributed to the phase change of the weld between liquid and solid. Furthermore, as the centerline of the inspection region was located 155 mm away from the weld starting position, the highest rate of amplitude increase was expected at that location. The derivative of the Lamb wave amplitude with respect to time was calculated for each sample and is shown in Figure 5.15.

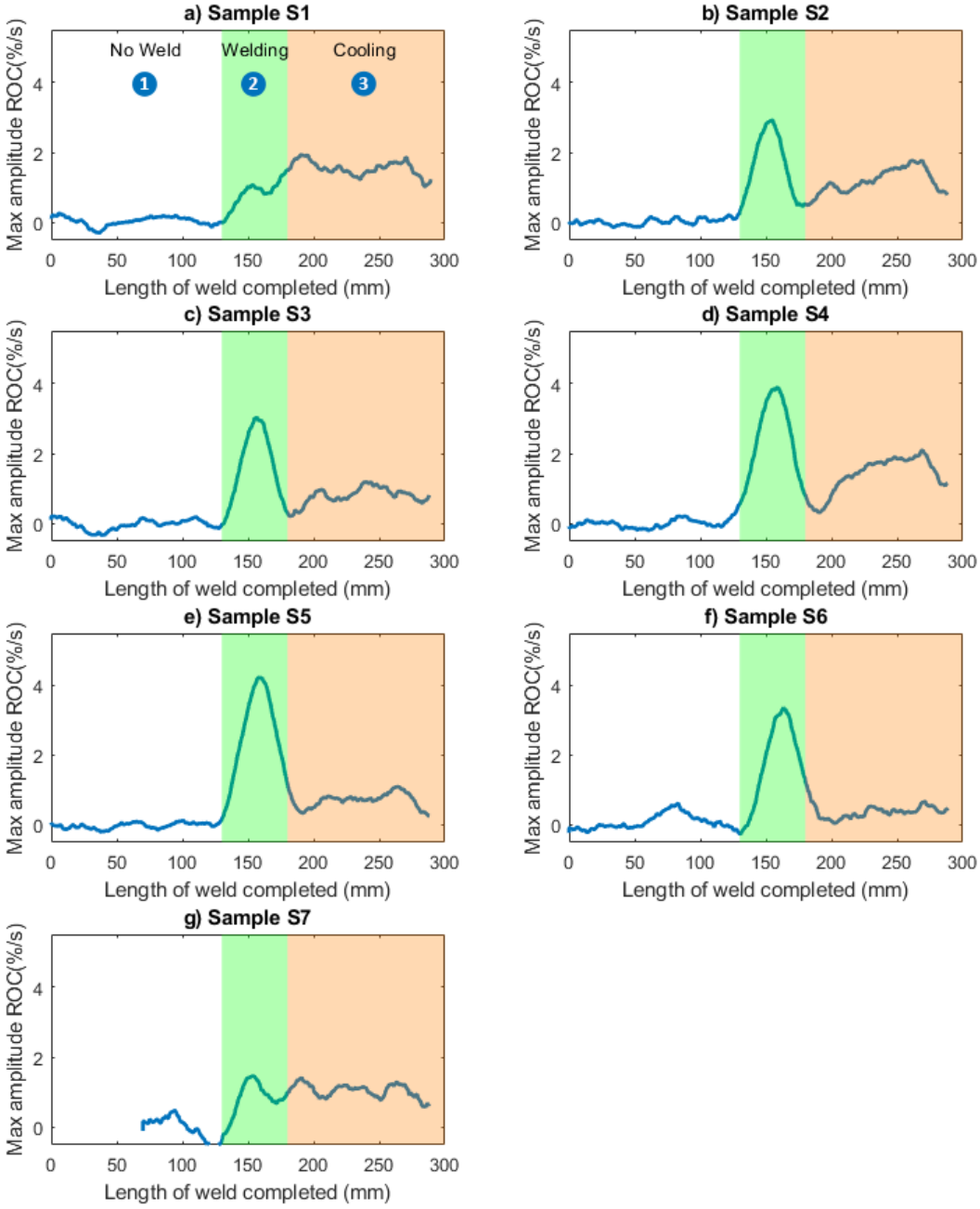

Figure 5.15 Signal amplitude Rate Of Change (RoC) vs length of weld completed for samples S1 through S7.

The location of the peak RoC was different for each trial and varied from 154 mm for the sample with the lowest heat input (S1), to 163 mm for the sample with the highest (S7). The shift of this peak from the expected location could be attributed to the delay in the weld solidification, caused by the higher amount of heat and the subsequent larger weld pool separating the welding torch and the trailing solidified weld. The maximum RoC also differed between the welding trials, with the highest peak RoC measured for the reference sample S5.

5.5. Results and Discussion

The maximum Lamb wave amplitude RoC for each sample was plotted against the obtained WPD. Each point on the plot in Figure 5.16. corresponds to an individual sample, the macrograph of which is displayed underneath. The peak Lamb wave amplitude RoC and the WPD observed a parabolic correlation, with the lack of penetration samples laying on the far-left side of the plot, and the undercut samples laying on the far right. This was due to the geometry of the welds varying from the geometry of a continuous 3 mm thick plate, resulting in the attenuation of the ultrasonic Lamb waves. As can be seen, a lack of root penetration and excessive penetration/undercut greater than 0.5 mm can be detected, when comparing the measurements to a baseline sample.

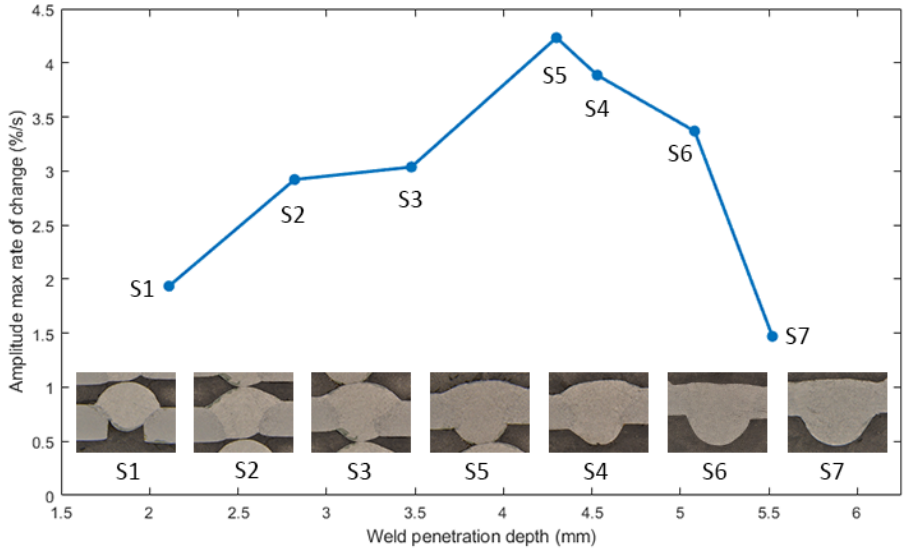

Figure 5.16 Relationship between weld penetration depth and Lamb wave amplitude peak RoC.

The location of the peak Lamb wave RoC for each sample was also measured and plotted vs the arc energy. As samples S1 and S7 were at the extreme levels of arc energy, the differential plots did not contain a clear peak when the welding torch was inside the inspection region and were, therefore, excluded from the graph. Figure 5.17 shows that the location of the peak Lamb wave RoC varied linearly with arc energy, owing to the delayed solidification of the inspected weld section. Furthermore, the total Lamb wave phase shift also varied linearly with arc energy as shown in Figure 5.18, due to the increasing heat input and thermal gradients in the sample. Therefore, as the former and latter parameters are correlated to the amount of heat generated by the welding process, they can be used in conjunction with the maximum amplitude RoC in order to distinguish between insufficient weld penetration and excessive WPD, when comparing the results to the baseline sample.

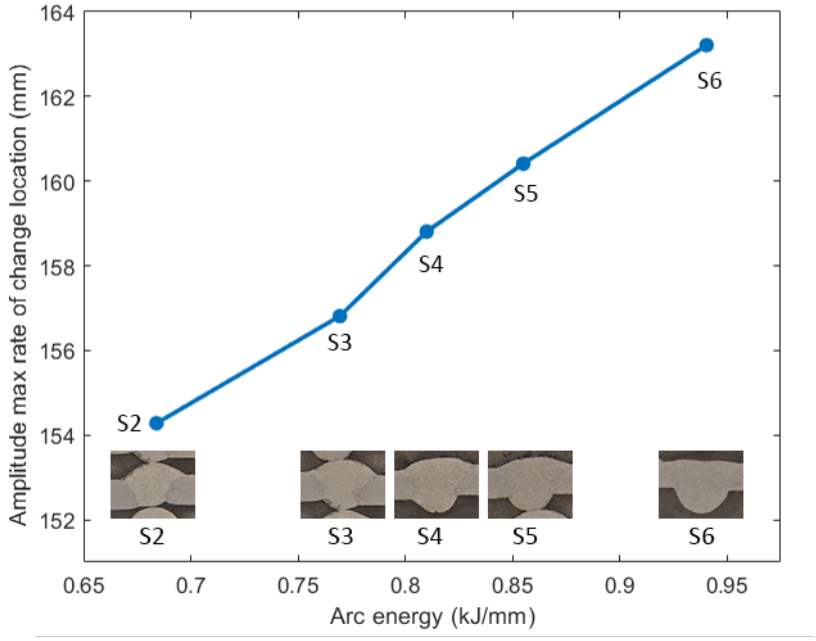

Figure 5.17 Relationship between arc energy and location of signal amplitude RoC.

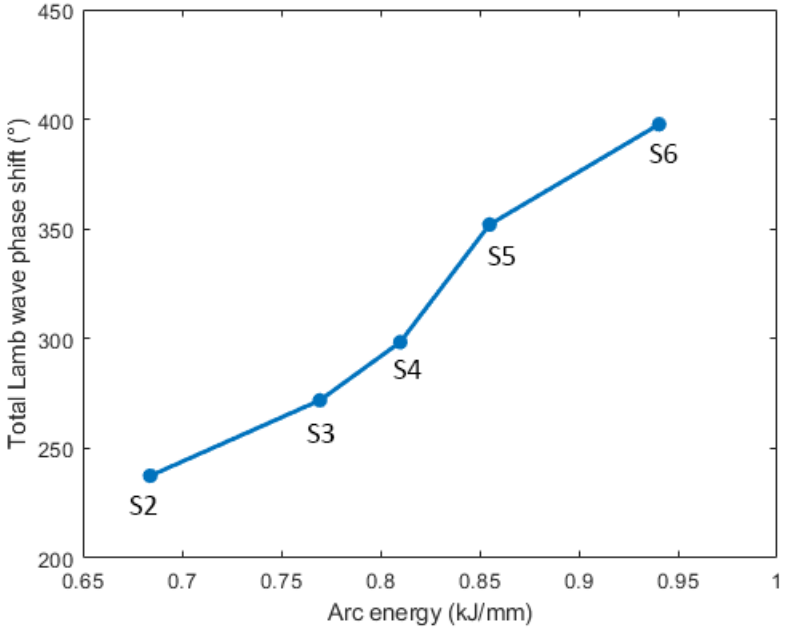

Figure 5.18 Relationship between arc energy and total Lamb wave phase shift.

The temperature of the workpiece had a strong adverse effect on the propagation of the Lamb waves due to the change in speed of sound and subsequent attenuation, frequency shift and phase shift. Nevertheless, the proposed technique was found to be sensitive to changes in the WPD in the butt-welded mild steel samples. By setting an adequate threshold for the peak Lamb wave RoC and measuring the location of this peak, the demonstrated approach can indeed be used to predict whether lack of root penetration or undercut can be expected in the produced weld. The lack of couplant required for the air-coupled ultrasonic transmission provides a non-obtrusive method for in-process screening of the welded joint. Therefore, this method could be used to provide an early indication of flaws developing in the weld and can be used in-situ for process monitoring.

5.6. Conclusion

An in-process screening procedure using air-coupled ultrasonic transducers was demonstrated and shown to enable on-line deployment in a harsh industrial environment, i.e. during GTAW welding. A successful non-contact transmission and reception of a guided Lamb wave was made possible through a matching layer system applied to the transducers, low noise amplification and real-time signal processing.

A total of seven butt-welded mild steel samples with varying levels of WPD were welded, while non-contact inspection was performed on a section of the welds. Results from the in-process screening have shown that variations in the arc energy and the resulting WPD, have an effect on the propagation of guided Lamb waves:

Firstly, the signal amplitude RoC showed an apparent parabolic correlation to the WPD of each sample. Therefore, unintentional variations in the weld bead geometry, i.e. lack of root penetration and excessive penetration/undercut greater than 0.5 mm were detected, when comparing the measurements to a baseline sample.

Secondly, the location of the peak signal amplitude RoC and the total Lamb wave phase shift demonstrated an apparent linear correlation to the arc energy. This relationship can be used to detect an increase or decrease in heat input, when comparing the measurements to a baseline sample.

In conclusion, air-coupled ultrasonic inspection enabled, for the first time, an in-process non-contact screening method for GTAW welding.

Chapter 6

Conclusion and Future Work

6.1. Suggestions for Future Work

6.1.1. Sensor-enabled Robotic Welding and NDE System

The next iteration of the robotic welding software will be aimed at fully automating the deposition of a complete multi-pass joint. The ability to import a WPS with all welding pass locations and welding settings would reduce the need for human input and would increase the repeatability of the system. Complex weld geometries such as pipe saddle welds could be achieved through a combination of CAM robotic path generation and advanced laser profiler seam tracking. As the bandwidth and storage of the cRIO were only sufficient for inspection with conventional UT probes, the LTPA had to be directly connected to the host PC when using phased array probes. This bandwidth limitation could be addressed by substituting the cRIO with a high-performance NI PXI real-time controller.

6.1.2. On-line Ultrasonic Thickness Measurement Based Welding Parameter Control

Although all thickness measurements assumed a constant lateral thickness of the sample, the flexible mount for the ultrasonic wheel probe allows for it to be positioned in front of the welding torch in order to measure the material thickness exactly at the weld interface. Moreover, if both plates are expected to change in thickness independently, (e.g. in support varying thickness fillet welds) a second UT probe could be placed on the second plate and a measurement of the two readings could be used to calculate the required welding parameters and welding torch orientation. The real-time robot control approach makes it possible to adjust the welding torch orientation on-the-fly, in order to direct the welding arc as necessary. Therefore, the system can be deployed in various situations and with different weld geometries, e.g. circumferential, fillet and lap, among others.

The proposed feed-forward system could also be deployed in conjunction with optical and other feed-back methods through sensor fusion, which would further increase the control over the final weld seam quality and metallurgical properties. To use the developed control approach in high speed welding processes like PAW and Laser Arc Welding (LAW), the measurement latency can be reduced by lowering the number of samples for the signal acquisition averaging and the median filter. However, a trade-off between latency and accuracy is expected, and further digital signal processing might be required to address this. Lastly, the surface finish of real-world samples (e.g. corrosion, dirt and oil) would

have a detrimental effect on the ultrasonic thickness measurement, which must be further investigated.

6.1.3. Non-contact In-process Screening of Thin Welded Joints

Despite the low signal amplitudes involved, the main limitation of the outlined approach was the fixed location of the ultrasonic transducers, as only a small section of the welded joint was inspected. A more practical application of the UT method would be to scan the full length of the weld by moving the transducers at a fixed distance behind the welding torch. With the current experimental setup and welding speed of 80 mm/min, one measurement would be performed for every 0.85 mm of weld, which would provide satisfactory overlap, given that the area of sensitivity (inspection region) was around 50 mm. The obtained ultrasonic B-scan would consist of multiple measurements and would represent a complete image of the weld seam. In an industrial environment, the welding parameters and arc energy used for all components would be the same and, therefore, the temperature and cooling rate would not change from sample to sample. This, along with maintaining the same distance from the welding torch for all ultrasonic measurements, would remove the workpiece temperature as a variable. This would enable the use of traditional amplitude sizing, and would remove the need to monitor the RoC of the signal amplitude. Additionally it would be beneficial to measure the signal amplitude for each sample until it is fully cooled down in order to establish how the amplitude RoC relates to the amplitude of the cooled samples.

The exact beam spread of the guided Lamb waves at high temperatures should be studied in order to more accurately determine the inspection region covered by the transducers. Furthermore, the effects of the high temperature gradient in the inspection region should be further investigated using FEA simulations. The possibility of using a non-air gas such as Argon should be explored as an option for increasing the transmission coefficient when exciting the ultrasonic Lamb waves in the steel workpiece. A sensitivity and repeatability study should also be carried out on the screening technique using artificially induced defects, and the effects of sample distortion and surface finish on the screening method should be studied, in order to identify suitable applications for the proposed approach.

6.2. General Overview

The growing robotic automation of HVM welded components has increased the need for fast, in-line automated NDE, to compensate for the current manually deployed inspection of the as-welded parts. Current state-of-the-art robotic systems are highly dependent on the available manufacturer software, significantly limiting the possibilities in terms of sensor integration and process control. Moreover, new, sensor-enabled and intelligent systems are required to address the needs of the 4th industrial revolution, and to tackle the production inefficiency and shrinking skilled workforce challenges.

When considering automated fusion welding, the delay between defect formation and detection can be significantly reduced by integrating NDE into the welding process. This could be particularly beneficial for welded assets that require multiple days to manufacture, such as WAAM components and thicker section multi-pass welds. The implementation of

in-process NDE would fundamentally result in higher production quality, reduced scrap rates, more predictable component lead times and overall lower costs of final product.

This thesis has addressed a number of technological barriers and has contributed to the areas of sensor-enabled robotics, automated fusion welding and automated in-process NDE of welded joints.

A key technological enabler was developed, with the potential to enhance a number of different robotic manufacture and NDE applications, aside from the fusion welding and NDE of welds discussed herein. An adaptive robotic control algorithm taking advantage of the RSI protocol, allows for the real-time correction-based control of KUKA industrial manipulators through a separate, external controller. Moreover, the low-latency adaptive motion controller can influence the robotic end-effector position every 4 ms through multi-sensory input. This was leveraged to create a sensor-enabled multi-robot welding and in-process NDE system.

An ultrasonic wheel probe has been deployed, for the first time, during the welding process for on-the-fly welding process control. An ultrasonic thickness measurement of the workpiece was enabled by robust on-line signal processing, allowing for the establishment of control relationships between key welding parameters and sample thickness. It has been demonstrated that the proposed control approach provided a sufficient response to changes in workpiece thickness, producing consistent penetration and a regular weld seam, in contrast to the excessive penetration and sample burn-through generated by an open-loop welding approach.

Finally, the in-process screening of thin fusion welded joints through non-contact gas-coupled ultrasonic transducers was investigated. A guided Lamb wave was induced in the workpiece, allowing to monitor the solidification of a section of the weld seam. It was shown that variations in arc energy and the produced weld have a measurable effect on the propagation of the guided waves, allowing to detect variations in the WPD, when comparing the detected signal with a baseline.

References

[1] F. Richter, “These are the top 10 manufacturing countries in the world,” *World Economic Forum*, Feb. 25, 2020. https://www.weforum.org/agenda/2020/02/countries-manufacturing-trade-exports-economics/ (accessed Jun. 09, 2021).

[2] Hennik Research, “Annual Manufacturing Report 2019,” *The Manufacturer*, 2020. https://www.themanufacturer.com/reports-whitepapers/manufacturer-annual-manufacturing-report-2019/ (accessed Jun. 09, 2021).

[3] M. Hardie and A. Banks, “The Changing Shape of UK Manufacturing.” The Office for National Statistics, Oct. 22, 2014.

[4] S. Mackenzie, S. Newman, and S. Zella, “Productivity economic commentary, UK - Office for National Statistics,” *Office for National Statistics*, Apr. 2021. https://www.ons.gov.uk/employmentandlabourmarket/peopleinwork/labourproductivity/articles/ukproductivityintroduction/octobertodecember2020 (accessed Jun. 09, 2021).

[5] Deloitte Manufacturing Institute, “The skills gap in U.S. manufacturing 2015 and beyond.” 2015.

[6] K. Weman, *Welding Process Handbook*, Second Edition. Woodhead Publishing Limited, 2012.

[7] Airbus, “Flying by numbers: Global Market Forecast for 2015-2034.” 2015.

[8] McKinsey & Company, “The road to 2020 and beyond: What’s driving the global automotive industry.” Sep. 2013.

[9] IHS Global, “Impact of the Manufacturing Renaissance from Energy Intensive Sectors.” 2013.

[10] “What is Industry 4.0? How Does it Work? (A Beginners Guide).” https://www.twi-global.com/what-we-do/research-and-technology/technologies/industry-4-0.aspx (accessed Apr. 08, 2021).

[11] A. Chinchane and S. Onkar, “Robotic Welding Market Size, Share | Welding Robot Statistics by 2026,” *Allied Market Research*, Nov. 2019. https://www.alliedmarketresearch.com/robotic-welding-market (accessed Mar. 17, 2021).

[12] R. Halmshaw, *Non-Destructive Testing*, 2nd ed. 1991.

[13] The Welding Institute, “Which standards stipulate delay time before inspecting welds?” https://www.twi-global.com/technical-knowledge/faqs/faq-which-standards-stipulate-delay-time-before-inspecting-welds.aspx (accessed Jun. 09, 2021).

[14] “Non-destructive testing of welds — Phased array ultrasonic testing (PAUT) — Acceptance levels (BS EN ISO 19285:2017).” The British Standards Institution, Sep. 2017. [Online]. Available: https://shop.bsigroup.com/ProductDetail?pid=000000000030342680

[15] C. Mineo *et al.*, “Fast ultrasonic phased array inspection of complex geometries delivered through robotic manipulators and high speed data acquisition instrumentation,” in *2016 IEEE International Ultrasonics Symposium (IUS)*, Sep. 2016, pp. 1–4. doi: 10.1109/ULTSYM.2016.7728746.

[16] G. Dobie, R. Summan, S. G. Pierce, W. Galbraith, and G. Hayward, “A Noncontact Ultrasonic Platform for Structural Inspection,” *IEEE Sensors Journal*, vol. 11, no. 10, pp. 2458–2468, Oct. 2011, doi: 10.1109/JSEN.2011.2138131.

[17] J. A. Hashem, M. Pryor, S. Landsberger, J. Hunter, and D. R. Janecky, “Automating High-Precision X-Ray and Neutron Imaging Applications With Robotics,” *IEEE Transactions on Automation Science and Engineering*, vol. 15, no. 2, pp. 663–674, Apr. 2018, doi: 10.1109/TASE.2017.2675709.

[18] R. M. Stern, A. Berlin, A. Fletcher, K. Hemminki, J. Jarvisalo, and J. Peto, “International conference on health hazards and biological effects of welding fumes and gases,” *Int. Arch Occup Environ Heath*, vol. 57, no. 3, pp. 237–246, Mar. 1986, doi: 10.1007/BF00405791.

[19] S. W. Williams, F. Martina, A. C. Addison, J. Ding, G. Pardal, and P. Colegrove, “Wire + Arc Additive Manufacturing,” *Materials Science and Technology*, vol. 32, no. 7, pp. 641–647, May 2016, doi: 10.1179/1743284715Y.0000000073.

[20] T. DebRoy *et al.*, “Additive manufacturing of metallic components – Process, structure and properties,” *Progress in Materials Science*, vol. 92, pp. 112–224, Mar. 2018, doi: 10.1016/j.pmatsci.2017.10.001.

[21] J. F. Lancaster, “The physics of fusion welding. Part 1: The electric arc in welding,” *IEE Proceedings B - Electric Power Applications*, vol. 134, no. 5, pp. 233–254, Sep. 1987, doi: 10.1049/ip-b.1987.0040.

[22] A. Salminen, H. Piili, and T. Purtonen, “The characteristics of high power fibre laser welding,” *Proceedings of the Institution of Mechanical Engineers, Part C: Journal of Mechanical Engineering Science*, vol. 224, no. 5, pp. 1019–1029, May 2010, doi: 10.1243/09544062JMES1762.

[23] L. Jeffus, *Welding: Principles and Applications*. Cengage Learning, 2020.

[24] TWI Ltd, “What is the difference between heat input and arc energy?” twi-global.com/technical-knowledge/faqs/faq-what-is-the-difference-between-heat-input-and-arc-energy.aspx (accessed Sep. 04, 2019).

[25] The British Standards Institution, “BS EN ISO 6520-1:2007 Welding and allied processes — Classification of geometric imperfections in metallic materials.” 2007.

[26] T. Font comas, C. Diao, J. Ding, S. Williams, and Y. Zhao, “A Passive Imaging System for Geometry Measurement for the Plasma Arc Welding Process,” *IEEE Transactions on Industrial Electronics*, vol. 64, no. 9, pp. 7201–7209, Sep. 2017, doi: 10.1109/TIE.2017.2686349.

[27] P. Ghanty *et al.*, “Artificial neural network approach for estimating weld bead width and depth of penetration from infrared thermal image of weld pool,” *Science and Technology of Welding and Joining*, vol. 13, no. 4, pp. 395–401, May 2008, doi: 10.1179/174329308X300118.

[28] J. Mirapeix Serrano, R. Ruiz-Lombera, J. J. Valdiande, A. Cobo, and J. M. Lopez-Higuera, “Colorimetric Analysis for On-Line Arc-Welding Diagnostics by Means of Plasma Optical Spectroscopy,” *IEEE Sensors Journal*, vol. 16, no. 10, pp. 3465–3471, May 2016, doi: 10.1109/JSEN.2015.2413057.

[29] X. Li, X. Li, S. S. Ge, M. O. Khyam, and C. Luo, “Automatic Welding Seam Tracking and Identification,” *IEEE Transactions on Industrial Electronics*, vol. 64, no. 9, pp. 7261–7271, Sep. 2017, doi: 10.1109/TIE.2017.2694399.

[30] Yuan Li, You Fu Li, Qing Lin Wang, De Xu, and Min Tan, “Measurement and Defect Detection of the Weld Bead Based on Online Vision Inspection,” *IEEE Transactions on Instrumentation and Measurement*, vol. 59, no. 7, pp. 1841–1849, Jul. 2010, doi: 10.1109/TIM.2009.2028222.

[31] Y. M. Zhang, R. Kovacevic, and L. Li, “Adaptive control of full penetration gas tungsten arc welding,” *IEEE Transactions on Control Systems Technology*, vol. 4, no. 4, pp. 394–403, Jul. 1996, doi: 10.1109/87.508887.

[32] Z. Wang, “An Imaging and Measurement System for Robust Reconstruction of Weld Pool During Arc Welding,” *IEEE Transactions on Industrial Electronics*, vol. 62, no. 8, pp. 5109–5118, Aug. 2015, doi: 10.1109/TIE.2015.2405494.

[33] Y. Liu, W. J. Zhang, and Y. Zhang, “Estimation of Weld Joint Penetration under Varying GTA Pools,” *Welding Journal*, 2013.

[34] Y. Liu and Y. Zhang, “Control of 3D weld pool surface,” *Control Engineering Practice*, vol. 21, no. 11, pp. 1469–1480, Nov. 2013, doi: 10.1016/j.conengprac.2013.06.019.

[35] G. C. Anzalone, Chenlong Zhang, B. Wijnen, P. G. Sanders, and J. M. Pearce, “A Low-Cost Open-Source Metal 3-D Printer,” *IEEE Access*, vol. 1, pp. 803–810, 2013, doi: 10.1109/ACCESS.2013.2293018.

[36] F. Martina, J. Ding, S. Williams, A. Caballero, G. Pardal, and L. Quintino, “Tandem metal inert gas process for high productivity wire arc additive manufacturing in stainless steel,” *Additive Manufacturing*, vol. 25, pp. 545–550, Jan. 2019, doi: 10.1016/j.addma.2018.11.022.

[37] F. Michel, H. Lockett, J. Ding, F. Martina, G. Marinelli, and S. Williams, “A modular path planning solution for Wire + Arc Additive Manufacturing,” *Robotics and Computer-Integrated Manufacturing*, vol. 60, pp. 1–11, Dec. 2019, doi: 10.1016/j.rcim.2019.05.009.

[38] J. Hönnige *et al.*, "Study of residual stress and microstructural evolution in as-deposited and inter-pass rolled wire plus arc additively manufactured Inconel 718 alloy after ageing treatment," *Materials Science and Engineering: A*, vol. 801, p. 140368, Jan. 2021, doi: 10.1016/j.msea.2020.140368.

[39] D. Mishra and M. Dakkili, "Gas tungsten and shielded metal arc welding of stainless steel 310 and 304 grades over single and double 'V' butt joints," *Materials Today: Proceedings*, Jan. 2020, doi: 10.1016/j.matpr.2019.12.189.

[40] X. Gao, X. Zhou, C. Wang, N. Ma, Y. Zhang, and D. You, "Skin depth and detection ability of magneto-optical imaging for weld defects in alternating magnetic field," *Journal of Manufacturing Systems*, vol. 55, pp. 44–55, Apr. 2020, doi: 10.1016/j.jmsy.2020.02.006.

[41] P. Gao, C. Wang, Y. Li, and Z. Cong, "Electromagnetic and eddy current NDT in weld inspection: A review," *Insight - Non-Destructive Testing and Condition Monitoring*, vol. 57, Jun. 2015, doi: 10.1784/insi.2015.57.6.337.

[42] N. Nacereddine, A. B. Goumeidane, and D. Ziou, "Unsupervised weld defect classification in radiographic images using multivariate generalized Gaussian mixture model with exact computation of mean and shape parameters," *Computers in Industry*, vol. 108, pp. 132–149, Jun. 2019, doi: 10.1016/j.compind.2019.02.010.

[43] B. W. Drinkwater and P. D. Wilcox, “Ultrasonic arrays for non-destructive evaluation: A review,” *NDT & E International*, vol. 39, no. 7, pp. 525–541, Oct. 2006, doi: 10.1016/j.ndteint.2006.03.006.

[44] R. J. Ditchburn, S. K. Burke, and C. M. Scala, “NDT of welds: state of the art,” *NDT & E International*, vol. 29, no. 2, pp. 111–117, Apr. 1996, doi: 10.1016/0963-8695(96)00010-2.

[45] W. J. Fleming, “New Automotive Sensors—A Review,” *IEEE Sensors Journal*, vol. 8, no. 11, pp. 1900–1921, Nov. 2008, doi: 10.1109/JSEN.2008.2006452.

[46] A. Carullo and M. Parvis, “An ultrasonic sensor for distance measurement in automotive applications,” *IEEE Sensors Journal*, vol. 1, no. 2, pp. 143-, Aug. 2001, doi: 10.1109/JSEN.2001.936931.

[47] D. Ensminger, *Ultrasonics: fundamentals, technologies, and applications*. CRC Press, 2011. Accessed: May 31, 2021. [Online]. Available: https://www.vlebooks.com/Vleweb/Product/Index/78042

[48] S. P. Kelly, R. Farlow, and G. Hayward, “Applications of through-air ultrasound for rapid NDE scanning in the aerospace industry,” *IEEE Transactions on Ultrasonics, Ferroelectrics, and Frequency Control*, vol. 43, no. 4, pp. 581–591, Jul. 1996, doi: 10.1109/58.503780.

[49] C. Holmes, B. W. Drinkwater, and P. D. Wilcox, "Post-processing of the full matrix of ultrasonic transmit–receive array data for non-destructive evaluation," *NDT & E International*, vol. 38, no. 8, pp. 701–711, Dec. 2005, doi: 10.1016/j.ndteint.2005.04.002.

[50] P. D. Wilcox, C. Holmes, B. W. Drinkwater, and D. Of, "Enhanced Defect Detection and Characterisation by Signal Processing of Ultrasonic Array Data," presented at the 9th European Conference on NDT - September 2006 - (ECNDT 2006), Berlin (Germany), 2006. doi: 10.1.1.159.6666.

[51] Y. Javadi *et al.*, "Ultrasonic phased array inspection of a Wire + Arc Additive Manufactured (WAAM) sample with intentionally embedded defects," *Additive Manufacturing*, vol. 29, p. 100806, Oct. 2019, doi: 10.1016/j.addma.2019.100806.

[52] Y. Javadi *et al.*, "Ultrasonic phased array inspection of wire + arc additive manufacture samples using conventional and total focusing method imaging approaches," *Insight: Non-Destructive Testing and Condition Monitoring*, vol. 61, no. 3, Art. no. 3, Mar. 2019, doi: 10.1784/insi.2019.61.3.144.

[53] A. Chabot, N. Laroche, E. Carcreff, M. Rauch, and J.-Y. Hascoët, "Towards defect monitoring for metallic additive manufacturing components using phased array ultrasonic testing," *J Intell Manuf*, vol. 31, no. 5, pp. 1191–1201, Jun. 2020, doi: 10.1007/s10845-019-01505-9.

[54] OLYMPUS, “WeldROVER Scanner.” https://www.olympus-ims.com/en/scanners/weldrover/ (accessed May 13, 2021).

[55] JIREH Industries, “NAVIC - Weld Scanner,” *JIREH Industries*. //www.jireh.com/products/navic-weld-scanner/ (accessed May 17, 2021).

[56] Eddify, “Scorpion 2 Ultrasonic Tank Shell Inspection | UT Thickness Readings.” https://www.eddyfi.com/en/product/scorpion-2 (accessed May 17, 2021).

[57] A. McGregor, G. Dobie, N. R. Pearson, C. N. MacLeod, and A. Gachagan, “Determining Position and Orientation of a 3-Wheel Robot on a Pipe Using an Accelerometer,” *IEEE Sensors Journal*, vol. 20, no. 9, pp. 5061–5071, May 2020, doi: 10.1109/JSEN.2020.2964619.

[58] D. Zhang, R. Watson, G. Dobie, C. MacLeod, A. Khan, and G. Pierce, “Quantifying impacts on remote photogrammetric inspection using unmanned aerial vehicles,” *Engineering Structures*, vol. 209, p. 109940, Apr. 2020, doi: 10.1016/j.engstruct.2019.109940.

[59] M. Car, L. Markovic, A. Ivanovic, M. Orsag, and S. Bogdan, “Autonomous Wind-Turbine Blade Inspection Using LiDAR-Equipped Unmanned Aerial Vehicle,” *IEEE Access*, vol. 8, pp. 131380–131387, 2020, doi: 10.1109/ACCESS.2020.3009738.

[60] D. Zhang, R. Watson, C. MacLeod, G. Dobie, W. Galbraith, and G. Pierce, "Implementation and evaluation of an autonomous airborne ultrasound inspection system," *Nondestructive Testing and Evaluation*, vol. 0, no. 0, pp. 1–21, Feb. 2021, doi: 10.1080/10589759.2021.1889546.

[61] R. J. Watson *et al.*, "Deployment of Contact-Based Ultrasonic Thickness Measurements Using Over-Actuated UAVs," in *European Workshop on Structural Health Monitoring*, Cham, 2021, pp. 683–694. doi: 10.1007/978-3-030-64594-6_66.

[62] KUKA AG, "Industrial robotics_low payloads," 2018. https://www.kuka.com/-/media/kuka-downloads/imported/9cb8e311bfd744b4b0eab25ca883f6d3/kuka_robotics_low_payloads.pdf?rev=cbf117123ca142dda4c7abe9ba0a3e64&hash=2EC50752C478393CC7DD0E76F272BC59 (accessed May 19, 2021).

[63] Y. Javadi *et al.*, "High-temperature in-process inspection followed by 96-h robotic inspection of intentionally manufactured hydrogen crack in multi-pass robotic welding," *International Journal of Pressure Vessels and Piping*, vol. 189, p. 104288, Feb. 2021, doi: 10.1016/j.ijpvp.2020.104288.

[64] OLYMPUS, "Ultrasonic phased array wedge for inspecting high-temperature parts up to 150°C." https://www.olympus-ims.com/en/applications/ultrasonic-phased-array-wedge-for-inspecting-high-temperature-parts-up-to-150c/ (accessed Sep. 02, 2019).

[65] J. Ji, W. Chen, and X. Yang, “Arc welding inverter with embedded Digital Active EMI controller,” in *2016 IEEE Applied Power Electronics Conference and Exposition (APEC)*, Mar. 2016, pp. 493–498. doi: 10.1109/APEC.2016.7467917.

[66] “KUKA.RobotSensorInterface 4.0.” KUKA Deutschland GmbH, Aug. 2018.

[67] C. Mineo *et al.*, “Enabling robotic adaptive behaviour capabilities for new Industry 4.0 automated quality inspection paradigms,” *insight*, vol. 62, no. 6, pp. 338–344, Jun. 2020, doi: 10.1784/insi.2020.62.6.338.

[68] National Instruments, “cRIO-9038.” http://www.ni.com/en-gb/support/model.crio-9038.html (accessed Sep. 05, 2019).

[69] Jäckle Schweiß- und Schneidtechnik GmbH, “Jackle ProTIG 350AC / DC Operating Manual.” https://www.jess-welding.com/en/portfolio/protig-350-500/

[70] Micro-Epsilon, “Compact laser scanner for high precision.” https://www.micro-epsilon.co.uk/2D_3D/laser-scanner/scanCONTROL-2900/ (accessed Mar. 05, 2020).

[71] Xiris Automation Inc., “XVC-1000 / 1100 Weld Camera.” https://www.xiris.com/xiris-xvc-1000/ (accessed May 19, 2021).

[72] PeakNDT, “PEAK LTPA Specification,” *PeakNDT*. https://www.peakndt.com/products/ltpa/ (accessed Sep. 05, 2019).

[73] “What is LabVIEW?” https://www.ni.com/en-gb/shop/labview.html (accessed Jun. 21, 2021).

[74] "JKISoftware/JKI-State-Machine," Mar. 26, 2021. https://github.com/JKISoftware/JKI-State-Machine (accessed Apr. 08, 2021).

[75] M. Morozov, S. G. Pierce, C. N. MacLeod, C. Mineo, and R. Summan, "Off-line scan path planning for robotic NDT," *Measurement*, vol. 122, pp. 284–290, Jul. 2018, doi: 10.1016/j.measurement.2018.02.020.

[76] C. N. Macleod, G. Dobie, S. G. Pierce, R. Summan, and M. Morozov, "Machining-Based Coverage Path Planning for Automated Structural Inspection," *IEEE Transactions on Automation Science and Engineering*, vol. 15, no. 1, pp. 202–213, Jan. 2018, doi: 10.1109/TASE.2016.2601880.

[77] C. Mineo, S. G. Pierce, P. I. Nicholson, and I. Cooper, "Robotic path planning for non-destructive testing – A custom MATLAB toolbox approach," *Robotics and Computer-Integrated Manufacturing*, vol. 37, pp. 1–12, Feb. 2016, doi: 10.1016/j.rcim.2015.05.003.

[78] M. Morozov *et al.*, "Assessing the accuracy of industrial robots through metrology for the enhancement of automated non-destructive testing," in *2016 IEEE International Conference on Multisensor Fusion and Integration for Intelligent Systems (MFI)*, Sep. 2016, pp. 335–340. doi: 10.1109/MFI.2016.7849510.

[79] A. E. Öberg and E. Åstrand, "Variation in welding procedure specification approach and its effect on productivity," *Procedia Manufacturing*, vol. 25, pp. 412–417, Jan. 2018, doi: 10.1016/j.promfg.2018.06.111.

[80] K. Weman and G. Lindén, *Mig Welding Guide*. Woodhead Publishing, 2006.

[81] R. K. W. Vithanage *et al.*, "A phased array ultrasound roller probe for automated in-process/interpass inspection of multipass welds," *IEEE Transactions on Industrial Electronics*, pp. 1–1, 2020, doi: 10.1109/TIE.2020.3042112.

[82] L. C. Lynnworth, *Ultrasonic Measurements for Process Control: Theory, Techniques, Applications*. Academic Press, 2013.

[83] T. Pfeifer and M. Benz, "Ultrasonic on-machine measurement for internal topographies," *International Journal of Production Research*, vol. 40, no. 15, pp. 3821–3834, Jan. 2002, doi: 10.1080/00207540210133525.

[84] B. P. C. Rao, B. Raj, T. Jayakumar, and P. Kalyanasundaram, "An artificial neural network for eddy current testing of austenitic stainless steel welds," *NDT & E International*, vol. 35, no. 6, pp. 393–398, Sep. 2002, doi: 10.1016/S0963-8695(02)00007-5.

[85] T. Kiwa, H. Tahara, E. Miyake, H. Yamada, and K. Tsukada, "Non-Contact Thickness Gauge for Conductive Materials Using HTS SQUID System," *IEEE Transactions on Applied Superconductivity*, vol. 19, no. 3, pp. 801–803, Jun. 2009, doi: 10.1109/TASC.2009.2019196.

[86] Y. Yu, Y. Zou, M. A. Hosani, and G. Tian, "Conductivity Invariance Phenomenon of Eddy Current NDT: Investigation, Verification, and Application," *IEEE Transactions on Magnetics*, vol. 53, no. 1, pp. 1–7, Jan. 2017, doi: 10.1109/TMAG.2016.2616328.

[87] OLYMPUS, “45MG Ultrasonic Thickness Gage.” https://www.olympus-ims.com/en/45mg/#!cms[focus]=cmsContent11047 (accessed Feb. 11, 2020).

[88] B. Drinkwater and P. Cawley, “An Ultrasonic Wheel Probe Alternative to Liquid Coupling,” in *Review of Progress in Quantitative Nondestructive Evaluation: Volume 14*, D. O. Thompson and D. E. Chimenti, Eds. Boston, MA: Springer US, 1995, pp. 983–989. doi: 10.1007/978-1-4615-1987-4_124.

[89] C. Mineo *et al.*, “Fast ultrasonic phased array inspection of complex geometries delivered through robotic manipulators and high speed data acquisition instrumentation,” in *2016 IEEE International Ultrasonics Symposium (IUS)*, Sep. 2016, pp. 1–4. doi: 10.1109/ULTSYM.2016.7728746.

[90] MillerWelds, “TIG Weld Setting Calculator.” https://www.millerwelds.com/resources/weld-setting-calculators/tig-welding-calculator (accessed Mar. 05, 2020).

[91] “Autodesk Inventor | 2022, 2021 Features | Modelling.” https://www.autodesk.com/products/inventor/features#modeling (accessed Aug. 03, 2021).

[92] Eddyfi, “R-scan Manual Ultrasonic System.” https://eddyfi.com/en/product/rscan-manual-ultrasonic-system (accessed Mar. 05, 2020).

[93] “MATLAB - MathWorks.” https://uk.mathworks.com/products/matlab.html (accessed Jun. 21, 2021).

[94] H. Gao, B. Lopez, X. Minguez, and J. Chen, “Ultrasonic inspection of partially completed welds using EMAT-generated surface wave technology,” in *NDT New Technology & Application Forum (FENDT), 2015 IEEE Far East*, 2015, pp. 263–266.

[95] H.-J. Salzburger, G. Dobmann, and H. Mohrbacher, “Quality control of laser welds of tailored blanks using guided waves and EMATs,” *IEE Proceedings - Science, Measurement and Technology*, vol. 148, no. 4, pp. 143–148, Jul. 2001, doi: 10.1049/ip-smt:20010534.

[96] C. Chen, N. Lv, and S. Chen, “Welding penetration monitoring for pulsed GTAW using visual sensor based on AAM and random forests,” *Journal of Manufacturing Processes*, Apr. 2020, doi: 10.1016/j.jmapro.2020.04.005.

[97] R. Yu, J. Han, Z. Zhao, and L. Bai, “Real-Time Prediction of Welding Penetration Mode and Depth Based on Visual Characteristics of Weld Pool in GMAW Process,” *IEEE Access*, vol. 8, pp. 81564–81573, 2020, doi: 10.1109/ACCESS.2020.2990902.

[98] J. Lu, Y. Shi, L. Bai, Z. Zhao, and J. Han, “Collaborative and Quantitative Prediction for Reinforcement and Penetration Depth of Weld Bead Based on Molten Pool Image and Deep Residual Network,” *IEEE Access*, vol. 8, pp. 126138–126148, 2020, doi: 10.1109/ACCESS.2020.3007815.

[99] Q. Wang, Y. Gao, L. Huang, Y. Gong, and J. Xiao, “Weld bead penetration state recognition in GMAW process based on a central auditory perception model,” *Measurement*, vol. 147, p. 106901, Dec. 2019, doi: 10.1016/j.measurement.2019.106901.

[100] L. Yang and I. C. Ume, “Measurement of weld penetration depths in thin structures using transmission coefficients of laser-generated Lamb waves and neural network,” *Ultrasonics*, vol. 78, pp. 96–109, Jul. 2017, doi: 10.1016/j.ultras.2017.02.019.

[101] A. Kita and I. C. Ume, “Measuring On-Line and Off-Line Noncontact Ultrasound Time of Flight Weld Penetration Depth,” *WELDING JOURNAL*, p. 9, 2007.

[102] S. E. Burrows, B. Dutton, and S. Dixon, “Laser generation of lamb waves for defect detection: Experimental methods and finite element modeling,” *IEEE Transactions on Ultrasonics, Ferroelectrics, and Frequency Control*, vol. 59, no. 1, pp. 82–89, Jan. 2012, doi: 10.1109/TUFFC.2012.2158.

[103] D. Cerniglia and N. Montinaro, “Defect Detection in Additively Manufactured Components: Laser Ultrasound and Laser Thermography Comparison,” *Procedia Structural Integrity*, vol. 8, pp. 154–162, Jan. 2018, doi: 10.1016/j.prostr.2017.12.016.

[104] Z. Abbasi *et al.*, “The Detection of Burn-Through Weld Defects Using Noncontact Ultrasonics,” *Materials*, vol. 11, no. 1, Art. no. 1, Jan. 2018, doi: 10.3390/ma11010128.

[105] L. Zhang, A. C. Basantes-Defaz, D. Ozevin, and E. Indacochea, “Real-time monitoring of welding process using air-coupled ultrasonics and acoustic emission,” *The International Journal of Advanced Manufacturing Technology*, vol. 101, no. 5–8, pp. 1623–1634, Apr. 2019, doi: 10.1007/s00170-018-3042-2.

[106] I. A. Viktorov., *Rayleigh and Lamb waves: Physical theory and applications.* Plenum Press, 1967.

[107] L. Zeng and J. Lin, “Structural damage imaging approaches based on lamb waves: A review,” in *2011 International Conference on Quality, Reliability, Risk, Maintenance, and Safety Engineering*, Jun. 2011, pp. 986–993. doi: 10.1109/ICQR2MSE.2011.5976769.

[108] F. Gao, L. Zeng, J. Lin, and Y. Shao, “Damage assessment in composite laminates via broadband Lamb wave,” *Ultrasonics*, vol. 86, pp. 49–58, May 2018, doi: 10.1016/j.ultras.2018.01.005.

[109] P. Huthwaite and M. Seher, “Robust helical path separation for thickness mapping of pipes by guided wave tomography,” *IEEE Transactions on Ultrasonics, Ferroelectrics, and Frequency Control*, vol. 62, no. 5, pp. 927–938, May 2015, doi: 10.1109/TUFFC.2014.006884.

[110] F. Simonetti and M. Y. Alqaradawi, “Guided ultrasonic wave tomography of a pipe bend exposed to environmental conditions: A long-term monitoring experiment,” *NDT & E International*, vol. 105, pp. 1–10, Jul. 2019, doi: 10.1016/j.ndteint.2019.04.010.

[111] J. Zhang, H. Ma, W. Yan, and Z. Li, “Defect detection and location in switch rails by acoustic emission and Lamb wave analysis: A feasibility study,” *Applied Acoustics*, vol. 105, pp. 67–74, Apr. 2016, doi: 10.1016/j.apacoust.2015.11.018.

[112] G. Dobie, W. Galbraith, M. Friedrich, S. G. Pierce, and G. Hayward, “P0-8 Robotic Based Reconfigurable Lamb Wave Scanner for Non-Destructive Evaluation,” in *2007 IEEE Ultrasonics Symposium Proceedings*, Oct. 2007, pp. 1213–1216. doi: 10.1109/ULTSYM.2007.305.

[113] B. Pavlakovic, M. Lowe, O. Alleyne, and P. Cawley, "Disperse: a general purpose program for creating dispersion curves. Review of progress in quantitative nondestructive evaluation," *Review of Progress in Quantitative Nondestructive Evaluation*, vol. 16A, 1997.

[114] C. B. Scruby and B. C. Moss, "Non-contact ultrasonic measurements on steel at elevated temperatures," *NDT & E International*, vol. 26, no. 4, pp. 177–188, Aug. 1993, doi: 10.1016/0963-8695(93)90472-7.

[115] A. Gachagan, G. Hayward, S. P. Kelly, and W. Galbraith, "Characterization of air-coupled transducers," *IEEE Transactions on Ultrasonics, Ferroelectrics, and Frequency Control*, vol. 43, no. 4, pp. 678–689, Jul. 1996, doi: 10.1109/58.503730.

[116] S. P. Kelly, G. Hayward, and T. E. Gomez, "An air-coupled ultrasonic matching layer employing half wavelength cavity resonance," in *2001 IEEE Ultrasonics Symposium. Proceedings. An International Symposium (Cat. No.01CH37263)*, Oct. 2001, vol. 2, pp. 965–968 vol.2. doi: 10.1109/ULTSYM.2001.991880.

[117] RS Components, "RS PRO Transparent Silicone Sealant Liquid 90 ml Tube 692-542." https://uk.rs-online.com/web/p/silicone-sealants/0692542/ (accessed Jun. 16, 2020).

[118] G. Hayward, A. Gachagan, R. Hamilton, D. A. Hutchins, and W. M. D. Wright, "Ceramic-epoxy composite transducers for noncontacting ultrasonic applications," in *New Developments in Ultrasonic Transducers and Transducer Systems*, Nov. 1992, vol. 1733, pp. 49–56. doi: 10.1117/12.130588.

[119] A. Gachagan, “An evaluation of 13 connectivity composite transducers for aircoupled ultrasonic applications,” PhD Thesis, University of Strathclyde, Glasgow, 1996.

[120] S. P. Kelly, “An air-coupled ultrasonic array scanning system for rapid through transmission NDT,” PhD Thesis, University of Strathclyde, Glasgow, 2000.

[121] G. Dobie, S. Gareth Pierce, and G. Hayward, “The feasibility of synthetic aperture guided wave imaging to a mobile sensor platform,” *NDT & E International*, vol. 58, pp. 10–17, Sep. 2013, doi: 10.1016/j.ndteint.2013.04.002.

[122] G. Dobie, “Ultrasonic sensor platforms for non-destructive evaluation,” PhD Thesis, University of Strathclyde, Glasgow, 2010.

[123] Adobe, “Measurement features in Photoshop,” Aug. 21, 2019. https://helpx.adobe.com/photoshop/using/measurement.html (accessed Jun. 14, 2021).

[124] C. Steimbreger and M. D. Chapetti, “Fatigue strength assessment of butt-welded joints with undercuts,” *International Journal of Fatigue*, vol. 105, pp. 296–304, Dec. 2017, doi: 10.1016/j.ijfatigue.2017.09.011.